Fakultät Maschinenbau
fortschritt studieren

RUHR
UNIVERSITÄT
BOCHUM

RUB

Large-eddy simulation of a modified T106 low-pressure turbine stator under periodic wake impact

Dissertation

zur
Erlangung des Grades
Doktor-Ingenieur

der
Fakultät für Maschinenbau
der Ruhr-Universität Bochum

von
Benjamin Winhart
aus Berlin

Bochum 2021

Dissertation eingereicht am: 26.04.2021
Tag der mündlichen Prüfung: 16.07.2021

Erster Referent: Prof. Dr. Francesca di Mare
Lehrstuhl für Thermische Turbomaschinen und Flugtriebwerke
Ruhr-Universität Bochum

Zweiter Referent: Prof. Dr.-Ing. Jörg Seume
Institut für Turbomaschinen und Fluiddynamik
Leibniz Universität Hannover

Abstract

Even today, despite the constantly advancing developments in the field of computer hardware, simulation methods based on the Reynolds-averaged Navier-Stokes (RANS) equations are still the driving force when it comes to the fluid mechanical simulation of turbomachinery flows. This is primarily due to the orders of magnitude higher computational effort required in the case of scale-resolving simulation methods such as large-eddy simulation (LES), but another aspect is the considerably higher degree of complexity required for the appropriate setup of such simulations and the efficient post-processing of the massive amounts of data.

However, a major drawback of the RANS based methods is that all effects of turbulence and boundary layer transition are represented by models which are mostly based on empirically derived correlations, introducing inaccuracies in their prediction. Especially in the case of complex flow phenomena such as the transition processes in low-pressure turbine (LPT) blades under the influence of incoming wakes, which are considered in this work, these inaccuracies can lead to misleading flow patterns, which in turn impede a targeted design of the respective blade profiles for maximum aerodynamic performance.

In the present work, an efficient work flow is described, which allows an exact determination of the boundary layer states of an LPT stator under periodic wake impact, using highly resolved LES at different operating conditions. Special attention is paid to a precise definition of the problem, the exact derivation of the resulting boundary conditions & settings, and the efficient post-processing of the resulting data, which made it possible not only to substantiate fundamental experimental findings, but also to gain insight into important flow characteristics and additional flow-physical relationships that could not be determined on the basis of the existing experimental database.

Contents

Nomenclature **VII**

1 Introduction **1**
1.1 Motivation . . . 1
1.2 State of research . . . 2
1.2.1 Historical background . . . 2
1.2.2 Turbomachinery specific research . . . 4
1.3 Objective of this work . . . 6

2 Theoretical background **8**
2.1 Aeroengines . . . 8
2.1.1 Operating principle . . . 8
2.1.2 Turbines . . . 9
2.1.3 Development trends of low-pressure turbine design . . . 11
2.1.4 The role of profile losses in low-pressure tubines . . . 14
2.2 Boundary layer flows & transition . . . 17
2.2.1 Boundary layer parameters . . . 17
2.2.2 Transition mechanisms . . . 20
2.3 Mathematical model . . . 31
2.3.1 Continuum hypothesis . . . 31
2.3.2 Navier-Stokes equations . . . 32
2.3.3 Turbulence . . . 33
2.4 Numerical fundamentals . . . 41
2.4.1 Numerical method . . . 41
2.4.2 Finite approximations . . . 42
2.4.3 Subgrid-scale modeling . . . 46
2.4.4 Pressure-velocity coupling . . . 47
2.4.5 Solution method . . . 49

3 Flow simulation **50**
3.1 Test-case . . . 50
3.1.1 Setup . . . 50
3.1.2 Flow conditions & similarity . . . 51
3.2 Numerical Setup . . . 55
3.2.1 Spatial discretization . . . 55
3.2.2 Boundary conditions . . . 61
3.2.3 Source term . . . 66
3.2.4 Transient setup . . . 68
3.2.5 Data output . . . 70

3.2.6 Computational cost . . . 71
3.3 Post processing procedures . . . 73
3.3.1 Statistical moments . . . 73
3.3.2 Q-criterion . . . 75
3.3.3 Turbulence states . . . 75
3.3.4 Spectral analysis . . . 77
3.3.5 Modal analysis . . . 79

4 Results **83**
4.1 Operating points under investigation . . . 83
4.2 LES quality assessment . . . 84
4.3 Time mean evaluation . . . 85
4.3.1 2-dimensional flow field . . . 85
4.3.2 Boundary layer analysis . . . 87
4.3.3 Wall shear stress distribution . . . 95
4.3.4 Analysis of turbulence states . . . 98
4.3.5 Summary . . . 101
4.4 Time domain evaluation . . . 102
4.4.1 Wake kinematics . . . 102
4.4.2 Time space analysis . . . 106
4.4.3 Flow visualization . . . 114
4.4.4 Summary . . . 121
4.5 Frequency domain evaluation . . . 121
4.5.1 General approach . . . 121
4.5.2 Unperturbed inflow cases . . . 122
4.5.3 Perturbed inflow cases . . . 128
4.5.4 Summary . . . 133
4.6 Modal analysis . . . 134
4.6.1 Reference case analysis . . . 134
4.6.2 Influence of free-stream turbulence . . . 140
4.6.3 Summary . . . 143

5 Summary & outlook **145**

6 Bibliography **149**

Nomenclature

Latin symbols ...

a	Wavelet scale	[s]
a_{ij}	Anisotropic part of the RST	$[m^2/s^2]$
a_k	Time coefficients	[1]
b	Time shift factor	[s]
b_{ij}	Anisotropy tensor	$[m^2/s^2]$
c	Absolute velocity	[m/s]
c_f	Friction coefficient	[1]
C	Chord length	[m]
C_w	Wale constant	[1]
$\boldsymbol{C}$	Covariance matrix	[-]
D	Diameter	[m]
$E(\kappa)$	Energy spectral density	$[m^3/s^2]$
f	Frequency	[Hz]
F_N	Net-thrust	[N]
$\mathcal{F}$	Fourier transform	[-]
$\mathcal{F}^{-1}$	Inverse Fourier transform	[-]
g	Pitch	[m]
h	Enthalpy	[J]
H	Blade/channel height	[m]
H_{12}	Shape factor	[1]
k	Turbulent kinetic energy	$[m^2/s^2]$
K	Acceleration parameter	[1]
l_0	Characteristic length scale	[m]
L	Length	[m]
L, l	Length scale	[m]
L_{11}	Longitudinal length scale	[m]
$\mathcal{L}$	Flow scale	[m]
M	Momentum	[Nm]
Ma	Mach number	[1]
$\dot{m}$	Mass flow	$[kg/m^3]$
n	Rotational speed	[rpm]
N	Integer number	[1]

p	Pressure	[Pa]
Q	Q-criterion	$[s^{-2}]$
$\boldsymbol{q'}$	Fluctuating vector field	[-]
r	Radius	[m]
R	Ideal gas constant	$[\mathrm{J}/(\mathrm{kg\,K})]$
Re	Reynolds number	[1]
Re_L	Turbulent Reynolds number	[1]
Re_0	Characteristic Reynolds number	[1]
Re_λ	Taylor scale Reynolds number	[1]
s	Entropy	[J/K]
S	Streamwise distance	[m]
S	Source term	[-]
Sr	Strouhal number	[1]
S_{ij}	Strain-rate tensor	$[s^{-1}]$
S^*	Arc length of the SS/PS	[m]
$\mathcal{S}$	Surface of the control volume	$[\mathrm{m}^2]$
t	Time	[s]
T	Temperature	[K]
T	Time period	[s]
Tu	Turbulence intensity	[1]
u	Velocity scale	[m/s]
u, v, w	Cartesian Velocity components	[m/s]
u_0	Characteristic velocity	[m/s]
u_τ	Friction velocity	[m/s]
$\boldsymbol{u}$	Velocity (vectorial notation)	[m/s]
$\boldsymbol{u}^*$	Tentative velocity (vectorial notation)	[m/s]
U	Absolute velocity	[m/s]
$\mathcal{U}$	Characteristic velocity scale	[m]
$\mathcal{V}$	Control volume	$[\mathrm{m}^3]$
w_{hann}	Hann window function	[1]
x	Axial coordinate	[m]
x, y, z	Cartesian coordinates	[m]
x^+, y^+, z^+	Non-dimensional wall distances	[1]
$\boldsymbol{x}$	Space vector	[m]

Greek symbols

α	Flow angle	[deg]

δ	Boundary layer thickness	[m]
δ^*	Displacement thickness	[m]
Δ	Variable difference prefix	[-]
Δ	Cutoff length scale	[m]
ε	Turbulent dissipation rate	[J/(kg s)]
η	Kolmogorov length scale	[m]
θ	Circumferential coordinate	[rad]
θ	Momentum thickness	[m]
κ	Wave number	$[m^{-1}]$
λ	Average free path	[m]
λ	Stagger angle	[deg]
λ_k	Eigenvalues of the covariance matrix	[-]
μ	Dynamic viscosity	[Pa s]
ν	Kinematic viscosity	$[m^2/s]$
ρ	Density	$[kg/m^3]$
σ	Standard deviation	[-]
τ	Time scale	[s]
τ	Bar passing period	[s]
τ_{ij}	Shear stress tensor	$[kg/(m\,s^2)]$
τ_w	Wall shear stress	[Pa]
ϕ	Generic variable	[-]
ϕ	Flow coefficient	[1]
$\boldsymbol{\phi}_k$	Spatial functions	[-]
ψ_{ab}	Adjustable window function	[1]
ψ^*	Complex conjugate of the wavelet function	[1]
ω	Angular frequency	$[s^{-1}]$
Ω	Angular frequency	$[s^{-1}]$
Ω_{ij}	Vorticity tensor	$[s^{-1}]$

Subscripts

$1, 2, 3, \ldots$	Axial position indicators
η	Kolmogorov scales
∞	Free stream quantity
θ	Cicumferential component
C	Casing
H	Hub
i, j, k	Indices

m	Mid-span
t	Total quantity, condition at the stagnation point
u, v, w	Cartesian Velocity components
x	axial component
x, y, z	Cartesian Spatial components
ax	Axial component
bar	Rotating bars
DI	Demarcation between dissipation range and inertial subrange
e	Edge of shear layer
EI	Demarcation between energy containing range and inertial subrange
exit	At the exit of the blade passage
lam	Laminar
MA	Maximum amplification
max	maximum value
md	Maximum displacement
norm	Normal component
r	Reattachment point
s	Separation point
sgs	subgrid-scale
tan	Tangential component
th	Theoretical
turb	Turbulent
WG	Wake generator

Operators

$(.)'$	Fluctuation part (Reynolds decomposition)
$\bar{(.)}$	Time average or spatial average
$\tilde{(.)}$	Statistial part (triple decomposition)
$\dot{(.)}$	Subgrid scale
$\hat{(.)}$	Filtering
$\langle(.)\rangle$	Phase-average
$\{(.)\}$	Ensemble average

Abbreviations

(U)RANS	(Unsteady) Reynolds-averaged Navier-Stokes

1C, 2C, 3C	1-, 2-, 3-component
APG	Adverse pressure gradient
BC	Boundary condition
BC	Power spectral density
BCDS	Bounded central difference scheme
BPF	Bar passing frequency
BPR	Bypass ratio
CBC	Convection boundedness criterion
CDS	Central difference scheme
CFD	Computational fluid dynamics
CWT	Continous wavelet transform
DFG	Deutsche Forschungsgemeinschaft
DFT	Discrete Fourier transform
DNS	Direct numerical simulation
DOF	Degrees of freedom
DTFT	Discrete-time Fourier transform
DWT	Discrete wavelet transform
FDM	Finite difference method
FEM	Finite element method
FPG	Favorable pressure gradient
FSM	Fractional step method
FST	Free stream turbulence
FSTI	Free stream turbulence intensity
FVM	Finite volume method
GGCB	Green-Gauss cell based
GGNB	Green-Gauss node based
HPC	High performance computing
HPC	High-pressure compressor
HPT	High-pressure turbine
HWA	Hot wire anemometry
IGV	Inlet guide vane
IPC	Intermediate-pressure compressor
ITA	Iterative time advancement
KH	Kelvin-Helmholtz
LES	Large-eddy simulation
LPT	Low-pressure turbine

LSB	Laminar separation bubble
N-S	Navier-Stokes
NITA	Non-iterative time advancement
NVD	Normalized variable diagram
OP-CL	Operating point - unperturbed laminar
OP-CT	Operating point - unperturbed turbulent
OP-W180	Operating point - perturbed 180rpm
OP-W60	Operating point - perturbed 60rpm
PISO	Pressure-implicit with splitting of operators
POD	Proper orthogonal decomposition
PS	Pressure side
QWSS	Quasi wall-shear stress
ROM	Reduced order model
RST	Reynolds stress tensor
RUB	Ruhr University Bochum
SGS	Subgrid-scale
SIMPLE	Semi-implicit method for pressure linked equations
SIMPLEC	Semi-implicit method for pressure linked equations-consistent
SS	Suction side
SST	Shear stress transport
STD	Standard deviation
TKE	Turbulent kinetic energy
TS	Tollmien-Schlichting
WALE	Wall-adapting local eddy-viscosity

1 Introduction

1.1 Motivation

To face the problem of climate change, the reduction of greenhouse gas emissions is a major goal of modern research. Although the share of aviation in total global CO_2 emissions is relatively low at around 2%, the climate impact of air traffic is much higher, since it is made up not only of direct CO_2 emissions but also of other factors such as nitrogen oxides and water vapour in particular in high air layers. The Intergovernmental Panel on Climate Change (IPCC) estimates that the climate impact of these factors is two to five times higher than that of CO_2. As a consequence, current studies by *Lee et al.* [57] assume that the worldwide overall climate impact of aviation is 4.9%.

A great deal of research has been carried out in recent decades to make aircraft engines more efficient and thus reduce their pollutant emissions. A major factor in increasing the efficiency of aircraft engines is weight reduction. Modern aeroengines like the Pratt&Whitney PW1100G are equipped with a heavy gear box between the fan and the low pressure shaft to spin each at optimum angular velocities. Additionally the high bypass ratio of 12.5:1 results in large fan and casing diameters. These features enable a highly efficient propulsion system, but also cause additional weight that must be saved inside the core engine, in order to avoid creating a snowball effect.

To enable weight savings within the core engine, the number of stages inside the compressor and turbine must be reduced to a minimum. This has the consequence that the individual stages are exposed to increased aerodynamic loads. In the case of the low-pressure turbine (LPT), so-called ultra-high-lift blade profiles are used for this reason. These profile types have such a high aerodynamic load that under certain operating conditions laminar flow separation can occur in the area of the suction-side trailing edge. The fact whether, and if so how quickly, the separated flow is able to reattach to the blade surface is decisive for the efficiency of the expansion process within the respective turbine stage, as a reattachment of a separated boundary layer can significantly reduce profile loss generation. In case of high aspect ratio LPT blades (usually between 3:1 and 7:1) the profile losses are the largest single contributor to the total loss of efficiency [42]. The phenomena involved in this reattachment process, such as linear and non-linear flow instabilities, which trigger the laminar to turbulent transition of the flow inside the separated shear layer are not completely understood until today and cannot be

predicted with sufficient accuracy using current, fast response design methods like RANS or URANS simulations.

It is therefore essential to gain a better understanding of the involved mechanisms in order to improve the prediction accuracy of modern design methods and achieve a target-oriented design process.

1.2 State of research

This chapter provides an overview of some of the most important research contributions in the field of boundary layer transition. To ensure a broad overview, the chapter is divided into two sections. The first section deals with a historical overview of basic research, whereas the second section deals with turbomachine-specific research successes in the field of boundary layer transition.

1.2.1 Fundamental research

In the late 19th century, Osborne Reynolds was the first person to carry out systematic experimental studies of the transition from laminar to turbulent flow within pipe flows. Using the example of his experiments on the flow along a sphere, *Ludwig Prandtl* [96] was able to prove experimentally for the first time in 1914 that the boundary layer near the wall of a body exposed to a flow can be both laminar and turbulent and that the process of boundary layer separation and thus the drag of the body is significantly influenced by this transition process. On the theoretical side, it was *William Mc Fadden Orr* [87, 88] and *Arnold Sommerfeld* [129] who, at about the same time in 1907 and 1908, developed a method of predicting the flow state in which linear two-dimensional perturbations within a viscous parallel flow become unstable. This method is now known as the Orr Sommerfeld method or linear stability theory.

Based on this work, the German researchers *Walter Tollmien* [138, 139] and *Hermann Schlichting* [110, 111, 112, 113], substantiated this theory with their investigations in the 1930s. They found that small disturbances in velocity of any wave length lying within a certain region would be amplified inside the boundary layer, whereas disturbances of shorter or longer wave length would be damped. Thus stability would depend on the wave length rather than the magnitude of a disturbance. However, it took more than ten years before in 1947, *H.L. Dryden* and his co-workers *Schubauer and Skramstad* [117]

were the first to find experimental evidence of wave-like boundary layer instabilities, which exhibited the typical characteristics of stability theory by *Tollmien* [138], using hot-wire anemometry (HWA) measurements. They found these oscillations accidentally during the course of an experiment in which transition from laminar to turbulent flow was being studied on a flat plate as the turbulence in the free stream was being reduced to unusually low values by means of damping screens. In his previous experiments *Dryden* [22] wrongly attributed these fluctuations inside the boundary layer to disturbances within the free flow.

Until the late 1960s there was a real rush in the field of transition research and a number of groups carried out various experiments on laminar-turbulent transition on flat plates and airfoils, which provided a basic understanding of the physical relationships involved. Special attention was paid to the transition within the detached boundary layer via a laminar separation bubble (LSB) (also called separated shear layer transition), which is particularly important when it comes to LPT transition scenarios such as those examined in the present work. This phenomenon occurs when a flow close to the wall is subjected to an adverse pressure gradient (like on airfoils or turbomachinery blades) and was first discovered in 1934 by *Jones* [50] during his experiments on airfoil stall phenomena.

According to *Alam and Sandham* [4] and *Samson and Sarkar* [106], the most notable advancement in understanding the bubble structure and behavior came with the publication of *Gaster* [29] about his studies regarding LSBs and their turbulent breakdown (burst) behavior over a wide range of Reynolds numbers and in a variety of pressure distributions. A more detailed review of the experiments was given by *Young and Horton* [154] and *Horton* [44].

In contrast to the experimental and theoretical studies, the first real numerical studies, which were not based on simplified variants of the Navier-Stokes equations, were not conducted until the 1990s, when the development of computer performance allowed the application of computational-intensive, scale-resolving numerical approaches such as large-eddy simulation (LES) and direct numerical simulation (DNS).

The first attempts to simulate LSBs on a flat plate under an adverse pressure gradient were conducted by *Pauley et al.* [90], *Ripley and Pauley* [99], *Wilson and Pauley* [147]. They realized the needed pressure gradient by the application of a suction through the upper boundary condition, but considered only the 2D incompressible Navier-Stokes equations in their simulations. Nevertheless, they were able to accurately reproduce the main characteristics of the separation found in Gaster's study such as the separation point, the pressure plateau within the upstream portion of the separation bubble, and the

reattachment point. The similarity between the experimental results and the time-averaged, 2D computational results indicated that the low-frequency velocity fluctuations detected by Gaster are primarily due to the motion of large vortex structures. This suggests that large-scale, 2D structures control the bubble reattachment and small-scale turbulence contributes a secondary role [99]. In addition, they found that the "bursting", which Gaster found in his steady experiments, was actually a periodic vortex shedding, which originates inside the separated shear layer and that the shedding frequency was the same as that predicted for the most amplified linear inviscid instability of the separated shear layer [90].

It was at the end of the 1990s, that with the help of increasing computing power, extensive 3D numerical analyses where carried out (see *Alam and Sandham* [2, 3, 4], *Pauley* [91], *Rist* [100], *Spalart and Strelets* [131], *Wilson and Pauley* [147], which in addition to the previous experimental studies enabled an unprecedented description of the transition in a LSB and the participating mechanisms.

Together with the extensive experimental and numerical investigations, which are still carried out today by a large number of researchers from a wide range of disciplines, this history shows in an impressive way how the interplay of different research disciplines has made possible a comprehensive description of the very complex subject area of the flow transition process, which is explained in more detail in section 2.2.2.

1.2.2 Turbomachinery specific research

Since the phenomenon of boundary layer transition plays an essential role in turbomachinery aerodynamics, all of the above-mentioned research contributions can in principle be considered relevant. Nevertheless, depending on the component considered, the essential courses of the transition differ considerably, so that a careful distinction must be made between the scenarios that must be taken into account.

In the case of the LPT flows considered in this work, the transition via a laminar separation bubble is particularly relevant, whether or not in association with turbulent reattachments, depending on the operating point. In the real machine, this transition scenario is additionally influenced by the interaction mechanisms of the neighboring blade rows.

On the experimental side, a comprehensive picture of the turbomachinery relevant transition mechanisms could be drawn by the extensive investigations of *Graveline and Sjolander* [31], *Halstead et al.* [34, 35, 36, 37], *Hodson and*

Howell [42], *Howell et al.* [46], *Lengani and Simoni* [59], *Walker* [141, 142]. In most cases, linear cascades were used as test rigs, which neglect the swirl influence and the radial variation of the blade channel of the real turbomachine, but can reproduce all other characteristics like wake kinematics and secondary flow systems to a high degree [42]. In particular, the investigations of *Halstead et al.* [34, 35, 36, 37] led to a detailed understanding of wake boundary layer interaction, which is still the reference in this area and is explained in more detail in section 2.2.2.4.

In contrast, most of the studies concerning the detailed analysis of the LSB structure are still performed on flat plate configurations. In this case, the required measurement technology, such as particle image velocimetry (PIV) or hot wire anemometry (HWA), can be more easily introduced into the test rig, which allows a detailed description of the structure and dynamics of the transition process like in the contributions of *Dähnert et al.* [21], *Hatman and Wang* [38], *Lengani et al.* [60, 61], *Lyko et al.* [67], *Marxen et al.* [70], *Simoni et al.* [121], *Talan and Hourmouziadis* [135]. The disadvantage of these simplified configurations is that they cannot correctly reproduce the kinematics of incoming wakes (usually realized by bar grids mounted on rotating belts), since the flow deflection through the blade channel is completely neglected, which is why this type of investigation does not provide much benefit in such configurations.

On the numerical side, this shift towards simplified configurations (flat plates) is even more pronounced. This is due to the fact that for the exact prediction of the phenomena involved in the transition process, exact scale-resolving simulation methods have to be used, whose application in simplified geometries facilitates the computational effort and, above all, the post-processing effort of the immense amounts of data. More details on the numerical background and challenges can be found in chapter 3 *Flow simulation*. Some significant contributions to LPT specific numerical transition research on flat plates can be found in the publications of *Alam and Sandham* [2, 3, 4], *Balzer and Fasel* [7], *McAuliffe and Yaras* [74, 75, 76, 77], *Spalart and Strelets* [131], *Yang* [151].

Close-to-reality scale-resolving numerical investigations in LPT configurations are rare. There are publications in which LPT flows (mostly cascade configurations) have been investigated. In this context, the contributions of *Cui et al.* [19], *Michelassi et al.* [80, 81], *Müller-Schindewolffs et al.* [82], *Sandberg et al.* [107] are particularly worth mentioning. In most cases, however, the results are focused on demonstrating the feasibility of the study, analyzing the differences to conventional simulation methods and the comparison of computational effort, while a 3-dimensional analysis of the flow struc-

tures involved in the transition process was not presented. At this point, the disadvantage of such scale-resolution simulation approaches becomes clear, which is the high effort for the analysis of the immense amounts of data generated by such types of simulations. This leads directly to the objectives of this work.

1.3 Objective of this work

The work presented in this thesis was carried out in the context of the DFG joint project PAK948: "Near-wall flow in turbomachinery blading" within subproject 4: "Influence of periodic wakes on the near-wall unsteady flow in axial turbine annular cascades".

Together with the detailed transient experimental investigations (see *Sinkwitz* [127]), a unique basis for the validation of the numerical results presented in this work could be created, on the basis of which an in-depth phenomenological analysis of the mechanisms involved could be realized.

In the context of the near-wall transition phenomena in the rear suction-side area of the investigated profile, the model created in this work mainly aims at the phenomena explained in section 2.2.2, which are still today mainly investigated on simplified flat plate experiments & simulations. With the help of the present investigations in a more realistic application case, their transferability is to be verified and further insights are to be gained, which cannot be obtained in the case of simplified experimental investigations. Thus, this work aims to bridge the gap between the study of extremely simplified configurations and the priceless computation of real machines by treating an experimentally well-characterized configuration that is within the range of LES but retains the main features of a turbomachinery flow.

This directly leads to the objectives of this work:

- Development of a detailed numerical model for the analysis of wake-boundary layer interaction mechanisms based on the LES approach with special emphasis on the following aspects:
  - Geometry and mesh creation.
  - Derivation of the boundary conditions specific to the test-rig.
  - Realization of an economic data output, which allows for an efficient analysis of the involved transient flow processes.
- Analysis of the data generated by the numerical model by the application of different post processing techniques with the aim of:

- Verifying the numerical predictions against selected experimental data sets.
- Elaborating the fluid mechanical relationships in the transitional region on the basis of time-averaged and time-exact data with special emphasis on:
  - Characterization of the transition process for the unperturbed case without incoming wakes ("clean inflow") with special reference to the phenomena known from the literature concerning flat plate flows.
  - Elaboration of the influence of the turbulence of the free flow on the transition process.
  - Working out the influence of the incoming wakes on the transition process

2 Theoretical background

2.1 Aeroengines

This chapter covers the most important parts of the theory of aircraft engines, which are considered important for understanding this work. It starts with a short introduction to the functioning of aircraft engines using a simple turbojet engine as an example. This is followed by a more detailed examination of the turbine's operation, focusing on the aerodynamic relationships within the stage array.

2.1.1 Operating principle

The operation of aircraft engines is based on an open cycle process in which the compressor is driven by the turbine via a shaft.

In the first step the working fluid (atmospheric air) is sucked into the engine inlet. Inside the compressor system, the air is compressed to the required pressure level and then combusted inside the combustion chambers with the addition of fuel (usually kerosene), causing it to expand rapidly. The air is finally expanded through the turbine, which converts the energy of the flow into mechanical energy and drives the compressor system. But only part of the flow energy, which was provided by the compressor and the combustion chamber, is used within the turbine to drive the shaft (and all additional utilities such as pumps and generators). The rest of the energy is converted into velocity downstream of the turbine inside the exhaust nozzle as the fluid ideally expands to ambient pressure. Thus, the crucial aspect of why an aircraft

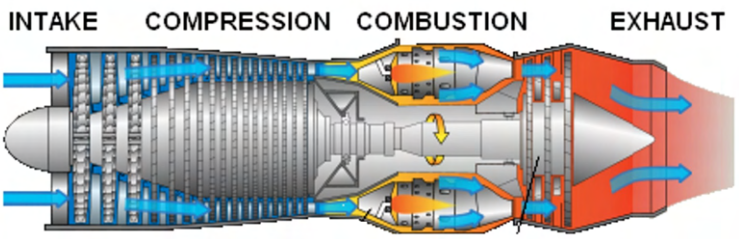

Figure 2.1: 2-dimensional illustration of a simple turbo jet engine (own representation based on [58]).

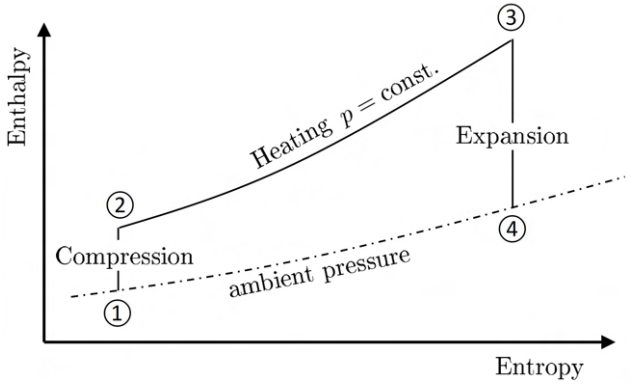

Figure 2.2: Schematic drawing of the ideal Joule cycle in the *h*-*s* diagram.

engine generates thrust is that the air before entering the turbine provides more energy in the form of pressure and thermal energy than the turbine needs to drive the compressor system.

This is made possible by the phenomenon known as isobaric divergence, which becomes clear when the previously described circular process of an aircraft engine is visualized within the enthalpy-entropy (*h*-*s*) diagram. Figure 2.1 shows a schematic drawing of the actual process, which is called Joule or Bryton cycle. In its ideal form, the air is first compressed isentropically (1→2). Then an isobaric combustion takes place (2→3) followed by an isentropic expansion (3→4). In this case, the process shown is ideal, which means that no losses are considered during compression and expansion ($\Delta s = 0$). Although this method of representation neglects various aspects of the real process, such as flow losses, heat conduction losses or mechanical losses, it is clear that due to the divergence of the isobars (2→3 and 1→4), more energy in terms of Δh can be released during expansion than is needed for the compression process. Therefore it is possible that the excess energy can somehow be used for propulsion of the aircraft. The methods of how this energy is used are described more closely in the following.

2.1.2 Turbines

As described in the previous section, the turbine serves to convert the energy of the flow into mechanical energy by means of rotation. It drives the shaft and thus the compressor system and all utilities connected to the shaft, such as generators and pumps. Unlike the simple turbojet engine described

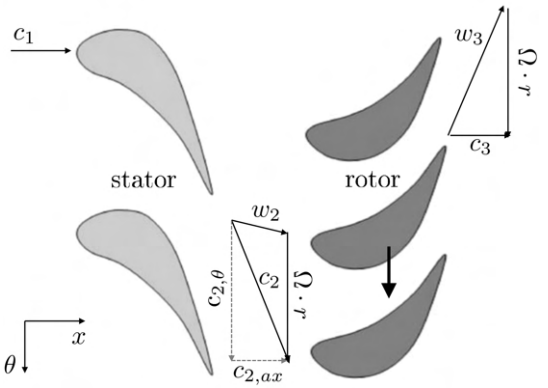

Figure 2.3: Schematic drawing of the velocity components inside a radial plane of a typical axial turbine stage.

above, modern engines consist of several compressor and turbine components, namely the high-, medium- and low-pressure parts, each of which can be mounted on up to three separate shafts. In this case the LPT usually drives the so-called fan, while the medium- and high-pressure turbine drive the medium- and high-pressure compressor.

To enable the energy within the flow to be converted into a rotational movement of the shaft, standard turbine stages consist of two rows of blades, a stator row and a rotor row. A schematic representation of a typical axial turbine stage is depicted in Fig. 2.3.

The rotor is the mechanical element that extracts the energy from the working fluid and converts it into shaft work. In order to make this process as efficient as possible, the upstream stator row expands and accelerates the flow, while it provides it with a corresponding swirl ($c_{2,\theta} > 0$), so that the inflow conditions of the downstream rotor are satisfied.

For the design process as well as for the evaluation of the performance and efficiency of a turbine stage, the velocity triangles, which are shown in Fig. 2.3. are of essential importance. In order to calculate the relative inflow of the rotor blades w_2, it is necessary to transform the velocities from the absolute system into the relative system of the rotor. For this purpose, the circumferential speed $u = \Omega \times r$ must be subtracted from the rotor inflow speed c_2 in the absolute system. Conversely, at the outlet of the rotor, the rotational speed $u = \Omega \times r$ must be added to the relative outflow speed w_3 to obtain the absolute outflow speed c_3.

Based on this simple kinematics, the specific work done by the rotor can already be calculated:

$$\Delta h_t = \frac{-M\omega}{\dot{m}} = \omega(c_{1,\theta}r_1 - c_{2,\theta}r_2), \tag{2.1}$$

with the moment of momentum equation

$$M = \dot{m}(c_{2,\theta}r_2 - c_{1,\theta}r_1). \tag{2.2}$$

When the inlet radius and outlet radius of the rotor are the same, i.e. $r_1 = r_2 = r$, then Eq. (2.1) can be simplified to

$$\Delta h_t = \omega r(c_{1,\theta} - c_{2,\theta}) = u\Delta c_\theta. \tag{2.3}$$

So specific workload at this case is only depending on the circumferential speed of the rotor and the difference of swirl between rotor-inlet and -outlet.

2.1.3 Development trends of low-pressure turbine design

Unlike the simple turbojet engine (described in section 2.1.1), where the remaining fluid energy downstream of the turbine is converted into velocity inside the exhaust nozzle to generate the highest possible thrust, modern turbofan engines use most of the remaining energy inside the LPT to drive a large fan in front of the compressor. The task of the fan is not to compress the air, but to moderately accelerate as much air as possible via the so-called bypass flow and thus to provide the main part of the thrust of the total engine. These two different ways of generating thrust can be illustrated using the simplified net-thrust formula ($\dot{m}_{\text{fuel}} << \dot{m}_{\text{air}}$) as an example:

$$F_N = \dot{m}_{\text{air}}(c_{\text{exhaust}} - c_{\text{intake}}). \tag{2.4}$$

It is obvious that the same amount of thrust can be generated either by a moderate mass flow with a high velocity difference between intake and exhaust of the engine (turbojet), or by a moderate acceleration of a much larger air mass flow (turbofan). The latter enables not only a higher efficiency of the entire engine but also considerably reduced noise emissions, which is why today's passenger planes are mainly equipped with turbofan engines.

To achieve this high efficient propulsion, the bypass ratio (BPR) of modern aircraft engines is up to 12.5:1 (PW1100G), which means that about 93% of the air mass flow is blown through the engine's bypass by the fan, generating up to 80% of the total thrust [46], and only about 7% of the mass flow is used

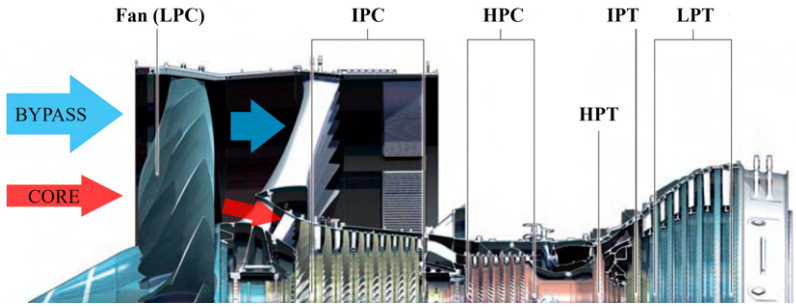

Figure 2.4: Cross section of the (three shaft) high bypass Trent 1000 turbofan engine (own representation based on *Schobeiri* [116]).

for the actual cyclic process inside the core engine. In the near future, the trend will be towards even higher BPRs of up to 16:1 (EU ENOVAL research program), which envisages fan diameters of up to 3.90 m and clearly underlines the importance of efficient LPT operation in the development trend of modern aircraft engines, as the LPT is responsible for driving the fan.

The relevance of the low-pressure system with regard to a possible optimization potential becomes additionally clear when the proportions of the individual systems are compared. Figure 2.4 shows a cross section of a modern Trent 1000 high bypass engine (BPR: 11:1) in a three shaft configuration. It is remarkable that both the eight-stage intermediate-pressure compressor (IPC) and the six-stage high-pressure compressor (HPC) are each driven by only one corresponding turbine stage (IPT/HPT). The large fan, on the other hand, is driven by a six-stage LPT.

This can be explained by the limited work output per stage in the low-pressure part of the turbine, because according to Eq. (2.3) it depends on the circumferential speed of the rotor, and thus on its diameter and rotational speed. However, as the fan has to be operated at low rotational speeds due to its large diameter and the subsequent high tip-speed, the LPT speeds are also limited if there is no gearbox in between. Additionally the diameter of the LPT is limited by the bypass channel.

This has the consequence that for this types of engines 20-30% of the total weight can be attributed to the LPT [20], which in turn has considerable potential for optimization, especially in view of the trend towards ever higher BPRs.

The optimization potential becomes additionally clear when considering the influence of a theoretical efficiency improvement on the specific fuel con-

Table 2.1: Components performance exchange to SFC for a civil aircraft at cruise conditions (Mach 0.8, 10,000 m altitude) [150]

1% change of efficiency of	Fan	LPC	HPC	HPT	LPT
Percent change in specific fuel consumption (SFC)	0.62	0.22	0.66	0.82	**0.96**

sumption (SFC) of an aircraft. Table 2.1 shows the components performance exchange to SFC for a civil aircraft at cruise conditions (Mach 0.8 at 10,000 m altitude) according to *Wisler* [150]. It shows that an LPT performance increase of 1% correlates to a reduction of SFC of almost 1%, which is more than the LPC & HPC system combined. Nevertheless, the course of the last 50 years, during which only about 10 percentage points of efficiency increase could be achieved, suggests that an increase in efficiency in the field of LPT is not easy to achieve. Especially because with efficiencies of over 90%, values have already been reached which will be difficult to improve in the future. [46].

Based on the above, it is evident that one of the main development trend aims at reducing the weight of the LPT, as a 17% weight reduction reduces operating costs by 1%, resulting in an effective cost reduction of approximately $200,000 per aircraft a year [150].

Two approaches are being pursued to achieve this:

1. Decoupling of the low pressure system:
   Modern engine concepts rely on decoupling the speeds between the LPT and fan. With the so-called geared turbofan concept (e.g. PW1100G) it is therefore possible to realize a fast rotating LPT with a reduced number of stages, which enables a more efficient operation and a subsequently lower SFC.

2. Blade count reduction:
   A further measure is to reduce the number of blades in the individual stages, which can be as much as 2000 in conventional LPTs. As a result of the blade count reduction, the remaining blades must be subjected to an increased aerodynamic loading in order to ensure the same LPT work output.

Both methods not only allow weight savings, but also significantly reduce the production and maintenance costs of an engine. However, the focus of this study will be on the consequences of the second point, as the increased aerodynamic load on the individual blades within the LPT due to the re-

duced number of blades leads to complex flow phenomena which, especially under the influence of interaction mechanisms, are not yet fully understood and therefore cannot be adequately represented within the design process using conventional methods. A detailed description of these phenomena is given in the following section.

2.1.4 The role of profile losses in low-pressure tubines

If losses in aircraft engines are mentioned, they can generally be divided into two categories:

- **External losses**: These include, for example, mass losses in the form of leakage, or mechanical losses in the form of friction in bearings and seals. The external losses do not influence the course of the state change and are therefore not part of this work.
- **Internal losses**: This includes all losses that occur inside the fluid in the form of flow losses and therefore influence the course of the state change, namely:
  - *Profile losses*
    The profile losses include all losses due to boundary layer effects, i.e. flow separation as well as flow mixing inside the wake.
  - *Secondary flow losses*
    Vortex formation due to the influence of pressure gradients on the boundary layer areas at hub and casing within the blade passage.
  - *Gap losses*
    Vortical structures and mixing zones originating between stationary and rotating components
  - *Friction losses*
    Due to viscous effects at the blading and at the hub and casing.

The focus of this work is on the mechanisms that determine the profile losses, so only these will be discussed in more detail below. A detailed description of the other loss mechanisms is provided in the textbook of *Bräunling* [14].

In the field of LPT, profile losses make up by far the largest part of the overall efficiency loss [42]. This is mainly due to the fact that the blades in the LPT area have a very high aspect ratio, since the gas in this area has already expanded in the upstream turbine section and thus has a higher volume flow rate. As the exit Mach number of the LPT is limited to approx. 0.4-0.6 [155], these facts lead to an increased cross section of the flow path and thus to a high aspect ratio of the blades between 3:1-7:1 [42].

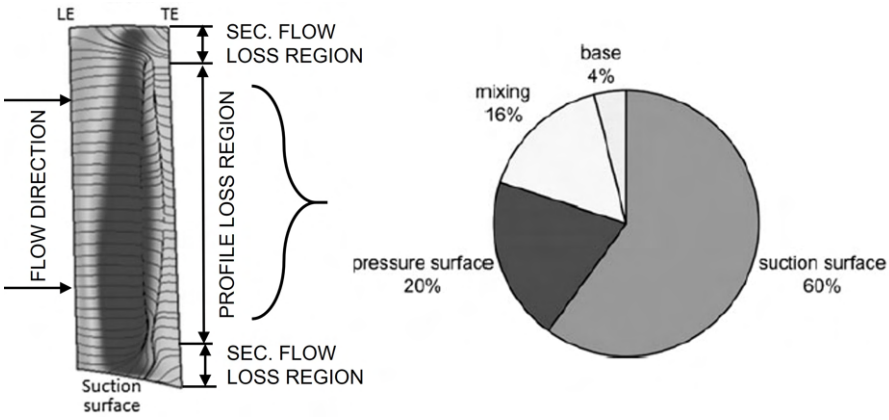

Figure 2.5: Numerically generated streamlines along the suction surface of an LPT vane (left, own representation based on [155]); percentage distribution of profile loss (right, own representation based on [20]).

Figure 2.5 (left) clearly illustrates this fact, using numerically generated wall streamlines on the suction side of an LPT vane [152]. Here, the area dominated by profile losses extends over a much larger part of the vane height than the area influenced by secondary flows. Another reason why the profile losses dominate is due to the LPTs operating range. The Reynolds numbers are the lowest in the entire engine due to the relatively low blade circumferential speeds and the low flow Mach numbers. In addition, very high turning angles (between 100°-110° or even higher) have to be realized due to the highly loaded blades in order to guarantee the required energy conversion (cf. Eq. (2.3)). All these aspects lead to the fact that large areas of the profile surface have laminar boundary layers, which in case of the suction side are very unstable due to the presence of an adverse pressure gradient and therefore tend to separate from the blade surface. The fact whether, and if so at which point, the suction-side boundary layer separates from the blade surface is of essential importance with regard to the profile losses and thus efficiency of the expansion process. What makes the design of the profiles even more difficult is the wide range in which modern aircraft engines must operate. The typical Reynolds number range in the case of LPT extends from about 100,000 at cruise condition to about 400,000 at take off condition, as depicted in Fig. 2.6 (left). Depending on the respective blade design, very different flow scenarios can occur on the suction side depending on the op-

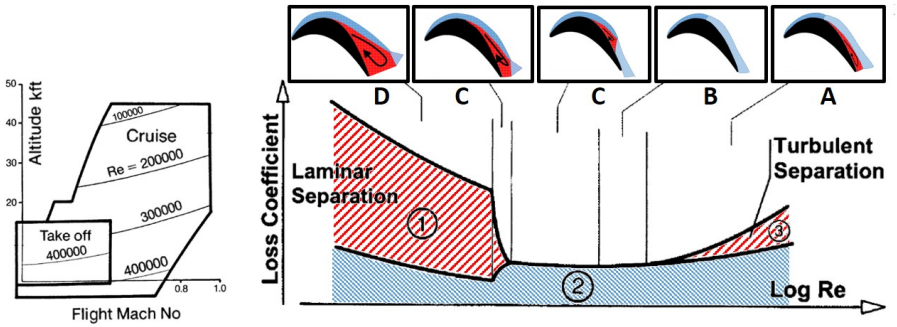

Figure 2.6: Variation of Reynolds number in an LPT for a civil aircraft flight envelope (left, own representation based on [45]); Loss coefficient for different types of flows (left, own representation based on [135]).

erating status of the LPT. These are illustrated in Fig. 2.6 (right) in a diagram showing the course of the loss coefficient over the Reynolds number.

The blue coloured areas represent the friction losses inside the shear layers, whereas the red highlighted areas represent the additional losses due to flow separation. As expected, the laminar boundary layer causes less friction loss than the turbulent boundary layer, but it is also very susceptible to flow separation, which at very low Reynolds numbers (range C and D) means that in addition to the friction loss, separation losses are added because the flow is not able to reattach to the blade surface. If the flow succeeds in reattaching turbulently to the blade surface (area C), which happens via a so-called laminar separation bubble, no separation losses occur, and the resulting total loss is thus drastically minimized. If the Reynolds number is increased even further, the transition takes place within the attached boundary layer (area B), which in turbo-machinery is usually achieved by means of the so-called bypass transition. Also in this region, the resulting losses are very low, but regarding LPT flows, this case is more likely to be associated with the high Reynolds numbers at take off. In the case of turbulent flow separation (area A), which can occur e.g. due to an increase in the adverse pressure gradient, the additional separation loss is much lower than with laminar flow, which is due to the fact that the turbulent flow separates later and more pressure recovery has already taken place.

In summary, flow separation, without reattachment, whether laminar or turbulent, should be avoided if possible to ensure efficient operation of the LPT.

However, since the risk of separation increases with increasing aerodynamic load, a precise knowledge of the boundary layer development along the suction side of such LPT profiles is essential. This includes the development of the laminar boundary layer as well as its transition into the turbulent state, either directly via the so-called bypass transition or within a detached shear layer via a laminar separation bubble.

2.2 Boundary layer flows & transition

2.2.1 Boundary layer parameters

Although the flow in LPT is characterized by strong turbulence and interaction mechanisms, it can be laminar or transitional within the boundary layers, over large areas of the blade. In the following, the physical aspects, which can be used to describe and analyze a boundary layer theoretically, will be explained in more detail. The goal is to identify parameters that can be used to evaluate the state (laminar/transitional/turbulent) of the boundary layer. A detailed description is given in the textbook of *Schlichting et al.* [114].

An important parameter, which is of essential relevance in connection with boundary layers, is the local shear stress τ_w or the non-dimensional friction coefficient:

$$c_\mathrm{f} = \frac{\tau_\mathrm{w}}{\frac{\rho}{2}c_e^2}, \quad \text{with} \quad \tau_\mathrm{w} = \mu \left(\frac{\partial u}{\partial y} \right) \tag{2.5}$$

where c_e is the unperturbed velocity at the edge of the boundary layer, u is the wall-parallel velocity component and y is the wall wall-normal coordinate.

The course of the non-dimensional friction coefficient is shown schematically in Fig. 2.7 using the example of a laminar turbulent transition over a detached shear layer, caused, for example by an adverse pressure gradient.

The wall friction, which is caused by the laminar boundary layer, decreases continuously to zero until the separation point. Within the subsequent separation bubble, backflow areas circulate, which result in negative wall shear stress. Afterwards the flow again reattaches turbulently, which in turn causes positive wall shear stress. However, due to the stronger exchange of momentum caused by the turbulent fluctuations inside the boundary layer, the friction rises well above the level of the laminar boundary layer.

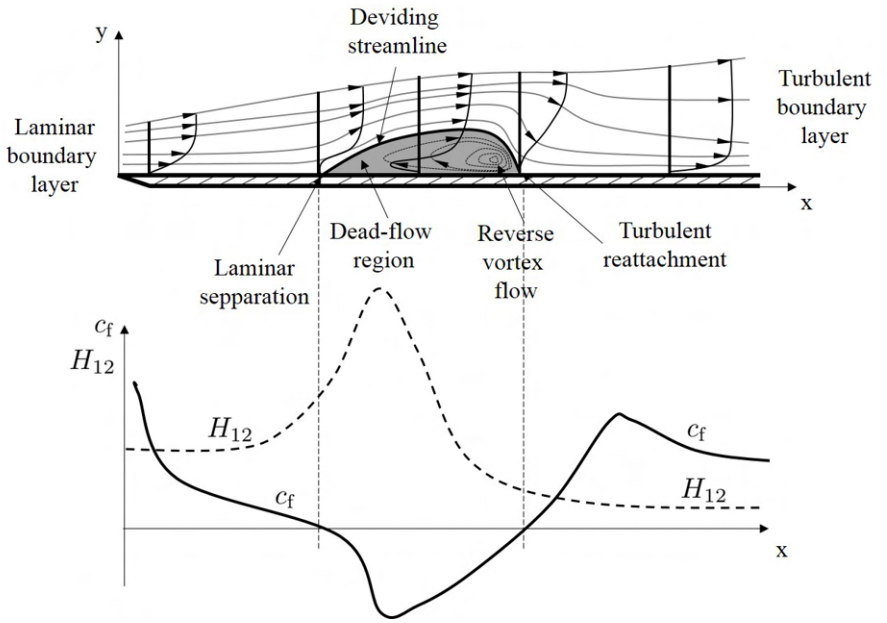

Figure 2.7: Schematic drawing of the development of the non-dimensional friction coefficient c_f and shape factor H_{12} by the example of a seperated shear layer transition with turbulent reattachment.

The two zero crossings of the friction coefficients are therefore a clear indicator for the beginning and the end of the separation bubble. Whether the transition within the detached shear layer is completed and whether the reattached boundary layer is turbulent is indicated by the level of friction increase downstream of the bubble.

A further quantity which can be used to identify the boundary layer transition is the form factor of the boundary layer H_{12}. It is defined as the quotient of the displacement thickness δ^* and the momentum thickness θ:

$$H_{12} = \frac{\delta^*}{\theta}. \tag{2.6}$$

The displacement thickness is a correct and fluid mechanically interpretable parameter for the thickness of the boundary layer. It is a measure for the displacement effect of the boundary layer and reads:

$$\delta^* = \int_{y=0}^{\delta} \left(1 - \frac{U}{U_e}\right) \mathrm{d}y, \tag{2.7}$$

with the boundary layer thickness δ.

The momentum thickness on the other hand is a measure for the momentum loss in the boundary layer:

$$\theta = \int_{y=0}^{\delta} \frac{U}{U_e} \left(1 - \frac{U}{U_e}\right) \mathrm{d}y. \tag{2.8}$$

These two values are preferred as comparison values. This is because the boundary layer thickness is not clearly defined, as it approaches asymptotically to the velocity in the outer flow and thus no exact limit can be defined. In order to avoid this problem, the boundary layer thickness δ in the literature is therefore usually approximated by the wall distance δ_{99}, which is given by the distance where $U/U_\infty = 0.99$ is reached.

The course of the shape parameter is also shown in Fig. 2.7. Different from the friction coefficient, it is higher in the area of laminar flow than in the area of turbulent flow and the onset of the separation bubble is characterized by a strong increase of the shape parameter.

In the literature [110], absolute values of the shape parameter are given for certain special cases. For example, the value

$$H_{12,\mathrm{lam}} = 2.59 \tag{2.9}$$

can be calculated for a laminar boundary layer without pressure gradient using the blasius equation. For the turbulent boundary layer without pressure gradients, the value

$$H_{12,\mathrm{turb}} = 1.28 \tag{2.10}$$

is obtained with the help of the 1/7 power law. An increase of the form factor to values above $H_{12} \approx 4$, however, indicates a separation of the boundary layer.

Since this test case is a complex flow process in which pressure gradients and transient effects play a significant role, these absolute values can at best

serve as a guideline, while a qualitative similarity can be more likely to be expected.

The course of boundary layer transition is a very complex phenomenon, which describes the change of a flow from the laminar to the turbulent state. It is characterized by the occurrence of different mechanisms, which interact with each other and additionally react very sensitively to external influences such as free stream turbulence intensity (FSTI), surface roughness, pressure gradients or periodic excitation. The interplay of these influences can affect the course of the transition process in such a way that it completely changes its character, which will be explained in more detail below. The focus here is not only on explaining the phenomenology and mechanisms involved, but also on providing a brief overview of the most important contributions over the past decades of fundamental boundary layer research. To this end, a brief summary of the historical course of transition research will be given, highlighting the complementary interaction of three research disciplines, namely experimental, theoretical and numerical activities.

2.2.2 Transition mechanisms

Although, owing to the prevailing flow conditions, the boundary layer transition in the area of the suction side of LPT blading mostly takes place via the so-called separated shear layer transition and the so-called wake induced transition, the mechanisms of natural and bypass transition, which are typical for attached flows, shall also be discussed here. This is of great importance because these mechanisms are included as fundamental elements in both cases and thus make a comprehensive understanding possible in the first place.

2.2.2.1 Natural transition

If wall-bound flows are exposed to very small external disturbances, the transition process usually takes place via the so-called natural transition. In the literature this is attributed to FSTI levels of less than 0.5%.

The course of natural transition is illustrated in Fig. 2.8 on the example of a flat plate boundary layer at zero incidence. Inside the laminar boundary layer (1) transition is initiated by 2-dimensional (2D) disturbances, the so-called Tollmien-Schlichting (TS) waves (2), which are also called primary instabilities. These TS waves are followed by 3-dimensional (3D) instabilities, which are classified as secondary instabilities and cause highly three-dimensional flow structures (typical Λ-structures), which form both in the

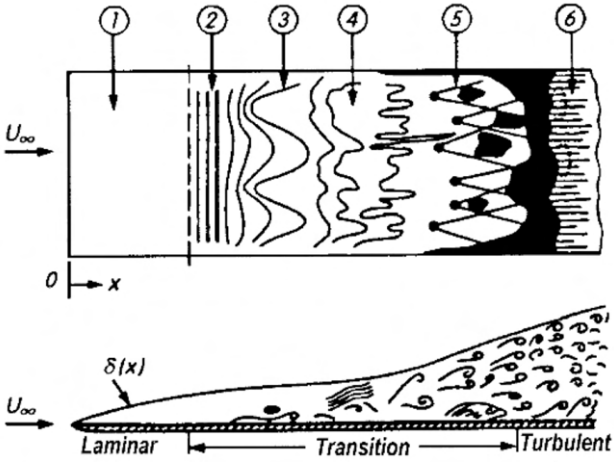

Figure 2.8: Sketch of laminar-turbulent transition in the boundary layer on a flat plate at zero incidence, adopted from *Schlichting et al.* [114]

flow direction and in the cross flow direction (3)-(4). In the last transition stage, the so-called turbulent breakdown, these large scale 3D vortex structures collapse into smaller structures and form turbulent spots (5), which then grow together and finally form a turbulent boundary layer (6). [114]

According to *Yang* [153], natural transition is the most extensively researched area compared with the other two categories of transition. A large part of the research work was already carried out in the first half of the 20th century based on the linear stability theory and some experiments (see above) and hence the transition process is relatively much better understood.

A detailed description of the individual five stages within the process of natural transition is provided by *Schmid and Henningson* [115] and *Yang* [153]:

1. Receptivity stage: This stage is associated with the initiation of disturbances in the flow. Receptivity includes the process of how (often) stochastic perturbations are projected into growing eigenmodes or how they otherwise cause perturbations within the boundary layer.

2. Linear growth stage (primary instability): This stage describes the amplification of small disturbances, due to a socalled primary instability (2-dimensional TS waves) until they reach a size where nonlinear effects become important.

3. Nonlinear saturation: Once a disturbance has reached a finite amplitude, it often saturates and transforms the flow into a new, possibly steady state. Only in a few cases does the primary instability lead the flow directly into a turbulent state (bypass transition).

4. Secondary instability: The new steady or quasi steady flow becomes a base flow on which secondary instabilities can grow (development of 3D flow structures). This secondary instability can be seen as a new instability of a more complicated flow. This stage of the transition process is in many cases more rapid than the stage where primary instabilities prevail.

5. Breakdown stage: The last stage is the breakdown stage where nonlinearities and/or higher (symmetry-breaking) instabilities excite an increasing number of scales and frequencies in the flow. This stage is often more rapid than both the linear stage and the secondary instability stage. The physics behind this process are highly difficult and a detailed analysis is usually done using physical or numerical experiments.

The subdivision of the transition process into the five stages described above is an idealization, which is not always fulfilled, since a clear distinction between these stages cannot always be guaranteed. Nevertheless, it provides a solid framework for the description of the transition process.

2.2.2.2 Bypass transition

When the FSTI level exceeds 1% the transition process typically occurs more rapidly and the 2D instability stage happening within the natural transition process is bypassed. The term "bypass transition" was firstly introduced in 1969 by *Morkovin* [83], when he noted "Apparently, we can bypass the TS-mechanism altogether if we can replace it with another strongly amplifying mechanism." In this quote the 'TS-mechanism' refers to the exponential growth of Tollmien-Schlichting (TS) waves.

The course of bypass transition can be summarized as follows:

1. Due to the increased FSTI, the boundary layer experiences a low-frequency excitation due to disturbances which penetrate the boundary layer from the free flow. These disturbances undergo an algebraic growth, which is also called transient growth or non-modal growth. In this case, non-modal means that this perturbation does not emerge as one of the eigenmodes of the solution of linear theories based on the Orr-Sommerfeld equation. These disturbances cause the formation of streamwise elongated vortex structures of high and low speed fluid, which are called boundary layer

streaks or also Klebanoff streaks, after P. S. Klebanoff who investigated this phenomenon first (*Klebanoff* [51], *Klebanoff et al.* [52]) and described them as a periodic thickening/thinning of the boundary layer.

2. The laminar boundary layer disturbed by these streaks is sensitive to additional instabilities, so that the amplitude of the streaks increases downstream. The transition process often takes place at the outer edge of the boundary layer as a result of interactions between high frequency disturbances in the free flow and the low velocity fluid within the streaks.

3. The formation of turbulent spots occurs directly in this process without any secondary instabilities as in the natural transition. A merging of these turbulent spots finally forms the fully turbulent boundary layer.

2.2.2.3 Transition in laminar separation bubbles

If a boundary layer detaches from the wall due to geometric aspects or adverse pressure gradients, transition can occur within the resulting detached shear layer. If the flow reattaches to the wall a laminar separation bubble (LSB) is formed. Within highly loaded, LPT stages, which are the subject of this thesis, this is the most common mechanism besides the wake influenced transition, so the focus in the following will be on these two variants of transition.

In principle, transition in a detached shear layer can take place according to both of the basic principles explained above, i.e. in a natural way or as a bypass transition, as stated by *Walker* [142] in 1993.

The aim of the following section is to describe the mechanisms involved in the transition via LSBs at low and increased FSTI. In addition, the most relevant research contributions of the past few years will be discussed to give an overview of the current state of research in this field.

Transition process under low free-stream turbulence

At low FSTI levels, the transition is mainly driven by receptivity of the detached laminar shear layer to small disturbances via an inviscid instability mechanism called Kelvin-Helmholtz (KH) instability, named after the two physicists Lord Kelvin and Hermann von Helmholtz, who discovered this mechanism in the late 19th century. Initially these instabilities are two-dimensional in nature and grow inside the separated shear layer with an amplification rate that is normally much higher than that of the TS-waves, which determine the natural transition in the attached boundary layer case.

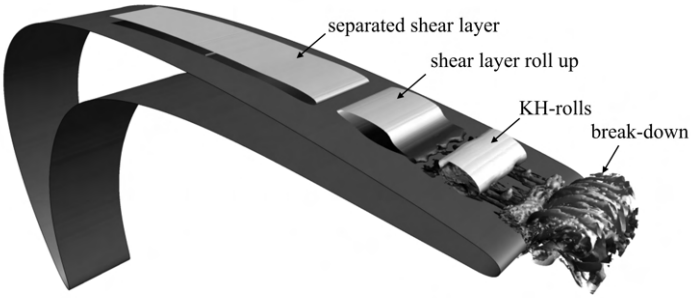

Figure 2.9: Illustration of the KH shear layer roll-up mechanism at low FSTI levels on the example of the underlying test case.

This instability was clearly identified by many experimental and numerical studies since the early 2000s (*Dähnert et al.* [21], *Lang et al.* [55], *McAuliffe and Yaras* [74, 75, 76, 77], *Satta et al.* [108], *Serna and Lázaro* [119], *Spalart and Strelets* [130], *Yang* [152]).

Further amplification of the KH instability (occurring at the most amplified frequency) results in the roll-up of the shear layer and the subsequent formation of spanwise vortices which are often referred to as "KH-rolls" (cf. Fig. 2.9). As the vortices saturate and shed downstream of the separated shear layer, smaller vortical scales emerge, which indicates that a transition to small-scale turbulence is initiated. This process is often described as a "breakdown" of these coherent structures (*McAuliffe and Yaras* [77]).

The dominant instability has been shown to scale with the Strouhal number Sr based on the momentum thickness θ, the velocity at the edge of the boundary layer at the separation point U_{es} and the frequency f_{KH} at which the KH vortex shedding occurs:

$$Sr_{\theta_s} = \frac{f_{\mathrm{KH}}\theta_s}{U_{\mathrm{es}}}. \tag{2.11}$$

It is important to mention that despite the dominance of the KH-instabilities, especially in case of a low FSTI, additional TS-instabilities may occur, which underlines the importance of the natural transition phenomenon. Although these have a significantly lower growth rate, they can interact with the KH-instabilities and thus significantly influence the transition process and especially the turbulent breakdown, as reported by *Lang et al.* [55], *McAuliffe and Yaras* [74, 75], *Roberts and Yaras* [104].

The understanding of the transition process in a separation bubble is relatively limited compared with that for an attached boundary layer, and in the transition process described above only the first stage, the primary instability (2D) stage, is well understood. But since turbulence is inherently three-dimensional, there must be (secondary) mechanisms which produce 3D disturbances in a LSB.

Even today there is no general agreement regarding the secondary instabilities, despite many studies in the past two decades like the numerical (DNS) studies of *Maucher et al.* [71, 72], who investigated a forced LSB transition occurring on a flow along a flat plate. They found that the phase with reverse flow inside the LSB is decisive for the secondary temporal amplification, as it generates small regions of high-shear with respect to 3D perturbations, which are transported downstream by the large scale 2D motions. After these 3-dimensional modes gain large amplitudes transition sets on. They also state that "The 3D disturbances pierce the detached shear layer from underneath and destroy it very rapidly, thus leaving spanwise rolls of turbulent flow".

Based on the linear stability theory, *Rist and Maucher* [102] examined the effect of profile shape on the stability of velocity profiles with reverse flow near the surface, and found two regions in which the associated instabilities show differing characteristics. The outer region of the detached shear layer is unstable via an inviscid instability with low Reynolds number dependence. Near the wall, another instability occurs in the area of the reverse flow region, which is highly dependent on the Reynolds number. They further found that dominance of one mode over the other depends on the distance of the zero-velocity point from the wall as well as on the level of reverse flow near the wall. Greater distance from the surface promotes inviscid instability in the outer part of the shear layer, while also increasing the frequency and growth rate. Conversely, a smaller distance from the surface causes a dominance of the inner (viscid) instability with an associated reduction in frequency and an increase in growth rate.

Extensive experimental and numerical (DNS/LES) studies have also been conducted at Carleton University in Canada. Here, the transition within an LSB on a flat plate flow exposed to an inverse pressure gradient was taken into account. They found a strong coupling between the TS-waves and the inviscid KH-instabilities (*McAuliffe and Yaras* [74], *Roberts and Yaras* [104]), which affects the shedding process of the spanwise KH-vortex structures. They state that areas of high-shear, which build in between these coherent rolls cause a time-periodic cross-stream mixing and a subsequent breakdown to turbulence, which is dominated by KH-instabilities but also considerably

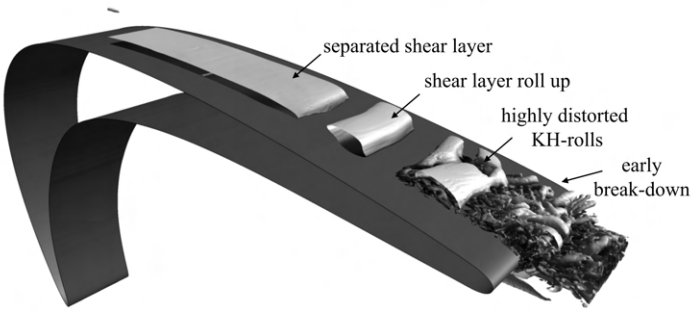

Figure 2.10: Illustration of the KH shear layer roll-up mechanism at elevated FSTI levels on the example of the underlying test case.

affected by the TS-waves. A comparison of the numerical results of *McAuliffe and Yaras* [77] with the velocity profiles of *Rist and Maucher* [102] revealed a predominance toward the outer-layer inviscid instability. Nevertheless, they could also identify coexistence of near-wall viscous instability mechanisms.

Transition process under elevated free-stream turbulence

Besides the wake induced transition, which will be described in the following section, this transition scenario is the most relevant, when it comes to LPT boundary layer transition. This is caused by the relatively high FSTI within LPT stages, which according to *Halstead et al.* [34] can be up to 5%.

Just as in the previously described case of the attached bypass transition, the receptivity of the laminar boundary layer leads to a non-modal growth of low-frequency disturbances from the free flow. As a consequence, Klebanoff structures are formed, which interact with the detached shear layer and can thus cause different transition scenarios, depending on their severity. In general this results in a reduction of the mean LSB length and thus an acceleration of the transition process, as many researchers reported [7, 48, 56, 59, 60, 85, 121]. However, what this looks like in detail depends heavily on the severity of the FSTI elevation.

In the lower range of elevated FSTI, the Klebanoff streaks first distort the spanwise oriented KH-rolls, increasing the 3-dimensional turbulence level and ultimately accelerating the breakdown of coherent structures toward small turbulent scales (cf. Fig. 2.10).

Recent studies of different research groups ([7, 48, 152]) revealed that in this case the Klebanoff-streaks are not directly connected to the turbulent flow region, but end already upstream of it. They also demonstrated the presence of the typical signatures of the KH instabilities using frequency based and modal based (POD) analysis methods, showing that the transition is still driven by the primary instability mechanism up to FSTI levels of 3%.

In the higher range of elevated FSTI the Klebanoff-streaks connect with the turbulent flow region causing an enhanced break-down to 3-dimensional small scale turbulence. While some researchers still observe the KH-instability caused, highly distorted shear layer roll-ups ([7, 48, 152]), some other groups found the direct formation of turbulent spots inside the separated shear layer. These spots are generated through the interactions of the separated free shear layer with the streaks via a localized secondary instability [77] whose frequency signature closely matches that of the KH-instability.

Nevertheless, although some researchers also speak of "bypass transition" in the context of the separated shear layer transition under elevated FSTI, it is important to note that this does not mean that the linear shear layer instability mechanism, the KH instability, is skipped, as it is the case in the attached transition scenario with the TS mechanism. Instead, "bypass transition" here means that the receptivity stage of disturbances, which enter the separated shear layer and lead to the shear layer roll-up is being bypassed [77, 153].

2.2.2.4 Wake induced transition

Basic mechanisms

According to *Halstead et al.* [34, 35, 36, 37], wake-induced transition on turbomachine blades may occur in one of three ways:

1. **Wake-induced transition in attached flow:**
   If the Reynolds number is high enough so that transition is complete before laminar separation can occur, or if the boundary layer does not separate because the levels of suction-surface deceleration are slight, then attached flow transition is induced by the high turbulence in the wakes. Between the wakes, the flow also remains attached. Further downstream, the background disturbances may also promote transition between the wake-induced events as these propagate downstream. [42]

2. **Wake-induced transition in the separated flow:**
   At increased suction-surface deceleration and lower Reynolds numbers the laminar boundary layer tends to separate and transition is induced

by the wakes inside the separated shear layer. The wake thus acts as an accelerator for the transition process in this case.

3. **Wake-induced transition in attached flows in the presence of laminar separation bubbles:**
   In this case, the transition is induced within the attached boundary layer upstream of the LSB. The separation of the flow is thus either suppressed periodically (low wake frequency) or completely (high wake frequency), depending on the frequency of the wake passing. In the periodic case, flow separation occurs between the wake events and the transition takes place via the mechanism of separated shear layer transition described before.

Since only the latter mechanism is relevant for the perturbed cases considered in this paper, it will be explained in more detail below. For details on the other cases, please refer to the work of *Hodson and Howell* [42] and *Halstead et al.* [34, 35, 36, 37].

The effect of wake-induced transition in attached flow on separation bubbles

As the lift coefficient of an LPT blade is increased or the Reynolds number is reduced, the likelihood of laminar separation increases. In the former case, this is because the increase in pitch-chord ratio leads to a higher velocity peak on the suction surface. In the latter case, it is because the Reynolds number of the boundary layer is reduced while the point of separation essentially remains fixed [42].

If this flow is now perturbed by periodic incoming wakes, the transition of the laminar boundary layer upstream of the LSB takes place mainly via the mechanism of the bypass transition, which has already been described before. This can be ascribed to the fact that, according to *Halstead et al.* [36], the turbulence intensity inside the incoming wake can easily exceed 5%, which, similar to a strongly increased FSTI, causes the direct formation of turbulent spots within the laminar boundary layer, whose structure is shown schematically in Fig. 2.11 (top).

It can be seen that the shape of turbulent spots is approximately triangular and that they spread at an angle of about 22° as they move downstream of their origin. The dark shaded region swept out by the turbulent spot is its zone of influence. Regarding to *Schubauer and Skramstad* [117], which performed experimental investigations on a flat plate at zero pressure gradient, the velocities of the leading and trailing boundaries are constant at $0.88U_\infty$ and $0.5U_\infty$ respectively, which is why the spot maintains a self similar shape as it gets convected downstream. They further found, that a so

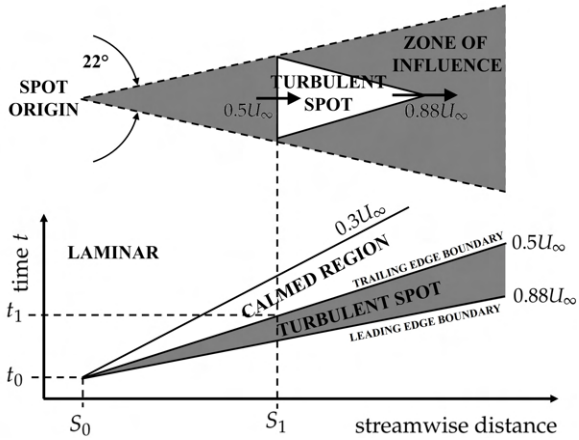

Figure 2.11: Plan view of a turbulent spot after *Schubauer and Skramstad* [117], and *S-t*-diagram of turbulent spot after *Halstead et al.* [34]

called "calmed region" forms immediately behind a turbulent spot or turbulent strip, which they identified as the region of decreasing, but still elevated, wall shear stress behind a turbulent spot or strip. Inside the calmed region the formation of new instability mechanisms like TS-waves or bypass transition processes is suppressed as the flow recovers from the direct wake impact, which further reduces the susceptibility of the flow to separate from the blade surface as reportet by *Halstead et al.* [36].

Based on these informations a time-space evolution of a single turbulent spot can be derived, which is shown at the bottom of Fig 2.11 and can be considered as the basis for the distance-time relationships of the wake-induced transition, which will be explained in more detail below.

Figure 2.12 shows the development of the boundary layer under periodic wake influence by means of a schematic time-space representation. It is important to note that this is a general representation, which of course depends strongly on the operating conditions, such as Reynolds number, rotational speed, FSTI and the aerodynamic loading of the blade profile. The influence of these parameters can strongly change the course of the schematic state regions, which will be discussed in more detail in the following.

First of all, the global course can be divided into two regions, namely the wake-induced path (1) and the path between wakes (2):

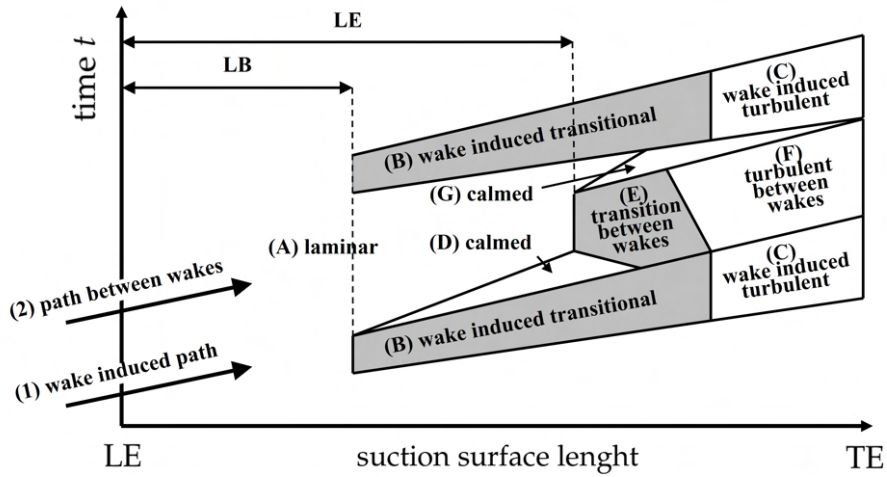

Figure 2.12: Time-space evolution of boundary layer development under periodic wake impact after *Halstead et al.* [34]

1. **Wake-induced path**
   While the wakes of the upstream blades are convected along the blade surface, the resulting turbulent fluctuations penetrate into the laminar boundary layer. From a certain point downstream of the leading edge (L_B) this induces turbulent spots within the boundary layer, whose leading and trailing edges spread along the blade surface according to the propagation velocities shown in Fig. 2.11, thus forming the trajectories of the so-called wake induced path (region (B)) shown in Fig. 2.12.

   When transition is completed within region B and the boundary layer becomes turbulent, this strip continues to the trailing edge as a wake induced turbulent strip (region (C)).

   Depending on the Reynolds number, wake intensity and blade loading, the ratio between the two regions (B) and (C) can vary. It can also happen that region (B) extends to the trailing edge of the blade when the Reynolds number is reduced and thus the wakes are no longer able to cause the laminar boundary layer to transition to the turbulent state.

2. **Path between wakes**
   In between the wakes the boundary layer development is strongly affected by the FSTI, the pressure gradient and of course the calmed region (D), which forms behind the turbulent spots generated inside the wake induced transitional regions (B).

Depending on the intensity of the turbulent spots within region (B), a more or less pronounced calmed region (D) is formed, which prevents or delays the transition or detachment of the boundary layer (region (E)) due to an increased wall shear stress. If the frequency of the incoming wakes is too low or the efficiency of the calmed region is reduced due to low intermittency within the transitional regions (B), a transition of the boundary layer occurs within the region (E) (which is in turn followed in time by a calmed region (G)). This can take place via a detached shear layer or in the attached state (mostly via the mechanism of the bypass transition).

Similar to the wake induced path depending on the operating conditions of the turbine, the transition process can be completed and a turbulent region (F) forms up to the trailing edge of the blade, or the flow remains transitional or detached.

In the case of an increased wake frequency, regions (E) and (F) may even be eliminated completely. In this case, the flow is able to resist the transition or detachment due to a strongly pronounced calmed region, so that a laminar flow is maintained between the wake impacts, enabling operation at low flow losses.

2.3 Mathematical model

This chapter summarizes the mathematical model on which the underlying studies are based. At the beginning the Navier-Stokes equations, which govern the flow of constant-property Newtonian fluids are discussed, as well as the basic assumptions which are necessary for this description. It should be mentioned at this point that the underlying test case is to be regarded as incompressible and isothermal, therefore only the special incompressible variant of the relevant equations is dealt with in the following. Furthermore, the basic properties of turbulent flows are addressed together with a description of three of the main modeling approaches.

2.3.1 Continuum hypothesis

Each fluid consists of individual molecules. Depending on the type of fluid (liquid or gaseous) and its state, these molecules are more or less far apart. According to *Pope* [95], the average distance between two molecules for air under ambient conditions is 3×10^{-9} m, the average free path λ is 6×10^{-8} m and the mean time between successive collision of a molecule is 10^{-10} s.

In comparison, the smallest length of a flow is rarely less than 0.1 mm $=$ 10^{-4} m, which results in time scales of around 1 µs $=$ 10^{-6} s up to flow speeds of 100 m/s. Thus, even for this example of a flow with small length and time scales, these flow scales exceed the molecular scales by three or more orders of magnitude.

It is obvious that a mathematical description of the movements of each individual molecule is simply impossible at this point in time. In addition, however, it is not feasible due to Heisenberg's uncertainty relation, according to which the location and momentum of a molecule cannot be given simultaneously [132]. Therefore, it is more useful to combine many molecules within a very small partial volume (ideally infinitesimally small) of the considered area and to consider the respective quantities like density, velocity etc. within this area as a continuous function of space and time. The whole area to be considered ideally consists of infinitely many of these sub-areas and thus forms a continuum, whose motion can be described by partial differential equations. Therefore, this hypothesis is the essential basis for the following mathematical description of the movement of fluid flows.

2.3.2 Navier-Stokes equations

The governing fundamental equations of viscous fluid flows are called Navier-Stokes (N-S) equations, named after French engineer and physicist Claude-Louis Navier and Anglo-Irish physicist and mathematician George Gabriel Stokes.

The N-S equations consist of the conservation equations for mass, momentum and energy, which fully describe the motion of the fluid. Since the flow in the underlying case can be considered incompressible and isothermal, the energy equation can be neglected and the conservation of mass simplifies to the divergence-free nature of the velocity field. [105]

The differential variant of the incompressible N-S equations, omitting volume forces and written in Cartesian coordinates is given by:

$$\frac{\partial u_i}{\partial x_i} = 0 \tag{2.12}$$

$$\frac{\partial u_i}{\partial t} + \frac{\partial u_i u_j}{\partial x_j} = \frac{1}{\rho}\left(-\frac{\partial p}{\partial x_i} + \frac{\partial \tau_{ij}}{\partial x_j}\right). \tag{2.13}$$

Since in this case a Newtonian fluid is involved, according to the Stokes' hypothesis the viscous stress tensor τ_{ij} yields:

$$\tau_{ij} = 2\mu S_{ij} - \left(\frac{2\mu}{3}\right)\frac{\partial u_k}{\partial u_k}\delta_{ij}, \tag{2.14}$$

with the molecular viscosity of the fluid μ and the strain-rate tenosr S_{ij}. This equation is based on the linear relation between the internal body forces and the rate of strain of the velocity field.

As the second term corresponds to the divergence of the velocity field, it disppears due to Eq. (2.12) so that the components of the viscous stress tensor are given by:

$$\tau_{ij} = 2\mu S_{ij} = \mu\left(\frac{\partial u_i}{\partial x_j} + \frac{\partial u_j}{\partial x_i}\right). \tag{2.15}$$

The N-S equations are usually accompanied by an equation of state relating pressure, temperature and density. This equation describes the variation of state of the fluid during the flow process and in case of the assumption of an ideal gas reads:

$$p = \rho R T, \tag{2.16}$$

with the ideal gas constant R, which in the case of dry air is approximately $R = 287\,\mathrm{J/(kg\,K)}$.

2.3.3 Turbulence

2.3.3.1 Turbulent energy cascade

The idea of the turbulent energy cascade is based on the work of *Richardson* [98] and basically states that turbulence is composed of eddies of different lengths and time scales, between which energy is exchanged. The total turbulent kinetic energy k distributed among these different eddies involved can be calculated based on the velocity fluctuation components [146]:

$$k(x_i) = \frac{1}{2}\overline{u_k' u_k'}. \tag{2.17}$$

The largest energy-bearing structures are generated by a conversion of kinetic energy from the main flow into vortices due to velocity gradients. The length scale of these vortex structures l_0 is usually comparable to the flow scale $\mathcal{L}$, while their characteristic velocity $u_0 = u(l_0)$ is comparable to the

characteristic velocity scale of the flow $\mathcal{U}$. Since the Reynolds number of these vortices $\mathrm{Re}_0 = u_0 l_0/\nu$ is relatively high, viscosity effects play a minor role.

According to *Richardson* these structures are unstable and break up, forming at least two more vortices between which the energy is divided. This process continues until the Reynolds number of vortices $\mathrm{Re}(l) = u(l)l/\nu$ formed is so small that the vortex motion stabilizes and the kinetic energy is dissipated into thermal energy.

A frequently quoted sentence from Richardson's work describes this process in picturesque fashion:

> *Big whorls have little whorls,*
> *Which feed on their velocity;*
> *And little whorls have lesser whorls,*
> *And so on to viscosity*
> *(in the molecular sense).*

2.3.3.2 Scales of turbulent motion

The model of the turbulent energy cascade described above provides information about the basic energetic relationships within turbulent flows, but doesn't provide information about the actual length scale l, time scale τ or velocity scale u of the structures during turbulent decay.

A significant extension of this model was published by *Kolmogorov* [53] in 1941, which allowed a clear subdivision of the turbulent energy spectrum as well as a clear relation between the respective scales.

In order to summarize the essential aspects of this theory, the areas of the turbulent energy spectrum described below are shown graphically in Fig. 2.13.

It should be noted at this point that the relationships described below apply to flows with high to very high Reynolds numbers. The subdivision of the different areas is usually based on the wave number $\kappa = 2\pi/l$, which is inverse to the length scale l, so the large scales can be found on the left side of the figure, while the small scales are on the right.

According to Kolmogorov, the turbulent energy spectrum can initially be divided into two ranges, namely the energy containing range and the universal equilibrium range (demarcation line: $l = l_{\mathrm{EI}} \approx 1/6 \cdot l_0$ [95]).

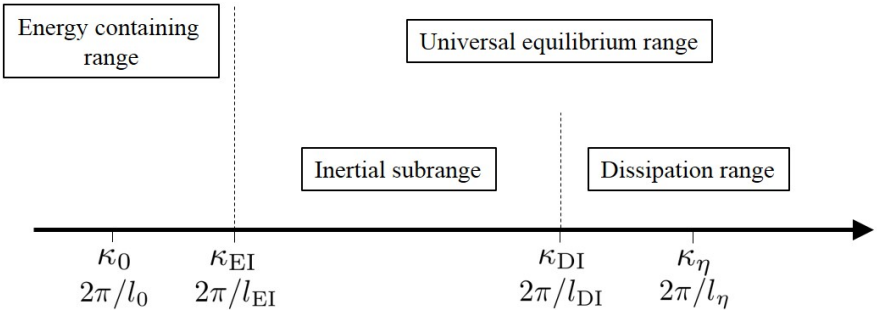

Figure 2.13: Wavenumbers (on a logarithmic scale) at very high Reynolds number showing the various ranges. Own representation according to *Pope* [95].

The first contains the large coherent structures ($l \approx \mathcal{O}(\mathcal{L})$), which are fed by the kinetic energy of the mean flow and are therefore highly anisotropic by nature and are affected by the boundary conditions of the flow.

The latter contains the smaller, mostly isotropic eddies $l < l_{EI}$, whose time scales $l/u(l)$ are small compared to l_0/u_0, so that the small eddies can adapt quickly to maintain a dynamic equilibrium with the energy-transfer rate imposed by the large eddies. The turbulent statistics of these small-scale structures have a universal character, which is similar in any flow at high Reynolds numbers and is only affected by the fluid's kinematic viscosity ν and the flows dissipation rate ε .

According to Kolmogorov, the universal equilibrium range can be further divided into the inertial subrange and the dissipation range. For this purpose, the length scale l_{DI} is introduced as a demarcation line, with $l_{DI} \approx 60\eta$ [95], where η is the smallest spatial scale that can be formed within a turbulent flow (Kolmogorov length scale).

Within the inertial subrange $l_{EI} < l < l_{DI}$, the eddies and their Reynolds number are large enough that viscous effects play a negligible role. Thus, the statistics of turbulent motion are solely determined by the dissipation rate ε. The dissipation of the turbulent energy thus takes place exclusively on scales within the disspation range, where the Reynolds number is small enough that the viscous effects become dominant.

The ratio between the smallest energy-dissipating scales the large energy-containing structures was found by Kolmogorov to be dependent on the turbulence Reynolds number Re_L of the flow:

$$\eta/l_0 \sim \mathrm{Re}_L^{-3/4}, \qquad u_\eta/u_0 \sim \mathrm{Re}_L^{-1/4}, \qquad \tau_\eta/\tau_0 \sim \mathrm{Re}_L^{-1/2}. \tag{2.18}$$

He could thus show that also the time scales and velocity scales of the smallest structures are small compared to the largest structures and that they get even smaller with increasing Reynolds number.

2.3.3.3 Turbulence modeling

Although laminar flow plays an important role in many applications as in the underlying test case, most flows in technically relevant applications are turbulent (at least at some portions of the respective domains). In summary it can be stated that turbulent flows are:

- highly unsteady,
- non-deterministic,
- 3-dimensional,
- consisting of a wide range of temporal and spatial scales.

It is therefore obvious that an adequate representation of the effects caused by turbulence through the applied CFD methods is of essential importance. Adequate in this context means that the user must first be aware of how strongly the underlying flow case is influenced by the effects of turbulence. In the end, this determines which numerical approach is used and thus the level of detail at which the turbulence is represented, resulting in a considerable difference in the overall computational costs.

The following sections contain a fundamental description of the three principal methods of turbulence treatment. They differ mainly in the degree of the modeled part of the turbulence, so at this point the turbulent energy spectrum should be mentioned again, which has already been discussed in detail in chapter 2.3.3.2.

Figure 2.14 shows the distribution of the spectral energy content along the different wave numbers κ of a turbulent flow. It can be seen, that the DNS approach resolves the whole energy spectrum, while the LES and the URANS approaches model certain portions of the energy spectrum. The basic functioning of the different approaches is discussed in the following.

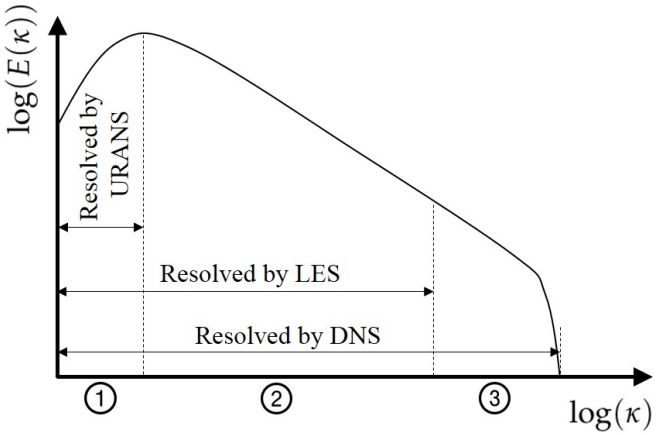

Figure 2.14: Schematic drawing of the spectral energy distribution in turbulent flows.

2.3.3.4 Reynolds-averaged Navier-Stokes simulation (RANS)

The RANS approach is the most inexpensive of the three methods, which is why it is also the most widely used for industrial applications. The key of this approach is the Reynolds decomposition of the respective flow values into a mean and a fluctuating part:

$$\phi(\mathbf{x}, t) = \bar{\phi}(\boldsymbol{x}) + \phi'(\boldsymbol{x}, t). \tag{2.19}$$

The governing equations are then solved only for the temporal mean of the respective flow variables.

In contrast to the two approaches explained above, which are intrinsically transient by nature, a distinction must be made between stationary and transient formulation in RANS. In case of steady RANS (assuming a statistically stationary flow) the mean value of any flow quantity ϕ is determined by:

$$\bar{\phi}(\boldsymbol{x}) = \lim_{T\to\infty} \frac{1}{T} \int_0^T \phi(\boldsymbol{x}, t)\mathrm{t}, \tag{2.20}$$

where t is the time and T is the averaging interval, which must be large compared to the typical time scale of the fluctuations. In the RANS case, the whole turbulent spectrum (Fig. 2.14 regions 1 + 2 + 3) must be modeled completely.

In case of unsteady RANS (URANS) a triple decomposition (see *Hussain and Reynolds* [47]) of the flow field has to be performed:

$$\phi(\boldsymbol{x},t) = \bar{\phi}(\boldsymbol{x}) + \tilde{\phi}(\boldsymbol{x},t) + \phi'(\boldsymbol{x},t), \tag{2.21}$$

where the additional statistical part $\tilde{\phi}(\boldsymbol{x},t)$ represents the large scale coherent motions of the flow and $\phi'(\boldsymbol{x},t)$ stands for the fluctuations related to turbulent motion.

The data set is then divided into subsets, in each of which ensemble averaging (or bin averaging) of the respective flow variable is performed, according to:

$$\{\phi\}(\boldsymbol{x},t) = \lim_{N\to\infty} \frac{1}{N} \sum_{n=1}^{N} \phi(\boldsymbol{x},t), \tag{2.22}$$

where N is the number of members of the ensemble and must be large enough to eliminate the effects of the turbulent (random) fluctuations [26].

If the time window associated with each ensemble is adequately selected, the URANS approach is able to represent the large-scale flow motions by this type of averaging procedure (Fig. 2.14 region 1), so that transient effects such as vortex shedding, which form e.g. in the flow past a cylinder can be resolved.

Similar to the filtered N-S equations in the LES approach (see Eq. (2.28) and (2.29)), the (U)RANS equations have an additional term τ_{ij}^R, which results from the nonlinearity in the convection terms of the momentum equations:

$$\frac{\partial\{u_i\}}{\partial x_i} = 0 \tag{2.23}$$

$$\frac{\partial\{u_i\}}{\partial t} + \frac{\partial\{u_i\}\{u_j\}}{\partial x_j} = \frac{1}{\rho}\left[-\frac{\partial\{p\}}{\partial x_i} + \frac{\partial}{\partial x_j}\left(\{\tau_{ij}\} - \tau_{ij}^R\right)\right], \tag{2.24}$$

with $\{\tau_{ij}\}$ representing the ensemble averaged variant of the stress tensor (Eq. (2.14)) and the (symmetric) Reynolds stress tensor

$$\tau_{ij}^R = \rho\{u_i u_j\} - \rho\{u_i\}\{u_j\} = \rho\{u_i' u_j'\} = \rho \begin{bmatrix} \{(u_1')^2\} & \{u_1'u_2'\} & \{u_1'u_3'\} \\ \{u_1'u_2'\} & \{(u_2')^2\} & \{u_2'u_3'\} \\ \{u_1'u_3'\} & \{u_2'u_3'\} & \{(u_3')^2\} \end{bmatrix}, \tag{2.25}$$

which represents the transfer of momentum due to turbulent fluctuations.

As this term introduces six new unknown variables to the set of governing equations it has somehow to be modeled. This is performed by the application of turbulence models, which are much more sophisticated and complex

than the SGS models used in LES, as they must represent the entire turbulent spectrum, including the highly anisotropic range at small wave numbers (cf. Fig. 2.14).

In all (U)RANS simulations performed within this work, the shear stress transport (SST) model by *Menter* [79] was used. Which involves two additional transport equations for the turbulent kinetic energy k and the specific dissipation rate ω.

2.3.3.5 Large-eddy simulation (LES)

In order to reduce the considerable computing effort of DNS, various methods have been developed, which are based on modeling a certain part of the turbulent spectrum.

One method is the LES, which belongs to the same category as DNS, since it directly calculates the turbulent fluctuations in time and space, but only up to a certain length scale ("large eddies", Fig. 2.14 regions 1 + 2). Below this length scale, which is also called subgrid scale (Fig. 2.14 region 3), turbulence is modeled using semi-empirical laws [39].

This approach is reasonable, because as already mentioned in section 2.3.3, it is the large vortex structures that transport the bulk of the energy and are therefore mainly responsible for the transport of the respective conservation quantities, while the smaller ones are usually much weaker and provide little transport of these properties [26]. Another important aspect is that the smaller structures can be considered to be mainly isotropic and homogeneous (not in the close vicinity of solid walls) by the assumption of local isotropy according to *Kolmogorov* [53] (cf. section 2.3.3.2), which simplifies their modeling considerably.

As a consequence even for wall resolved LES, where according to *Choi and Moin* [16] the near wall resolution inside the viscous sublayer has to be increased like $N \sim \mathrm{Re}^{13/7} \approx \mathrm{Re}^{1.86}$, the computational cost decreases, compared to DNS ($N \sim \mathrm{Re}^{37/14} \approx \mathrm{Re}^{2.64}$), in such a way that LES can be applied at Reynolds numbers at least one order of magnitude higher [12], which is the reason why it was used for all simulations underlying to this work.

Filtered governing equations

Because scale separation can be assumed, a spatial filtering of all flow variables can be employed in order to distinguish between the different scales of

the turbulent energy spectrum described above. The decomposition of any variable ϕ by means of a spatial filtering is given by:

$$\phi(\boldsymbol{x},t) = \underbrace{\hat{\phi}(\boldsymbol{x},t)}_{\text{grid-scale}} + \underbrace{\dot{\phi}(\boldsymbol{x},t)}_{\text{subgrid-scal}} \quad . \tag{2.26}$$

where, according to *Sagaut and Meneveau* [105], the filtered quantity $\hat{\phi}$ is described by a convolution product in the physical space:

$$\hat{\phi}(\boldsymbol{x},t) = \int_{-\infty}^{+\infty}\int_{-\infty}^{+\infty} G(\boldsymbol{x}-\boldsymbol{x}',t-t')\phi(\boldsymbol{x}',t')\,\mathrm{d}t'\mathrm{d}\boldsymbol{x}'. \tag{2.27}$$

The filter kernel G can be specified explicitly, but in case of an implicit LES as it was used in the present work, it is intrinsically given by the numerical discretization whilst the filter width is given by the local mesh size. [27, 105].

The filtered variant of the incompressible N-S equations reads:

$$\frac{\partial \hat{u}_i}{\partial x_i} = 0 \tag{2.28}$$

$$\frac{\partial \hat{u}_i}{\partial t} + \frac{\partial \hat{u}_i\hat{u}_j}{\partial x_j} = \frac{1}{\rho}\left[-\frac{\partial \hat{p}}{\partial x_i} + \frac{\partial}{\partial x_j}\left(\hat{\tau}_{ij} - \tau_{ij}^S\right)\right], \tag{2.29}$$

with $\hat{\tau}_{ij}$ representing the filtered variant of the stress tensor (Eq. (2.14)). The non-linearity of the convective term leads to the appearance of the so-called subgrid-scale stress (SGS) tensor:

$$\tau_{ij}^S = \rho\widehat{u_iu_j} - \rho\hat{u}_i\hat{u}_j, \tag{2.30}$$

which in fact describes the large scale momentum flux caused by the action of the small or unresolved scales [12, 26] and similarly as in the (U)RANS approach has to be modeled, which is further explained in the numerical fundamentals in section 2.4.3.

2.3.3.6 Direct numerical simulation (DNS)

DNS is the simplest of the three methods, although it is the most expensive. As shown in Fig. 2.14, the DNS resolves the entire turbulent spectrum down to the smallest structures about the size of the Kolmogorov length scale. For

this reason, there are no further modeling errors except for the approximation errors of the involved numerical schemes (if additional models, such as condensation or similar, are excluded). The error inherent in this method is therefore directly quantifiable and controllable and is independent of the particular test case.

As explained in section 2.3.3.2, the size of the smallest spatial and temporal scales behaves inversely proportional to the Reynolds number. It is therefore obvious that the computational effort also increases with the Reynolds number (cf. Eq. (2.18)).

Thus, if one wants to resolve the smallest spatial structures in all three directions of space with n points, the total number of grid points as well as the arithmetic operations is scaled according to Equation 2.18 with $n^3 \cdot \mathrm{Re}^{3/4}$ [39]. Since the numerical time step is directly determined by the smallest spatial scales, the computational cost for DNS simulations scales with Re^3.

This means that increasing the Reynolds number by a factor 10, requires an increase in the computational cost of at least a factor 1000, which means that the DNS will remain impracticable for a long time for most application-relevant considerations within the field of turbomachinery, where the Reynolds numbers mainly range between 10^4 and 10^6.

2.4 Numerical fundamentals

The following chapter contains the most important basics of numerical flow simulation. First, the used flow solver ANSYS Fluent is presented in its basic features. Afterwards the applied method, namely the finite volume method (FVM), is explained. The used discretization schemes are discussed on the basis of the individual terms and their essential structure is briefly described. Finally, the used solution method is explained, with special emphasis on the pressure-velocity coupling.

It should be noted that this is a commercial flow solver, which is extensively documented in the literature. For this reason and because the flow solver was not significantly modified, only a superficial description of the relevant schemes and settings is presented in this chapter.

2.4.1 Numerical method

All scale-resolving simulations presented in this work were performed using the commercial flow solver ANSYS FLUENT in its version R2020 R2.

The solver is a cell centered implementation of the finite volume method (FVM) for the discretization of the N-S equations. It uses an unstructured discretization approach, which guarantees a high degree of flexibility with respect to the used computational grids (more details are given in the following sections). Both a pressure-based solver and a density-based solver can be used, making ANSYS FLUENT suitable for both low (as in this work) and high to very high Mach numbers.

For the final solution of the system of equations, either a coupled method or a segregated method can be used.

2.4.2 Finite approximations

2.4.2.1 The finite volume method

The application of the finite volume method (FVM) in the field of CFD goes back to *McDonald* [78] (1971) and *Maccormack and Paullay* [68] (1972), which introduced it independently of each other for the solution of 2-dimensional, transient Euler equations.

The FVM is a direct discretization of the integral form of the conservation equations,which does not require the fluxes to be continuous (property which is not satisfied for instance along shock waves or along free surfaces) [39].

In contrast to the finite difference method where the differential form of the conservation equations is discretised and the domain of interest is divided into discrete points, in the FVM it is divided into small control volumes which are connected by shared boundary surfaces. In each of these control volumes, the temporal change of the respective conservation quantity is considered to be the balance of convective and diffusive fluxes over the boundary surfaces of the volume and the distribution of all sources and sinks within the volume.

In principle, these elements can take any shape, which makes this method very flexible. Typically used element types are shown in Fig. 2.15, where the polyhedral element type (d) is relatively new in ANSYS FLUENT and offers a very efficient possibility for hybrid mesh generation (structured/unstructured).

Since the geometry in this work is relatively simple, only hexahedral elements were used for mesh generation. It is therefore a structured mesh, which does not offer any advantages when used in an unstructured solver

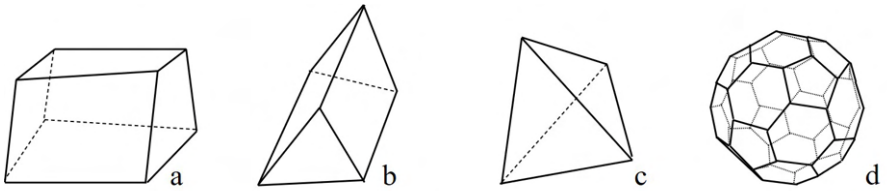

Figure 2.15: Schematic drawing of commonly used control volume shapes in ANSYS FLUENT: a) hexahedron, b) prism, c) pyramid, d) polyhedron.

first of all. However, a high-quality hexahedral mesh is in most cases preferable to an unstructured mesh, because a considerably higher mesh quality can be realized.

A closer look at the generic transport equation reveals that the fluxes are calculated on the boundary surfaces of the control volumes, while the temporal variation and the source terms are evaluated inside the control volume. Furthermore, the terms differ in whether the flow quantity or its gradient is to be evaluated.

Depending on the formulation of the solver, cell-centered or vertex based, the respective values are available directly or have to be approximated from neighboring cells. A brief overview of the selected procedures within ANSYS FLUENT is given in the following section.

2.4.2.2 Individual term treatment

ANSYS FLUENT offers a variety of settings regarding the treatment of the terms of the respective conservation equations. These allow the user to adapt the solver to the given flow situation, so that a robust solution can be achieved. The settings made for the simulations of this work are briefly explained in the following as well as their theoretical basis. For a more detailed description refer to the literature sources provided.

Temporal variation

For the temporal discretization of the conservation equations only an implicit discretization is available when using the pressure based solution method. In principle, first and second order discretization can be chosen.

For the temporal development of a scalar quantity $\frac{\partial \phi}{\partial t} = F(\phi)$ the second order method employed in this work has the following structure:

$$\frac{3\phi^{n+1} - 4\phi^n + \phi^{n-1}}{2\Delta t} = F(\phi^{n+1}), \tag{2.31}$$

where n denotes the current time level, while $n-1$ stands for the previous time level at $t - \Delta t$ and $n+1$ for the next time level at $t + \Delta t$. This procedure generally results in a truncation error of $\mathcal{O}\left[(\Delta t)^2\right]$, which, however, is additionally influenced by the manner in which the solutions are advanced to the next time step (cf. section 2.4.5).

Convective fluxes

The face values of the respective flow quantity are required for the evaluation of the convective fluxes. Since ANSYS Fluent stores these values in the cell centers, it is therefore necessary to interpolate them based on the neighboring cells. This is typically realized using upwind methods, where the value on the cell face is interpolated based on the upstream cell center. However, the drawback of these methods is a high numerical diffusion, which leads to small-scale turbulent structures being damped away from the discretization procedure and thus distorting the solution when applied in the field of scale-resolving methods such as LES.

An alternative is given by the central difference scheme (CDS), which is second order accurate and has meritoriously low numerical diffusion. It is therefore an optimal choice for scale-resolving simulations using the FVM. The CDS calculates the face value for a variable ϕ_f as follows:

$$\phi_{f,\mathrm{CD}} = \frac{1}{2}\left(\phi_0 + \phi_1\right) + \frac{1}{2}\left(\nabla\phi_0 \cdot \boldsymbol{r}_0 + \nabla\phi_1 \cdot \boldsymbol{r}_1\right), \tag{2.32}$$

where the indices 0 and 1 refer to the cells that share face f, $\nabla\phi_{r,0}$ and $\nabla\phi_{r,1}$ are the reconstructed gradients at cells 0 and 1 (cf. section 2.4.2.2), respectively, and $\boldsymbol{r}$ is the vector directed from the cell centroid toward the face centroid.

A drawback of such methods, however, is that they can produce non-physical wiggles accompanied by non-physical overshoots or undershoots, especially in regions with steep gradients of transported variables, which in turn can lead to stability problems.

This problem is avoided by the so-called Bounded CDS (BCDS), which was therefore used in this work. The BCDS is a so called normalized variable diagram (NVD) method [62] that blends central differences, second order

upwind and first order upwind in order to satisfy the convection boundedness criterion (CBC) criterion. For more details refer to the work of *Gaskell and Lau* [28] and *Choi et al.* [17].

Diffusive fluxes

For the diffusive fluxes the gradients of the respective flow quantity on the boundary surfaces $\mathcal{S}$ of the control volume are required. In order to calculate these gradients, first the gradients at the cell centers are computed, which are also needed for the reconstruction of scalar values at the cell faces (cf. Eq. (2.32)) and velocity derivatives.

This is done using one of the three available methods: Green-Gauss Cell Based (GGCB), Green-Gauss Node Based (GGNB) and Least-Squares Cell Based (LSCB). The GGNB achieves a higher accuracy than the GGCB method, especially in case of distorted grids, but is more expensive to compute. For the simulations carried out in this thesis, the LSCB method was used, since it achieves a comparable accuracy to the GGNB method, but is much more efficient in terms of computational costs [5].

The required gradients at the cell faces are determined by the application of a multi-dimensional Taylor series expansion.

Source terms

The treatment of the source term requires the integration over the control volume $\mathcal{V}$. Since the values are already available for a cell-centered procedure, no reconstruction is necessary in this case. The volume integral of Φ can thus be replaced by the product of the mean value of $\overline{\Phi}$ and the volume of the control volume, where the former is approximated as the value at the center of the control volume:

$$\Phi_p = \int_{\mathcal{V}} \phi \, \mathrm{d}\mathcal{V} = \overline{\phi} \, \Delta\mathcal{V} \approx \phi_P \Delta\mathcal{V}. \tag{2.33}$$

According to *Ferziger and Perić* [26], the above approximation becomes exact if q is either constant or varies linearly within the control volume; otherwise, it contains a second-order error.

2.4.3 Subgrid-scale modeling

Subgrid-scale (SGS) modeling refers to the representation of important small-scale physical processes that occur at length-scales that cannot be adequately resolved on the underlying computational mesh. In Large-Eddy Simulation of turbulence, SGS modeling is used to represent the effects of unresolved small-scale fluid motions in the equations governing the large-scale motions that are resolved by the mesh.

There are two basic categories of SGS modeling approaches, explicit and implicit. The former model the SGS tensor τ_{ij}^S explicitly, mostly based on the local velocity field. In this context, it is crucial that the numerical damping of the applied numerical discretization schemes is significantly lower than that of the SGS model.

The latter follows the assumption that the SGS viscosity is adequately represented by the numerical damping of the applied method, so that the SGS stress term is completely omitted in the discretized equations. Since an explicit SGS-viscosity treatment is used in this thesis, only this approach will be discussed in the following. Further details on the implicit approach, (often referred to as monotonically integrated LES (MILES)), are given by *Sagaut and Meneveau* [105] and *Garnier et al.* [27].

The model used in this work is the so-called wall-adapting local eddy-viscosity (WALE) model, developed by *Nicoud and Ducros* [84]. As in transitional flows, the SGS model must not corrupt the laminar portion of the flow by introducing spurious dissipation, the WALE model is built to recover the expected asymptotic behavior of the SGS viscosity in the near-wall region in equilibrium turbulent boundary layers on fine grids, without any additional damping function [105]. Therefore, it is well suited to accurately capture the laminar to turbulent transition inside boundary layers.

Like the well-known Smagorinski model, the WALE model belongs to the algebraic eddy viscosity models, which are essentially based on the equilibrium hypothesis which implies that the small scales dissipate entirely and instantaneously all the energy they receive from the large scales [12, 105]. According to the Boussinesq hypothesis [13], these models relate the deviatoric part of the SGS stresses to the filtered large-scale strain rate $\hat{S}_{ij}$:

$$\underbrace{\tau_{ij}^{\mathrm{sgs}} - \frac{\delta_{ij}}{3}\tau_{kk}^{\mathrm{sgs}}}_{\substack{\text{deviatoric} \\ \text{part of } \tau^{\mathbf{sgs}}}} = -2\nu_{\mathrm{sgs}}\hat{S}_{ij}, \tag{2.34}$$

with

$$\hat{S}_{ij} = \frac{1}{2}\left(\frac{\partial \hat{u}_i}{\partial x_j} + \frac{\partial \hat{u}_j}{\partial x_j}\right). \tag{2.35}$$

In the WALE model the turbulent viscosity ν_t is calculated using a combination of resolved velocity spatial derivatives:

$$\nu_{sgs} = (C_w \hat{\Delta})^2 \frac{(S^d_{ij} S^d_{ij})^{3/2}}{(\hat{S}_{ij}\hat{S}_{ij})^{5/2} + (S^d_{ij} S^d_{ij})^{5/4}}, \tag{2.36}$$

with the WALE constant C_w, which was set to the default value in ANSYS FLUENT, $C_w = 0.325$ for all calculations of the underlying work.

In Eq. (2.34) the complementary spherical tensor $\frac{1}{3}\tau^{sgs}_{kk} = \frac{2}{3}k^{sgs}$, with the kinetic energy of the subgrid modes k^{sgs}, is added to the filtered static pressure term and consequently requires no modeling. This decomposition is necessary since the tensor $\hat{S}_{ij}$ has a zero trace, and thus the modeled tensor must also have a zero trace [105].

2.4.4 Pressure-velocity coupling

As already described in section 2.3.2, the incompressible variant of the N-S equations represents a special case in which the pressure field can not be determined by one distinct equation as it appears in all three momentum equations and there only as a gradient term. To overcome this issue, so-called pressure correction methods are generally used, which are also called predictor corrector methods. ANSYS FLUENT offers four different pressure correction schemes for the segregated solution method: SIMPLE, SIMPLEC, PISO and Fractional Step. As in this work the Fractional Step method (FSM) was used within all unsteady simulations, more informations according this method are given below. For a detailed description of the other methods the reader is asked to refer to the textbooks of *Hirsch* [39, 40] and *Ferziger and Perić* [26].

2.4.4.1 Fractional step method

According to *Ferziger and Perić* [26] the major difference between the FSM and pressure-correction methods of the SIMPLE-type is that in the former the pressure (or pressure correction) is solved only once per time step, while in the latter, both the momentum and the pressure correction equations are

solved several times per time step. This is why the FSM is only available in combination with the non-iterative time advancement scheme (cf. section 2.4.5) in ANSYS FLUENT. For this reason the FSM is mostly used for the computations of unsteady flows, while the SIMPLE-type algorithms are used predominantly for steady flow computation, where accurate satisfaction of the continuity condition is required only at convergence. Thus, the pressure correction equation does not have to be solved exactly at each outer iteration (a reduction of the residual by one order of magnitude is usually sufficient) [26].

There is a variety of FSM methods for the computation of incompressible fluid flows. The method implemented in ANSYS FLUENT forces a decoupling of the momentum equations from the continuity equation using a mathematical technique called operator-splitting or approximate factorization. Within the predictor step the discretized version of equation 2.13 is approximated by calculating a tentative velocity vector $\boldsymbol{u}^*$, using the momentum equations without the pressure, and then use the pressure, found by solving the Poisson equation 2.37

$$\Delta p^{n+1} = \frac{1}{\Delta t} \nabla \cdot \boldsymbol{u}^* \tag{2.37}$$

in order to project the tentative velocity into the space of discretely incompressible functions. By solving Eq. (2.38)

$$\frac{\boldsymbol{u}^{n+1} - \boldsymbol{u}^*}{\Delta t} = -\nabla p^{n+1}. \tag{2.38}$$

the final velocity is found as *Perot* [92] states. A more detailed description of the mathematical background is given in [6, 8, 23, 92].

2.4.4.2 Pressure & velocity interpolation

As ANSYS FLUENT uses a co-located scheme, pressure and velocity are both stored at the cell centroids. In the momentum equation 2.13 the pressure has to be evaluated at the cell faces, therefore, an interpolation scheme is required to compute the face values of the pressure from the cell values. The same is the case for the velocity used in the pressure correction Equation 2.37.

Using a co-located scheme, this can lead to nonphysical oscillations in the pressure field (checker-boarding), which originate from a simple linear reconstruction of cell face pressure and velocity values. To overcome this issue, the default scheme in ANSYS FLUENT interpolates the pressure as well as the velocity values at the faces using momentum equation coefficients,

which is based on a method commonly referred to as *Rhie & Chow* [97] interpolation. A detailed description is given in the textbook *Ferziger and Perić* [26].

2.4.5 Solution method

The segregated solution process, which is used in all unsteady simulations presented in this work, introduces a splitting error additional to the truncation error of the time integration method (cf. section 2.4.2.2), while the fully coupled process does not. However, this method is significantly faster for transient calculations compared to the coupled method, which is why it is particularly useful for scale-resolving simulations in which up to several 100 k time steps must be calculated.

Within the segregated solution process, one can choose between two different approaches, depending on how to deal with the splitting error.

In the iterative time advancement (ITA) method, the respective equations are solved iteratively inside the so-called outer loops within one time step until the splitting error has dropped below the desired convergence criterion. The ITA method is the default scheme in ANSYS FLUENT, but it requires a considerable amount of computational effort due to the large number of outer iterations performed for each time-step.

A much more efficient approach can be pursued with the so-called non-iterative time advancement (NITA) procedure. This is based on the assumption that it is not inevitably necessary to reduce the splitting error with the help of outer iterations. Instead this method performs sub-iterations in order to ensure that the splitting error is in the order of magnitude of the truncation error, so that the more expensive outer iterations are completely omitted.

This method is a possibility to save a lot of computational time especially for weakly compressible to incompressible flows, even if the requirements for the maximum time step size are much more restrictive compared to the iterative methods.

In the simulations on which this work is based, the use of the NITA method saved about 50% of time compared to the ITA scheme, which is why this method was used in all transient simulations.

3 Flow simulation

3.1 Test-case

Within this chapter the experimental setup is described, which is the basis for the numerical investigations presented in this work. In addition to the basic setup and design philosophy, the operating conditions and the realizable turbomachine-specific similarities are explained.

At this point it should be noted that all experimental work was carried out by my colleague Dr.-Ing. Martin Sinkwitz. The following description is only intended to provide a basic overview of the experimental setup, which enables the reader to determine the geometric and turbomachine-specific parameters. A detailed description of the experimental setup is given by *Sinkwitz et al.* [123, 124, 125, 126].

3.1.1 Setup

The underlying test-case is an annular, large scale, axial flow turbine, which is located at the the Chair of Thermal Turbomachines and Aeroengines at Ruhr University of Bochum. It has an outer diameter of 1.66 m (casing) and an inner diameter of 1.32 m (hub). It is operated in an open flow cycle induced by a 150 kilowatts variable-speed engine coupled to a radial blower, which enables a mass flow rate of 12.8 kg/s.

To ensure proper inflow angles to the investigated stator row, the test-facility is equipped with an inlet guide vane (IGV) row made up of 60 vanes (NACA 8408 profile), which is designed and optimized for disturbing the inflow of the investigated stator row as minimal as possible.

In order to produce the artificial wake disturbances, the rotor (driven by a 15 kilowatts AC engine) is equipped with 60 radially stacked steel bars in the investigated configuration. The steel bars are designed to reproduce the velocity defect and turbulence intensity comparable to a realistic turbine's rotor but without the presence of a secondary flow system. The axial distance between the rotating bars and the stator row's leading edge is $x/C_{\text{stator}} = 0.33$, with the stator vane's chord length being $C_{\text{stator}} = 0.1\,\text{m}$, which represents a typical axial gap within an LPT. By changing the rotational speed of the rotor and the number of bars, the test rig allows for separate adjustment of Strouhal number and flow coefficient.

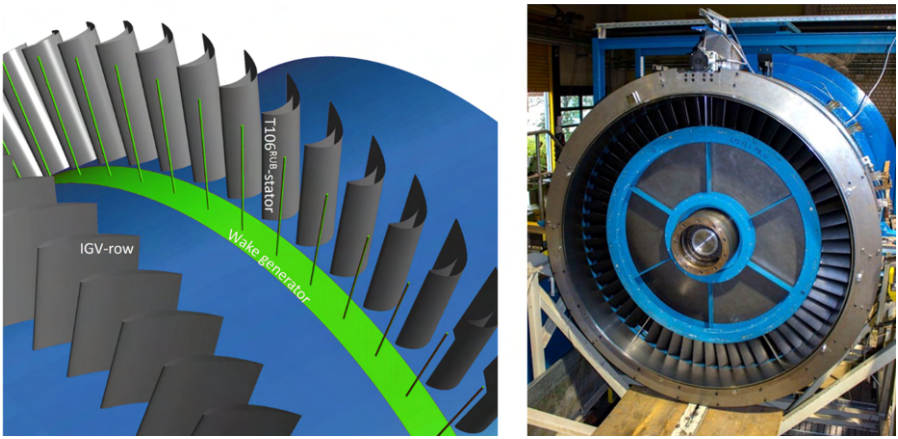

Figure 3.1: 3-dimensional model of the investigated test rig (left), rear view into the investigated $T106^{RUB}$ stator row (right)

The turbine stator row under investigation consists of 60 stator blades (no radial gaps) with a modified T106 profile, specified as $T106^{RUB}$. The profile shape is the result of a CFD based transformation of the original T106 high speed profile and matches its loading characteristics at the prevailing low speed flow conditions.

Main geometric properties are summarized in Tab. 3.1.

3.1.2 Flow conditions & similarity

The operating point investigated within this work is defined at a theoretical exit Reynolds number of $Re_{3,th} = 200,000$ (based on $T106^{RUB}$ chord length C and theoretical exit velocity $c_{exit,th}$):

$$Re_{exit,th} = \frac{c_{exit,th} \cdot \rho_{exit,th} \cdot C}{\mu}. \tag{3.1}$$

The theoretical exit state (using upstream total-pressure and downstream static pressure) is a common way to account for altered losses when the velocity or the count of the rotating bars is modified while maintaining comparability of the flow [123]. The chosen operating point represents a typical value for LPT operation at cruise conditions (cf. Fig. 2.6) where such types of blade profiles are prone to suction side boundary layer separation.

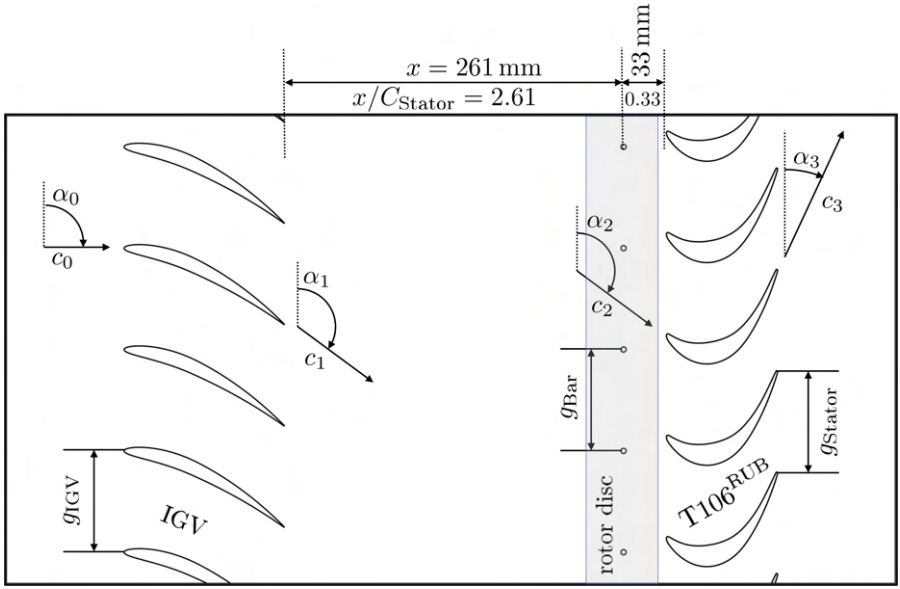

Figure 3.2: Schematic 2-dimensional drawing of the test rig setup at mid-span, including IGV row, rotating wake generator and the investigated $T106^{RUB}$ stator row.

A schematic representation of the components of the test rig at mid-span is illustrated in Fig. 3.2 together with the most important flow parameters.

At the operating point under consideration, the flow upstream the IGV is accelerated to an absolute velocity of $c_0 \approx 12\,\mathrm{m/s}$ (swirl-free inflow, $\alpha_0 = 90\,°$). Within the IGV, the flow is turned to the investigated stator row's design angle of incidence $\alpha_1 = \alpha_2 = 127.7°$ and accelerated to an absolute velocity of approximately $c_1 \approx 17\,\mathrm{m/s}$. Under these inflow conditions the stator row's outflow velocity is $c_3 \approx 32\,\mathrm{m/s}$, which corresponds to a theoretical outflow Mach-number of $\mathrm{Ma}_{3,\mathrm{th.}} = 0.09$. In the experimental investigations, all data required to determine the operating point are measured at several circumferential mid-span positions and averaged.

To characterize the influence of periodic disturbances on the flow conditions within turbomachinery blade rows, two dimensionless quantities are used: the Strouhal number Sr and the flow coefficient ϕ:

$$\mathrm{Sr} = \frac{u_B \cdot C}{g_B \cdot c_{\mathrm{ax}}}, \qquad \phi = \frac{c_{\mathrm{ax}}}{u_B}, \tag{3.2}$$

with the circumferential velocity of the bars u_B and the pitch of the bars g_B, both evaluated at mid-span position.

The Strouhal-number is defined by the frequency of the generated wakes f_B, the chord length of the T106$^{\mathrm{RUB}}$ profile C and the mean axial velocity c_{ax}. It thus represents the ratio of the convection time-scale (l/c_{ax}) to the duration of a periodic event ($1/f_B$) and must be maintained in order to reproduce a representative flow under periodic disturbance [133].

The flow coefficient ϕ is a typical characteristic for the design of turbomachinery stages. It is defined as the ratio of axial speed c_{ax} to rotational speed u (in this case the circumferential speed of the wake generator u_B) and reflects the kinematics of the rotor-stator interaction, since this is primarily determined by the velocity triangles [133].

Within this work, the effect of different perturbed inflow conditions is studied by varying the rotational speed of the vortex generator, while a variation of the bar pitch was not considered for two reasons: On the one hand, an unequal pitch ratio between rotating and stationary domain increases the numerical effort considerably, on the other hand, only for the configuration with 60 bars transient measurement data were available on the blade surface.

In order to better work out the effects of the periodically incoming disturbances on the transition mechanisms, a configuration with unperturbed inflow is also considered as a reference.

Table 3.1: Main geometric test rig properties and turbine stage parameters

Test rig		
Outer diameter (casing)	D_C	1.66 m
Inner diameter (hub)	D_H	1.32 m
Mid-span diameter	D_m	1.49 m
Turbine stage		
Blade height IGV, T106$^{\mathrm{RUB}}$	H	0.17 m
Chord length IGV	C_{IGV}	0.137 m
Pitch IGV at mid-span	g_{IGV}	0.078 m
Stagger angle IGV	λ_{IGV}	25.5 deg
Chord length T106$^{\mathrm{RUB}}$	$C_{\mathrm{Stator}} = C$	0.1 m
Pitch T106$^{\mathrm{RUB}}$ at mid-span	g_{Stator}	0.078 m
Stagger angle T106$^{\mathrm{RUB}}$	$\lambda_{\mathrm{Stator}}$	30.7 deg
Blade count IGV, T106$^{\mathrm{RUB}}$	$N_{\mathrm{IGV}} = N_{\mathrm{Stator}}$	60
Design flow angles at mid-span:		
IGV inflow	α_0	90 deg
IGV outflow = T106$^{\mathrm{RUB}}$ inflow	$\alpha_1 = \alpha_2$	127.7 deg
T106$^{\mathrm{RUB}}$ outflow	α_3	26.8 deg
Axial distances:		
IGV TE to bar plane	x/C_{Stator}	2.61
Bar plane to T106$^{\mathrm{RUB}}$ LE	x/C_{Stator}	0.33
Bar diameter	D_{Bar}	0.002 m
Bar length	L_{Bar}	0.168 m
Bar count	N_{Bar}	60
Bar pitch at mid-span	g_{Bar}	0.078 m
Operating point/Design point		
Mass flow	$\dot{m}$	12.8 kg/s
Reynolds number	$\mathrm{Re}_{\mathrm{exit,th}}$	200,000
Mach number	$\mathrm{Ma}_{\mathrm{exit,th}}$	0.091
Strouhal number range	Sr	0.6-3.15
Flow coefficient range	ϕ	0.81-2.84

3.2 Numerical Setup

This section comprises all settings which are relevant for the creation of the numerical model. Special focus is put on the a priori estimation of the grid resolution needed for an adequately resolved LES, on the derivation of the imposed boundary conditions and the definition of an efficient transient data output.

3.2.1 Spatial discretization

3.2.1.1 Numerical domain

As described in section 3.1.1, the test rig basically consists of three main components, namely the IGV, the rotating wake generator, and the stator grid under investigation (see Fig. 3.1). Since three-dimensional simulation of all these components using LES would far exceed the available computing resources, some simplifications had to be made a priori. Special care must be taken that these simplifications do not distort the effects of the boundary layer transition in the area of the suction-side trailing edge. Basically, three simplifications were made, which are summarized in the following:

- **Component reduction**
  The first measure is the reduction of the components. This is achieved in the present case by neglecting the IGV in the numerical domain, since in CFD the flow angle can be simply specified via the boundary condition at the inlet. However, the influence of the wake of the IGV must not be neglected, as numerical preliminary studies have shown, and a way must be found to reproduce it with the help of the boundary conditions, which will be discussed in detail in the following section.

- **Dimensional reduction**
  The second measure is a reduction of the spatial dimension. For this purpose, the numerical model is reduced to a finite width section at midspan, whereby end wall effects (hub and casing) are neglected. This is only possible if the curvature of the annular channel is neglected, so that periodic boundary conditions at the blade "ends" can be assumed. This simplification is widely used in the field of numerical analysis of transition phenomena by means of scale-resolving methods [81, 82, 107]. It is reasonable because of the assumption that in case of high aspect ratio blading the flow in the middle section of the blade is largely uninfluenced by the secondary flow effects which develop due to the end wall boundary layers.

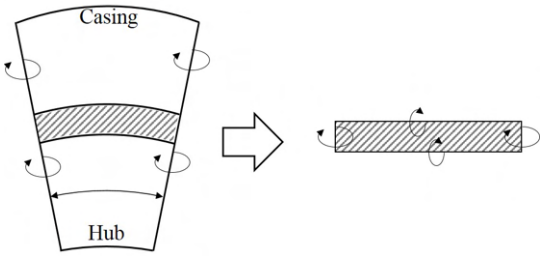

Figure 3.3: Schematic drawing of the transformation from an annular to planar midspan section. Periodic boundary conditions are indicated by circular arrows.

That this assumption is not completely correct in the underlying case will be shown in the following, however it is possible to eliminate the errors that are caused by this simplification.

- **Utilizing periodicities**
  Since the test case under consideration is an annular test rig, there is a circumferential periodicity for both the wake generator and the stator row, which in the 2-dimensional case turns into a translational periodicity (cf. Fig. 3.3). As both components have the same pitch (60 bars and 60 vanes) only one instance of each component has to be modeled.

The numerical domain resulting from these simplifications is shown in Fig. 3.4 for the perturbed configuration. All domains are stationary except the hatched subdomain, which contains the wake generator, that moves translatorily in the indicated direction along the investigated stator profile. The translational movement is the result of the above described reduction to a two-dimensional mid-span section, which requires the conversion of the rotational movement into a translational movement. In the unperturbed inflow configuration the wake generator is not modeled and the stator domain is simply extended to the same inlet position as in the perturbed case.

The dimensions of the numerical domain mainly result from the conditions of the experimental setup, which can be found in table 3.1. The distance between inlet and blade leading edge was chosen so that the inlet lies exactly on the measuring plane in which the fields for the boundary conditions were measured, so that these can be directly imposed without additional transformations. It is important that this distance is large enough so that the turbulence, which is artificially generated at the inlet by a numerical method, can develop. This is ensured in this case, which will be discussed in the following chapter.

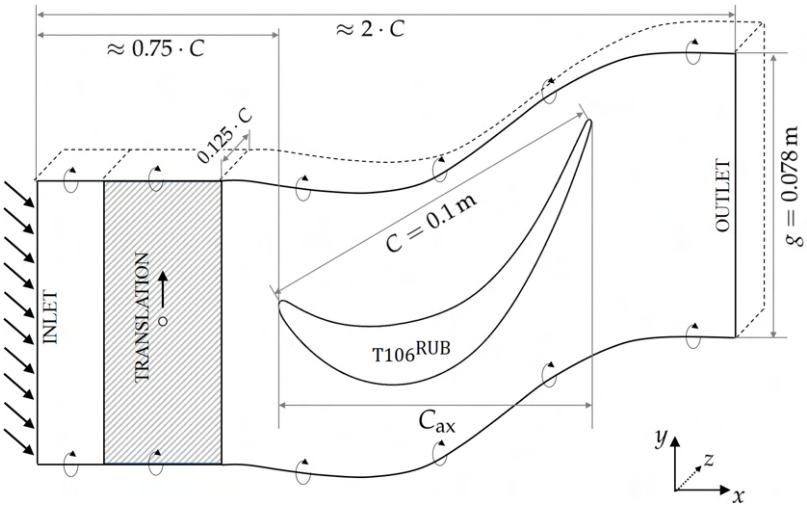

Figure 3.4: Schematic drawing of the numerical domain including the translating wake generator and the $T106^{RUB}$ stator vane. Periodic boundary conditions are indicated by circular arrows.

In spanwise direction (z-direction) the extension of the domain was set to $0.125 \cdot C \approx 0.15 \cdot C_{ax}$ according to the literature, where recommended values lie in the range of $0.15 \cdot C_{ax}$ [80, 118].

3.2.1.2 Numerical mesh

The creation of the numerical mesh is a key point in the topic of LES, because it defines the spatial filter in the implicit sense, and as a consequence also the part of the actually resolved turbulent energy spectrum (cf. section 2.3.3.3). As the filter width is defined by the mesh size, a mesh independence as it exists in a RANS approach is not possible in the case of a LES (neglecting numerical errors mesh independence would mean a DNS).

It is therefore important to adhere to explicit guidelines when generating numerical meshes for LES applications, so that the simulation results are reliable and time-consuming iteration loops can be avoided. One of these guidelines is the measure of the turbulent kinetic energy k, which, according

to *Pope* [95], results e.g. from the integration of the turbulent kinetic energy spectral density $E(\kappa)$:

$$k = \int_0^\infty E(\kappa)\,\mathrm{d}\kappa. \tag{3.3}$$

It is generally reported in the literature that at least 80% of the turbulent energy spectrum must be resolved for a well resolved LES [95]. To be able to assess this criterion a priori, a few basic considerations have to be made, which are fundamentally based on the theory of turbulent scales described in the section 2.3.3.2.

By looking at figure 2.14 it becomes clear that most of the turbulent kinetic energy is concentrated in the low wavenumber range and peaks in the range of the integral length scale l_0. Now the question arises up to which wave number 80% of the energy has already accumulated so that the computational grid can be designed in such a way that these scales can be adequately resolved.

However, since the shape of the energy spectrum is not known a priori, a model must be used, which usually results in some simplifying assumptions. The energy spectrum of isotropic turbulence is given by *Pope* [95]:

$$E(\kappa) = C\varepsilon^{2/3}\kappa^{-5/3} f_L(\kappa L) f_\eta(\kappa\eta) \tag{3.4}$$

$$f_L(\kappa l_0) = \left(\frac{\kappa L}{[(\kappa L)^2 + C_l]^{1/2}}\right)^{5/3+p_0} \tag{3.5}$$

$$f_\eta(\kappa\eta) = \exp\left(-\beta\left[[(\kappa\eta)^4 + C_\eta^4]^{1/4} - C_\eta\right]\right). \tag{3.6}$$

In case of isotropic turbulence at high Reynolds numbers, *Pope* [95] specifies the constants as follows:

$$C = 1.5 \qquad C_l = 6.78 \qquad p_0 = 2 \qquad \beta = 5.2 \qquad C_\eta = 0.4 \tag{3.7}$$

Equation 3.4 depends on the length scale $L = k^{3/2}/\varepsilon$, the Kolmogorov length scale η, the dissipation rate ε and the wave number κ.

A meaningful scaling is given by $E(\kappa)/(kL_{11})$ according to *Pope* [95] and visualized in Fig. 3.5 (left). Here L_{11} represents the longitudinal length scale which in case of high Reynolds numbers corresponds to $L_{11} \approx 4/(3\pi) \cdot L$. The turbulent kinetic energy can be calculated using

$$k = (L\varepsilon)^{2/3}. \tag{3.8}$$

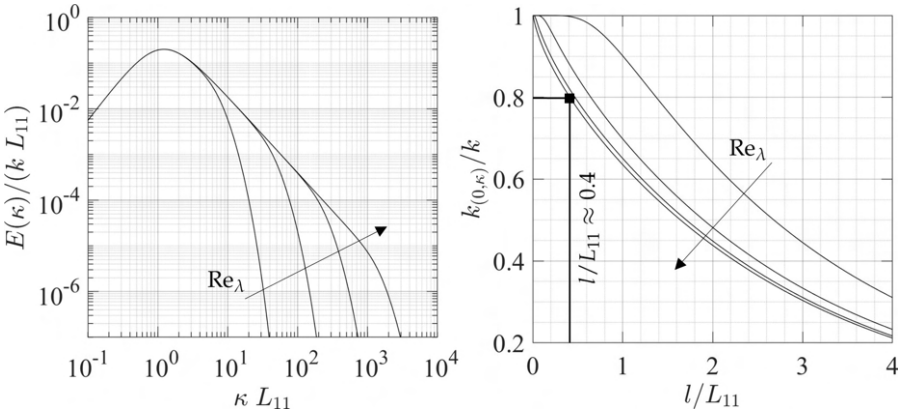

Figure 3.5: The model spectrum for various Reynolds numbers (Re_λ = 30, 100, 300, 1000; Re $\approx$ 450, 5000, 45000, 500000), scaled by k and L_{11} (left). Cumulative turbulent kinetic energy $k_{(0,\kappa)}$ against wavelength $l = 2\pi/\kappa$ for the respective model spectra (right).

The resulting scaled equation is thus only dependent on the turbulent Reynolds number via the ratio $\eta = l_0 \cdot \mathrm{Re}_L^{-3/4}$, which is linked to the Taylor-scale Reynolds number via $\mathrm{Re}_L = \frac{3}{20}\mathrm{Re}_\lambda^2$ [95].

In order to identify up to which length scales the numerical grid has to be resolved to adequately capture at least 80% of the turbulent kinetic energy, Eq. 3.4 has to be integrated cumulatively. The result is shown in Fig. 3.5 (right) for the same Reynolds numbers. It is clearly visible that at a level of 80% of the total energy for increasing Reynolds numbers the curves approximate a value of $l/L_{11} \approx 0.4$ (cf. *Pope* [95]).

This means that structures corresponding to about 40% of the size of the longitudinal length scale L_{11} must be captured by the numerical mesh. This requires at least 4 grid cells in each spatial direction, which is why the grid spacing Δ has a maximum value depending of the respective length scales of $\Delta \approx 0.1 \cdot L_{11} \approx 0.043 \cdot L$.

It is important to note that L is not a global size, but varies with the flow. For the final grid design, an iterative process consisting of several precursor RANS simulations was carried out, with the help of which the length scale L was calculated based on

$$L = \frac{k^{1/2}}{C_\mu \omega}, \tag{3.9}$$

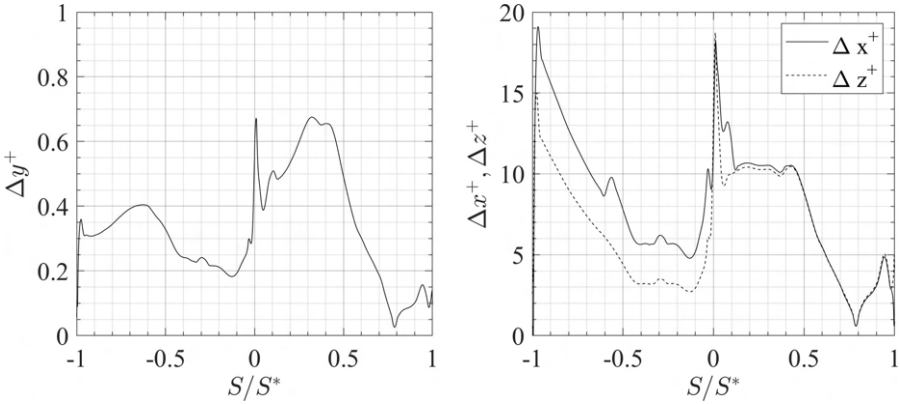

Figure 3.6: Time averaged near wall resolution along the blade profile for the final LES mesh at the unperturbed inflow operating point with free stream turbulence (OP-CT).

with the model constant $C_\mu = 0.09$ and the turbulence eddy frequency ω, in each cell of the grid and on which basis the grid was carefully adjusted.

Since the considered model spectra as well as the background of Eq. (3.8) are based on simplifying assumptions, this is procedure is only a rough estimate and can therefore only be considered as a guideline. Whether the final computational mesh actually meets the requirements can only be determined a posteriori by checking suitable quality criteria, which is shown in chapter 4.2.

A further criterion, which plays an essential role in the grid creation for wall resolved LES, is the compliance with the guidelines for non-dimensional wall distances. According to *Piomelli and Chasnov* [94] the first grid point must be located at $\Delta y^+ < 2$ (wall normal spacing) and the grid spacing must be of order $\Delta x^+ \simeq 50 - 150$, $\Delta z^+ \simeq 15 - 40$ (tangential/spanwise direction), while *Chapman* [15] gives values of $\Delta^+ < 2/100/20$. The non-dimensional grid spacing in streamwise direction is given by: ,

$$\Delta x^+ = \frac{\Delta x u_\tau}{\nu}, \tag{3.10}$$

with the absolute grid spacing Δx and $u_\tau = \sqrt{\tau_w/\rho}$. The other components are obtained accordingly.

Since these values depend on the local wall shear stress velocity, which is unknown a priori, the node distributions have to be adjusted iteratively with

Table 3.2: Main mesh parameters for both, the unperturbed inflow (OP-C) case, and the perturbed (OP-W) case.

		OP-C/OP-W
Total number of elements	$n_{\text{tot.}}$	$70.0/72.2 \times 10^6$
Points around profile (T106)	$n_{\text{p,T106}^{\text{RUB}}}$	2080
Points around profile (wake gen.)	$n_{\text{p,WG}}$	300
Points spanwise	n_{span}	121
1^{st}-element offset (T106)	$\Delta y_{\text{T106}^{\text{RUB}}}$	$\approx 5 \times 10^{-6}$ m
1^{st}-element offset (wake gen.)	Δy_{WG}	$\approx 2 \times 10^{-6}$ m
Max. wall distance	$\Delta^+_{\text{max}}(x/y/z)$	20.45/0.78/20.64
Avg. wall distance	$\Delta^+_{\text{avg}}(x/y/z)$	7.74/0.34/6.74

precursor RANS simulations. The resulting time-averaged distributions are shown in Fig. 3.6 for the unperturbed inflow case with inflow turbulence (OP-CT) along the non-dimensional surface fraction S/S^*. It can be clearly seen that the reference values from the literature are far undercut. This is intended, because, as described in section 2.4.2, only 2nd order schemes can be realized efficiently by the application of FVM for spatial discretizations. This deficit can only be compensated by a finer local discretization, so that structures of higher wavenumbers can be resolved adequately. Near the blade surface, the used mesh can thus be regarded as a highly resolved LES mesh even close to the used DNS resolution by *Michelassi et al.* [80].

The final grid is a block structured grid which is shown in Fig. 3.7. For the perturbed case it consists of 28 blocks, while for the unperturbed inflow case the number of blocks reduces to 21. The grid was created with ANSYS ICEM first as a 2-dimensional planar grid and was then extruded in z-direction. Special care was taken to ensure that the expansion ratio did not exceed 1.1 in the vicinity of the blade surface. Final smoothing of the grid also ensures smooth transitions between adjacent cells throughout the entire domain, thus preventing major volume changes. Main mesh parameters are summarized in Table 3.2.

3.2.2 Boundary conditions

The boundary conditions (BCs) are discussed in the following, whereby the focus is on the inlet BC, since an inhomogeneous distribution of the flow variables must be specified at this point due to the neglected IGV in the numerical model (cf. section 3.2.1.1). All other boundaries have translational

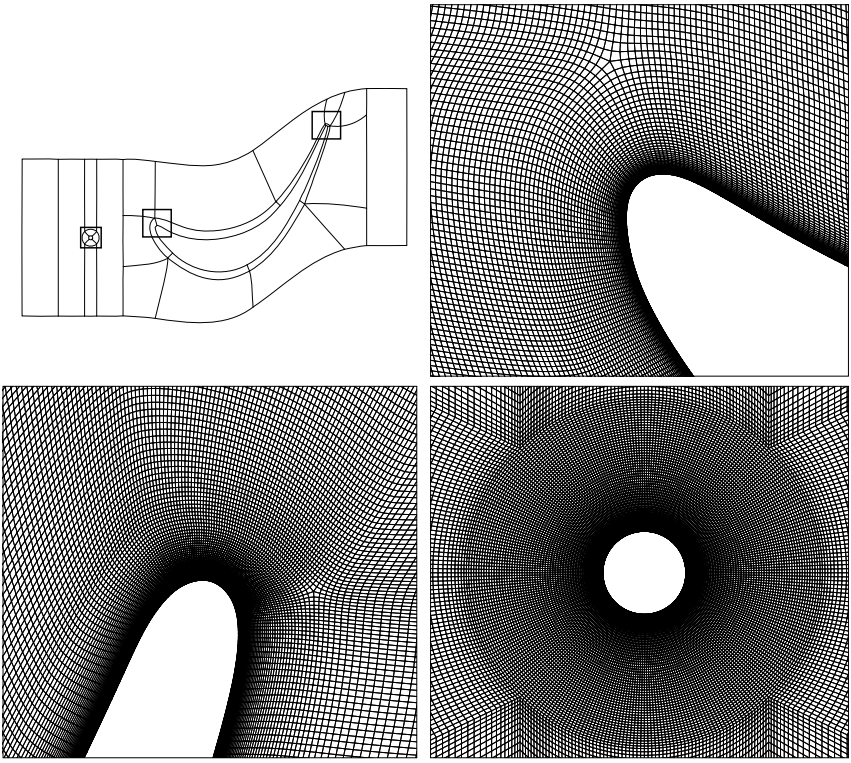

Figure 3.7: Blocking structure of the numerical domain for the wake disturbed case (top left), and closeups for selected mesh regions near the blade's leading edge (top right), the blade's trailing edge (bottom left) and the cylindrical wake generator (bottom right).

periodic boundary conditions except the outlet, where an average static pressure is specified, and in the case of the perturbed simulations the sliding interface, which connects the rotating and stationary domains.

For the determination of the inlet BC, a 2-dimensional field was experimentally determined 75 mm ($0.75 \cdot C$) upstream of the stator leading edge by means a of a 5-hole probe traverse. This yields the time-averaged velocity vector components which are imposed at the inlet of the numerical domain. For the sake of brevity only the time mean absolute velocity distribution $\overline{c}(r, \theta)$ is shown in Fig. 3.8 (left). To get a better impression, the distribution of a single pitch was duplicated.

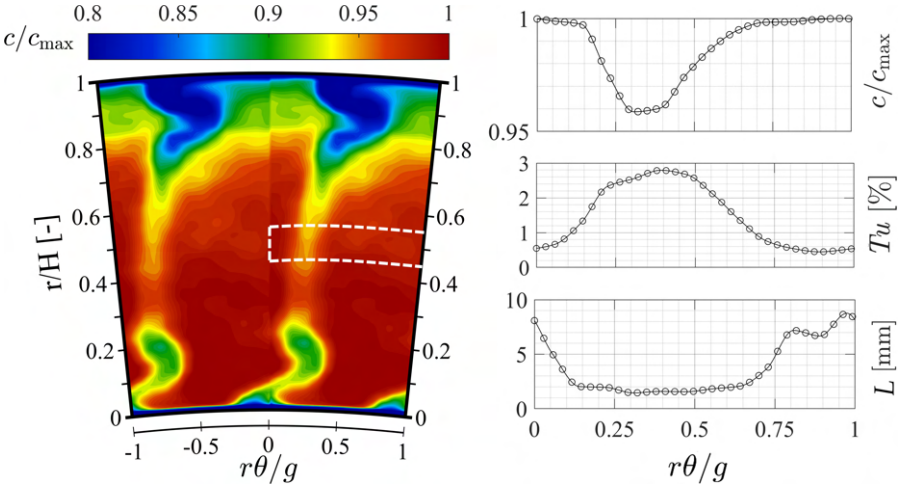

Figure 3.8: Distribution of the non-dimensional time mean velocity $\overline{c}/c_{\max}$ at a plane $0.75 \cdot C$ upstream of the T106$^{\text{RUB}}$ leading edge (left, view against flow direction), and distributions of the non dimensional time mean velocity (right top), turbulence intensity Tu (right middle) and length scale L (right bottom) at mid-span.

The wake of the IGV as well as the secondary flow regions are clearly visible as areas of reduced velocity. Although the secondary flow regions are very pronounced, they do not merge at the blade's mid-span section (dashed area).

Since the information about the turbulence properties are of special interest for the inlet BCs in case of scale-resolving simulations, additional hot-wire traverses were carried out by *Sinkwitz* [127] in the relevant mid-span section. Figure 3.8 (right) shows the distributions of absolute velocity (all three components were measured), turbulent intensity Tu and length scale L. The turbulent intensity can be calculated according to:

$$Tu = \frac{1}{|\overline{\boldsymbol{u}}|}\sqrt{\frac{1}{3}\left(\sigma_u^2 + \sigma_v^2 + \sigma_w^2\right)} = \frac{1}{|\overline{\boldsymbol{u}}|}\sqrt{\frac{1}{3}\overline{u_i' u_i'}}, \tag{3.11}$$

with the standard deviation σ of the respective velocity components.

Furthermore, the length scale can be determined according to the method presented by *Roach* [103], which is an empirical approach mainly based on the analysis of the power spectra of the hot wire signals.

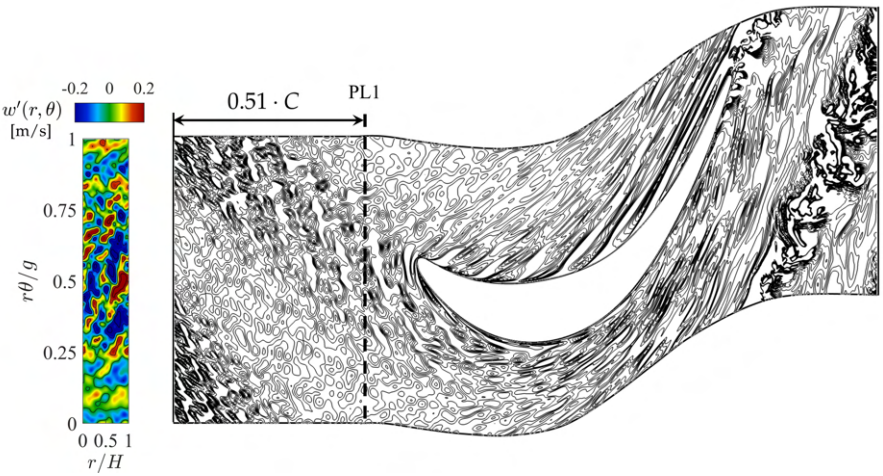

Figure 3.9: Distribution of instantaneous velocity component $w(r, r\theta, t)$ at evaluation plane PL1(left), and blade to blade visualization of instantaneous velocity component $w(x, r\theta, t)$ (right)

The measurements clearly show an increase in turbulent intensity to about 2-3% within the IGV wake. The length scales are clearly reduced in this range (approx. 1-2 mm) compared to the free stream (approx. 6-9 mm). The measured course of the turbulent variables can therefore be considered plausible.

Since for the specification of the turbulence the solver requires the distributions of the turbulent kinetic energy k and the turbulent dissipation rate ε, the measured distributions are determined with the help of the relations

$$k = \frac{3}{2} \left(|\overline{\boldsymbol{u}}| \cdot Tu \right)^2 \quad \text{and} \quad \varepsilon = \frac{k^{3/2}}{L} \tag{3.12}$$

and imprinted as profiles at the inlet.

For generating artificial turbulence at the inlet of the numerical domain, the *Synthetic Turbulence Generator* implemented in ANSYS FLUENT was used for all simulations including free stream turbulence. It is a Fourier based turbulence generator, which is based on a Cholesky decomposition of the Reynolds stress tensor. More information can be found in the publication of *Shur et al.* [120].

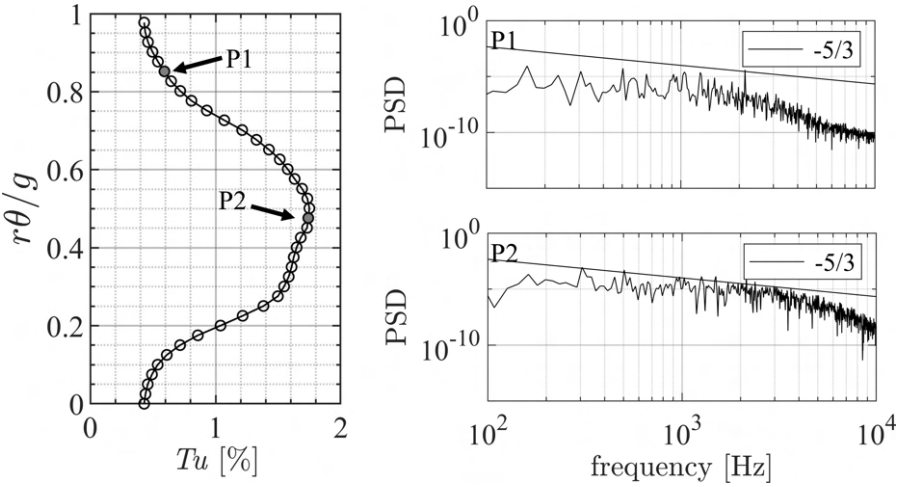

Figure 3.10: Distribution of turbulence intensity in pitch direction inside PL1 (left), power spectral density (PSD) for two distinct points P1 and P2 inside PL1 (right)

In order to finally check whether the synthetically generated turbulence corresponds to the desired specifications, it is analyzed below within an evaluation plane $0.51 \cdot C$ downstream of the inlet (cf. Fig 3.9).

On the left side of Fig. 3.9 the distribution of the z component w of the velocity vector is shown. Due to the reduced length scale, significantly smaller turbulent structures can be detected within the wake influenced flow compared to the free flow. These smaller structures cause stronger fluctuation velocities, which is caused by the increased degree of turbulence. All structures appear randomly distributed and no deterministic formations are visible.

In order to determine the turbulence intensity based on the actually resolved fluctuation velocities, the fluctuation signals of the velocity components are now analyzed within the evaluation plane PL1 and evaluated using Eq. (3.11). In pitch direction the resulting curve is shown in Fig. 3.10.

In comparison to the curves given at the inlet (see Fig. 3.8), it is noticeable that the turbulence intensity has decreased from about 2.8% to 1.8% in maximum, which is caused by the natural turbulence decay as described in section 2.3.3. The qualitative course has not changed significantly by convection and shows a similar pattern as the measured distribution, which was imprinted at the inlet. These observations confirm that the global structure of the turbulence is well reproduced by the used method. To further illus-

trate the local structure, the power spectral density (PSD) over the frequency is shown on the right side of Fig. 3.10.

The courses of both spectra show a typical pronounced turbulent broadband spectrum.The energy level for point P2 is significantly higher compared to point P1 due to the higher degree of turbulence. This is particularly noticeable in the range of higher frequencies, which is attributable to the smaller turbulent length scale.

3.2.3 Source term

As mentioned before, the reduction of the computational domain to the blade's mid-span section is permissible without restrictions only if the flow in this area can be regarded as almost unaffected by wall (hub & shroud) effects. Since these cannot be taken into account by the application of simple periodic boundary conditions. In a first approximation, this applies to blades with high aspect ratios, as is usually the case in LPT.

In the present case, however, the blade is not of high aspect ratio, since this had to be subordinated to the requirements on the Reynolds number in the design of the test rig. It is therefore essential to quantify in advance, with the aid of experimental data or 3-dimensional CFD calculations, whether the flow in the center section of the blade is influenced by these effects, and if so, how strongly.

Within this work, this was done using a combined approach based on 3-dimensional URANS calculations and experimental 5-hole probe measurements. This has the advantage of simultaneously verifying the numerical predictions against the experimental data, thus ensuring the validity of the applied boundary conditions. For the sake of brevity only the major outcomes regarding the mid-span flow field are presented here, whereas a detailed description of the setup and a more thorough analysis of the results has been published in *Winhart et al.* [148, 149].

Figure 3.11 (left) shows the numerical domain used for the calculation of the 3-dimensional URANS simulations together with the imposed inlet boundary profile (see Fig. 3.8) for the perturbed operating point. For the unperturbed inflow case the rotating bar domain is omitted and the stator domain extends to the same inlet position.

The right side of the figure shows a comparison between the data measured experimentally by 5-hole probe measurements (left half) and the URANS

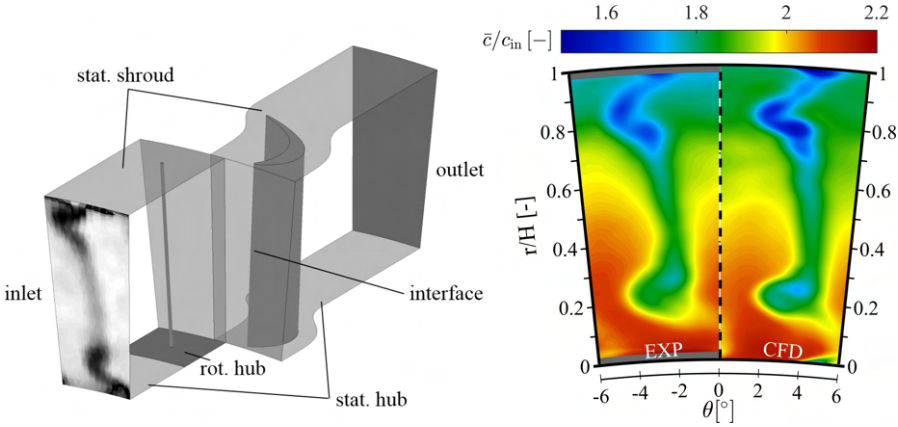

Figure 3.11: Computational domain with imposed inlet boundary profile used for the URANS simulations (left), and comparison between experimentally measured velocity distribution and CFD predictions downstream of the investigated stator vane (right, view against flow direction).

predictions (right half). The measurement plane is located $0.34 \cdot C$ downstream the stator blades trailing edge and the viewing direction here is against the direction of flow.

In a first glance, it can be observed that the CFD reproduces the 3-dimensional flow field very well. Both the characteristics of the secondary flow regions near hub and shroud and the asymmetry of the flow topologies due to the annular test rig are in excellent agreement with the experimental profiles. On the one hand this indicates that the boundary conditions derived from the experimental measurements are plausible. On the other hand further analysis based on the verified numerical model are justified.

It can be further observed that the secondary flow regions do not merge in the mid-span region and thus do not directly interact with the boundary layer flow in this area, which would make a reduction of the numerical domain to this region inadmissible.

Nevertheless, it is clearly visible that the secondary flow regions take up a considerable part of the total passage flow, which leads to a blocking of the passage due to the reduced momentum in these regions (blue areas) and thus gives rise to a radial contraction of the streamlines. Since this streamtube contraction also affects the flow close to the wall in the area of the mid-

span section, it can be assumed that the flow is indirectly influenced to a considerable extent.

To account for this effect the approach of *Giles* [30] was followed in this work, where an additional source term is added to the x-momentum equation. The basic idea behind this approach is that the acceleration of the flow is proportional to the contraction of the stream tube caused by the secondary flow effects.

Assuming that the axial velocity would remain constant over the blade row in the absence of secondary flow effects, the contraction of the flow tube can be derived from the ratio of the axial velocity component up- and downstream of the blade row. Considering the stream-tube to vary only in the axial direction, the modified governing equations read

$$\frac{\partial U}{\partial t} + \nabla \cdot (\boldsymbol{F}_{\mathbf{inv}} - \boldsymbol{F}_{\mathbf{visc}}) = S \tag{3.13}$$

where $\boldsymbol{F}_{\mathbf{inv}}$ and $\boldsymbol{F}_{\mathbf{visc}}$ are the inviscid and viscous fluxes of the Navier-Stokes equations, respectively, and S is the streamtube correction which according to *Giles* [30] reads:

$$S = \frac{1}{h} p \frac{\partial h}{\partial x} [0 \;\; 1 \;\; 0 \;\; 0]^T - \frac{1}{h} \frac{\partial h}{\partial x} F, \tag{3.14}$$

where p is the static pressure, h is the height of the stream tube and F is the inviscid flux in axial direction.

Since the flow tube does not contract along the entire blade passage, the additional source is only switched on between the suction peak of the profile and the trailing edge. The implementation of the additional source term is realized by a C routine, which is hooked to the solver via a user defined function.

It should be noted at this point that the incoming wakes influence the characteristics of the secondary flow areas and therefore ultimately also the contraction of the stream tube, which is why the stream tube contraction must be derived individually for each operating point.

3.2.4 Transient setup

This section summarizes the most important considerations and settings which have been made for the realization of the scale-resolving simulations. In particular, the temporal discretization and the acquisition of transient statistics are discussed.

3.2.4.1 Temporal discretization

The numerical time step was determined iteratively, paying attention that the maximum *Courant Friedrichs Lewy* (CFL) number $\mathrm{CFL}_{\max} \ll 1$ was fulfilled in the entire numerical domain. This strict guideline is justified by the use of the NITA procedure, as mentioned in section 2.4.5.

A further guide line is given by the circumferential speed of the wake generator (WG). The time step has to be chosen in a way, that it fits as integer into a passing period and can be calculated according to

$$\Delta t = \frac{60}{n_{\mathrm{WG}} \cdot N_{\mathrm{bar}} \cdot N_{\mathrm{steps}}}, \tag{3.15}$$

where n_{WG} is the speed of the wake generator in rpm, while N_{bar} and N_{steps} represent the number of bars and the desired number of time steps per passing. Related to a rotational speed of 180 rpm (OP-W-180) and 7500 time steps per bar passing, this results in a time step width of $\Delta t \approx 7.4074 \times 10^{-}7\,\mathrm{s}$.

Since this operating point is the most critical with respect to the maximum CFL number, this time step was also adopted for all other operating points, although it must be taken into account that a simulation with a WG speed of one third also results in three times the computing effort in terms of time steps.

It should be noted that for this reason and for a better comparability also for the simulations without wake influence OP-C the simulation time is related to the WG passings for the high rpm case OPW-180.

3.2.4.2 Initialization & transient statistics

The simulations with wake disturbance were computed in each case for five bar passings ($5 \cdot 22500$ steps for OP-W-60 and $5 \cdot 7500$ steps for OP-W-180) as so-called initialization runs to clear the initial transients, while the unperturbed inflow cases were initialized for the same number of time steps as the OP-W-180 case.

After the initialization runs, ten more bar passings are performed for the transient data output and the acquisition of the transient statistics (output runs). This corresponds to a total simulation time for the output runs of $T \approx 0.0556\,\mathrm{s}$, which is equivalent to about 3.5 flow-through times (FTT) for the OP-W180 case and approximately 10.5 FTT for the OP-W60 case.

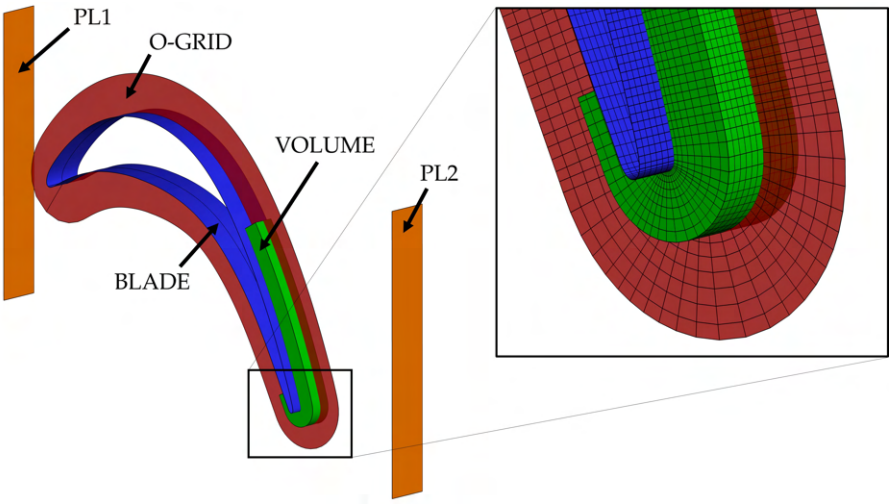

Figure 3.12: Overview of the evaluation regions for the transient data output (left), and detailed view of the blade's trailing edge region with grid lines (note: every 5^{th} grid line shown).

3.2.5 Data output

The transient data output plays a crucial role in the field of scale-resolving simulation of fluid flows. This is due to the high spatial and temporal resolution, which, depending on the sampling frequency, results in a high number of large output files. However, since the sampling frequency cannot be reduced arbitrarily, as otherwise important information about the expensively generated turbulent motions would be lost, another way must be found to reduce the data output to a tolerable level.

In the simulations presented in this thesis, the data output was realized with the help of separately created structured evaluation grids in the relevant areas. These grids were created using PYTHON routines and adapted to the requirements in terms of spatial resolution, so that transient data can be written quasi independently of the local distribution of the computational grid. In contrast to the native data output of ANSYS Fluent, which has no definable structure due to the unstructured formulation of the solver, the interpolation regions are all built in a structured way, which considerably facilitates the later evaluation of the data.

To enable an interpolation of the solution of the respective time step to the particular evaluation grids, several C program routines were developed, which can be used within ANSYS FLUENT using the so-called *user defined functions* UDFs. The sequence is divided into the following steps:

Prior to the simulation:

- **Importing the coordinates**
  In the first step, the coordinates generated by the PYTHON script are read from ASCII files and stored in the respective fields.
- **Determining the cell centroids**
  The centroid coordinates of the cells in which the respective points are located are determined and stored using an octree based search algorithm, which is performed on each individual CPU. Furthermore, the distance vector between cell centroid and the interpolation point is determined and stored.

During the simulation:

- **Interpolation**
  The desired scalar flow quantity $\phi(\boldsymbol{x}, t)$ is interpolated at the respective coordinate by a gradient based linear interpolation:

$$\phi(\boldsymbol{x}, t) = \phi_0 + (\boldsymbol{x_{int}} - \boldsymbol{x_0}) \frac{\partial \phi}{\partial x_i}, \tag{3.16}$$

  where $\boldsymbol{x_{int}}$ is the coordinate of the interpolation point and $\boldsymbol{x_0}$ the coordinate of the cell centroid.

A total of five interpolation regions were defined, which are shown in Fig. 3.12 They differ both in their dimensions and in their respective sampling rates. The most important parameters are summarized in Table 3.3. It should be noted, that for the OP-W60 operating point the number of files and total file size triples.

3.2.6 Computational cost

At this point, the computational effort of the simulations presented in this paper should be briefly discussed, as this is the main criterion for the applicability of such scale-resolving simulations.

All simulations presented were performed on the in-house High-Performance Computing (HPC) cluster of the Chair of Thermal Turbomachines and Aero Engines, whose main specifications are summarized in Table 3.4.

Table 3.3: Summary of the main parameters for the transient data output regions.

	Sampling frequency	Spatial resolution	Number of files	Total size
O-GRID	67.5 kHz	2080/75/1	3750	22 GB
PL1/PL2	270 kHz	1/200/40	15000	4.5 GB
BLADE	27 kHz	2080/1/121	1500	15 GB
VOLUME	33.75 kHz	633/61/40	1875	110 GB
TOTAL				**151.5 GB**

In total 20 compute nodes of the #1 partition of the HPC cluster were allocated in all runs, resulting in a total number of 560 CPU cores. In the case of the simulations without wake generator, this resulted in a total computing time of about 4 days, which corresponds to about 400 core weeks. In the case of the simulations with wake generator, the calculation time for the high speed case (180 rpm) was approx. 8 days, i.e. approx. 640 core weeks. This effort triples in the case of low speed (60rpm), which corresponds to a total computing time of about 24 days or about 1920 core weeks.

Overall, the computation times in the case of perturbed operating points are higher than for the unperturbed inflow cases, despite the roughly equal number of grid nodes. This is due to the fact that no turbomachine-optimized interface handling is implemented in ANSYS Fluent for the required translational sliding interface, so that the entire wake generator domain must be moved in each time step.

Compared to the approx. 7 core weeks of the fully 3-dimensional (U)RANS simulations, which were briefly discussed in section 3.2.3 and published in [148, 149] in more detail, this results in an approx. 2 orders of magnitude higher computational effort.

Table 3.4: Summary of the main specifications of the HPC cluster.

Partition	Number of nodes	Cores per node	CPU type	RAM	Interconnect
#1	28	28	Intel Xeon "Skylake" Gold 6132 @2.6 GHz	96 GB	Intel Omni-path
#2	8	40	Intel Xeon Scalable Gold 6248 @2.5 GHz	96 GB	Intel Omni-path
TOTAL	**36**	**1104**		**3.4 TB**	

3.3 Post processing procedures

In this chapter, the basic principles of the analysis methods used in this work are presented. The focus here is on a basic description of the functionality and the principle of application; for more in-depth details, please refer to the literature cited in each case.

3.3.1 Statistical moments

For all applied statistical moments, the number of samples should ideally strive towards infinity, which is difficult to achieve especially in the case of scale-resolving CFD simulations. Especially in the present case, where in comparison to the applied time step a very low frequency disturbance due to wake passings dominates the transient flow pattern, an ordinary evaluation of the statistics leads to a blurring of the global wake effects. In this case a phase-locked evaluation has to be carried out, which drastically reduces the number of input data that can be used for averaging due to the limited number of simulated wake passings.

To overcome this limitation, a combination of temporal and spatial averaging was used in this work in order to artificially increase the size of the statistical sample and reduce statistical error.. This is achieved, for example, by using not only one section in the middle of the blade span as data basis for the statistical moments on the blade surface, but all 120 available sections. This allows a total of 1200 data sets to be obtained from the only ten existing passing periods, which results in a significantly improved representation of the statistical moments. The efficiency of this procedure is discussed in more detail in later chapters and is graphically illustrated in Fig. 3.13.

3.3.1.1 Mean value

In this work, mean values are always referred to as time averages unless otherwise indicated. The discrete temporal mean value $\overline{\phi}$ of a quantity $\phi(t)$ is given by

$$\overline{\phi} = \frac{1}{N} \sum_{i=1}^{N} \phi(t_i). \tag{3.17}$$

As with all statistical moments described below, it is important to distinguish between a global and a phase-fixed mean value. In the present case, phase-fixed means that the mean value is only related to a fixed relative position between stator blades and rotating wake generator.

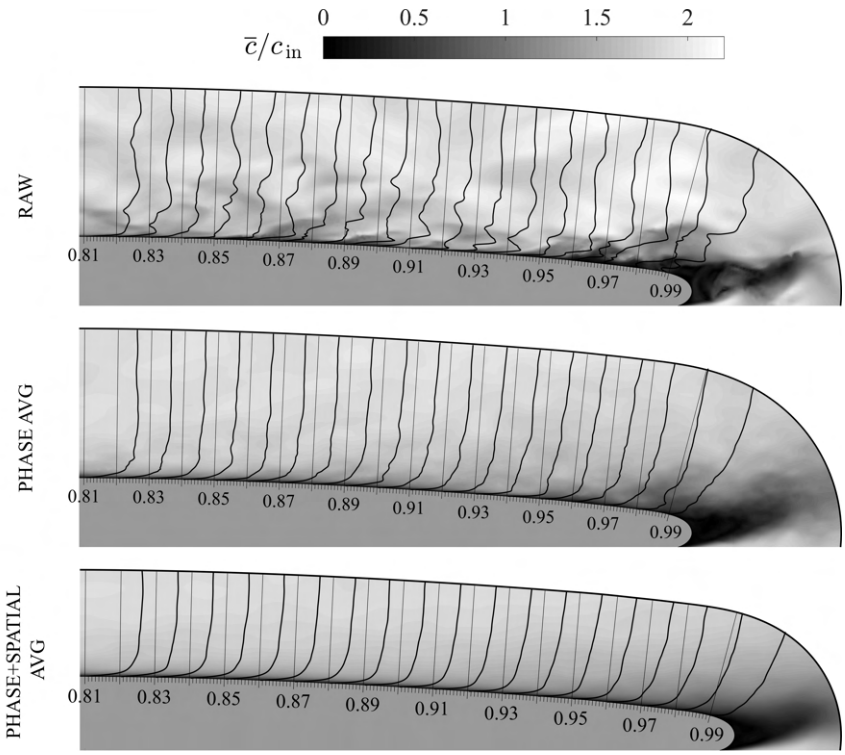

Figure 3.13: Influence of the averaging procedure on the distribution of the absolute velocity $\overline{c}$ in the vicinity of the blade surface for a distinct snapshot at OP-W180.

3.3.1.2 Standard deviation

The standard deviation σ measures the amount of variation or dispersion for a given set of values around its statistical mean value. The standard deviation is calculated using the following equation:

$$\sigma = \sqrt{\frac{1}{N}\sum_{i=1}^{N}\left[\phi(t_i) - \overline{\phi}\right]^2}. \tag{3.18}$$

Similar to the mean value, the standard deviation can also be evaluated in a phase-fixed manner.

3.3.2 Q-criterion

A valuable quantity to visualize vortex structures is provided by the q-criterion, which is defined as the second invariant of the velocity gradient tensor $\partial u_i / \partial x_j$:

$$Q = \frac{1}{2}(\Omega_{ij}\Omega_{ij} - S_{ij}S_{ij}), \tag{3.19}$$

with

$$\Omega_{ij} = \frac{1}{2}\left(\frac{\partial u_i}{\partial x_j} - \frac{\partial u_j}{\partial x_i}\right) \quad \text{and} \quad S_{ij} = \frac{1}{2}\left(\frac{\partial u_i}{\partial x_j} + \frac{\partial u_j}{\partial x_i}\right), \tag{3.20}$$

where Ω_{ij} is the vorticity tensor and S_{ij} is the rate-of-strain tensor. According to *Kolár* [54], it therefore represents the local balance between shear strain rate and vorticity magnitude, defining vortices as areas where the vorticity magnitude is greater than the magnitude of strain rate. [149]

3.3.3 Turbulence states

According to Pope, the Reynolds stresses have the greatest influence on the mean turbulent flow. These can be expressed in the Reynolds stress tensor (RST), which can be divided into a deviational and a rotational part according to the nature of stress tensors. The RST is a symmetrical tensor whose trace contains the normal stresses wich correspond to twice the turbulent kinetic energy k.

In order to analyze the respective different states within the turbulent spectrum, the anisotropy of the RST is determined with the help of the anisotropic part of the RST a_{ij}. For this purpose, the isotropic stresses $2/3\,k\,\delta_{ij}$ are simply subtracted from the RST:

$$a_{ij} = \overline{u_i' u_j'} - \frac{2}{3}k\delta_{ij}. \tag{3.21}$$

Normalization yields the anisotropy tensor:

$$b_{ij} = \frac{a_{ij}}{2k}. \tag{3.22}$$

In order to characterize turbulence based on the normalized anisotropy tensor b_{ij}, according to *Lumley and Newman* [66] it is not necessary to consider all six components. Instead, they propose to calculate the two invariants η and ξ based on its eigenvalues

$$\eta^2 = \frac{1}{3}(\lambda_1^2 + \lambda_1\lambda_2 + \lambda_2^2) \quad \text{and} \quad \xi^3 = -\frac{1}{2}\lambda_1\lambda_2(\lambda_1 + \lambda_2) \tag{3.23}$$

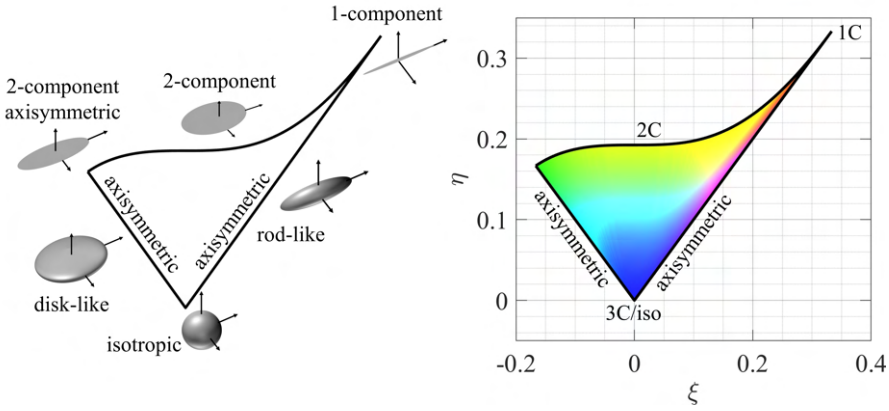

Figure 3.14: Anisotropy invariant map with graphical illustration of the turbulence states (left), and anisotropy invariant map colored by the *method of componentality contours* according to *Emory and Iaccarino* [24] (right).

and to evaluate them graphically within the so-called anisotropy invariant maps, with one of them being called Lumley triangle, named after him. The Lumley triangle is presented in Fig. 3.14 (left) and spans the space that is covered by the different combinations of η and ξ, with the corners and edges of this triangle representing the different states of turbulence. These are: isotropic (3C), axisymmetric, two-component (2C) and one-component (1C) turbulence. A detailed description of these states, is provided in *Simonsen and Krogstad* [122].

A weakness of the classical variant for the determination of turbulent states using the Lumley triangle is the assignment between the physical space and the data points entered in the invariant map. Due to the large data sets used in this thesis, it is almost impossible to make a meaningful assignment. To avoid this, the *method of componentality contours* according to *Emory and Iaccarino* [24] is used in this work, which maps a color scale to the Lumley triangle (cf. Fig. 3.14 (right)) and thus can serve as a color map for the visualization of 2-dimensional flow fields.

3.3.4 Spectral analysis

In order to identify the different mechanisms within the transition process, spectral analysis methods are used in this work, which are all based on an analysis of the collected time signals within the frequency domain.

The basic principles of such analytical methods is explained shortly in the following. A detailed descriptions, is provided in the text-book of *Bendat and Piersol* [10].

3.3.4.1 Discrete Fourier transform

The discrete Fourier transform (DFT) transforms a finite series of temporally equidistant samples of a function or distribution into a series of equal lengths of samples equidistant in frequency space, the so-called discrete-time Fourier transform (DTFT), which is a complex function of frequency. Here, the frequency interval of the DTFT is determined by the reciprocal of the total sampling time T of the discrete input signal $f[n]$.

The DTFT $F[k]$ of a discrete input signal $f[n]$ of finite length N is given by:

$$F[k] = \sum_{n=0}^{N-1} f[n] e^{-j\frac{2\pi}{N}kn}. \tag{3.24}$$

3.3.4.2 Welch's method

Since the signals to be expected in the present applications are highly nonlinear and stochastically superimposed due to turbulent effects, the frequency spectra obtained from these signals are usually also highly noisy, which makes an analysis of the different frequency components very difficult and often even impossible. To circumvent this problem, methods based on the convolution of the signals with the aid of suitable window functions provide a useful approach.

One popular method, which was employed within this work is the so called Welch's method, which was published by *Peter D. Welch* in 1967 [145] for the estimation of the power spectral density of a signal.

In this case, the output signal is first divided into individual segments which overlap to a certain extent and on each of which a frequency analysis by means of a DFT is then performed. Subsequently, the frequency information of the individual segments is averaged to obtain an averaged frequency spectrum of the overall signal.

Usually, each window is multiplied by a windowing function, which is multiplied by the original signal segment as a weighting distribution. A commonly used window function in this context is the so-called Hann window, which is based on a superposition of three spectrally shifted sinc-functions. For a discrete signal of length N, the weighting function w of Hann windows is given by:

$$w_{\text{hann}}[n] = \frac{1}{2}\left[1 - \cos\left(\frac{2\pi[n - N/2]}{N}\right)\right]. \tag{3.25}$$

3.3.4.3 Wavelet analysis

Although the method described above is suitable for obtaining information about the spectral components of a signal, the solution of this method, i.e. the DTFT, lacks an essential piece of information, namely the information of time. It is therefore not possible to assign points in time in the original signal to the different frequency components, which is particularly problematic if the characteristics of the underlying signal change over time. Since this is the case in the perturbed considerations, a simple DFT is not sufficient here, since it would be globally dominated by the wake passing frequency and the flow features occurring in the meantime would become blurred.

An efficient method to circumvent this problem is the continous wavelet transform (CWT). In contrast to conventional frequency domain analysis like the previously described DFT with fixed-length window functions, CWT enables the analysis of temporally resolved spectra by the use of adjustable time-frequency window functions. The scale decomposition is obtained by the translation and dilation of one single function, often referred to as "mother wavelet". As suggested by Farge [25], the Morlet wavelet is used in this work for the analysis of the turbulence data.

The CWT for a one dimensional vector $x(t)$ is given by the convolution of this vector with the adjustable window function $\psi_{ab}(t) = (1/\sqrt{|a|})\psi((t-b)/a)$:

$$CWT_x(a,b) = \frac{1}{\sqrt{|a|}} \int_{-\infty}^{\infty} x(t)\psi^*\left(\frac{t-b}{a}\right) dt \tag{3.26}$$

with the wavelet scale $a \in \mathbb{R}$ and $a \neq 0$, the time shift factor b and the complex conjugate of the wavelet function ψ^*.

The CWT of the time signal $x(t)$ can now be computed as the inverse Fourier transformation of $X(\omega)\Psi(a\omega)$

$$CWT(a,b) = \sqrt{a}\left\{\mathcal{F}^{-1}[X(\omega)\Psi(\omega)]\right\}_t. \tag{3.27}$$

The discrete form of this continuous transform is given by:

$$DWT_x(a,b) = \frac{\sqrt{|a|}}{N} \sum_{k=0}^{N-1} X(k)\Psi\left(a\omega\right) e^{i\omega nT}. \tag{3.28}$$

A detailed description is given in the monograph of *Pathak* [89] and the textbook of *Addison* [1].

3.3.5 Modal analysis

Simple aerodynamic configurations can exhibit complex flows with a wide range of temporal and spatial features even under simple conditions. In analyzing these flows, it is common practice to look for physically important features, which are also called modes, and extract them as the first step in the analysis. This step typically begins with a modal decomposition of an experimental or numerical data set of the flow field. To achieve this, the underlying dataset must first be decomposed by means of a suitable modal decomposition method. A review of the various methods relevant in fluid mechanics was published by *Taira et al.* [134] in 2017.

In the following, a basic overview of the functional principle of the applied decomposition method is given. Since the present case deals with spatially and temporally highly resolved 3-dimensional data sets, the computational aspect in terms of computational resources and time expenditure of the analysis will be discussed subsequently.

3.3.5.1 Proper orthogonal decomposition (POD)

For the modal decomposition of the transient 3-dimensional data sets, the method of proper orthogonal decomposition (POD) was used in this work. In the following, a superficial description of the basic functionality will be given. An extensive description is given in [11, 18, 43, 134, 144].

The proper orthogonal decomposition (POD) is a modal decomposition technique that extracts modes based on optimizing the energy content of the field variable being examined. It was first introduced in 1967 by *Lumley* [65] as a mathematical technique to extract coherent structures from turbulent flow fields. [134]

The basic idea behind the POD is to decompose a random fluctuating vector field $\boldsymbol{q'}(\boldsymbol{x},t)$, into a set of deterministic spatial functions $\boldsymbol{\phi_k}(\boldsymbol{x})$ modulated by random time coefficients $a_k(t)$ so that:

$$\boldsymbol{q'}(\boldsymbol{x},t) = \sum_{k=1}^{\infty} a_k(t)\boldsymbol{\phi_k}(\boldsymbol{x}). \tag{3.29}$$

Here $\boldsymbol{x} = (x,y,z)$ stands for the position vector and $\boldsymbol{q'}(\boldsymbol{x},t) = \boldsymbol{q}(\boldsymbol{x},t) - \overline{\boldsymbol{q}}(\boldsymbol{x})$ stands for a random fluctuation variable (e.g. velocity) vector field.

If the POD is calculated based on the velocity components $\boldsymbol{u} = (u,v,w)^T$, like in the underlying work, i.e. $q' = \boldsymbol{u'} = \boldsymbol{u} - \overline{\boldsymbol{u}}$, each mode represents a certain portion of the total TKE of the flow. The POD modes thus represent an optimal set of basis functions in that sense that a finite number of these orthogonal modes represent more of the TKE than any other set of orthogonal modes.

The method of POD used in this work is the so-called snapshot method according to *Sirovich* [128], which considerably reduces the required storage effort compared to the classical (spatial) POD, which makes the POD of data sets of the size used in this work possible on conventional workstations in the first place.

The process of modal decomposition is divided into the following steps:

1. In a first step the snapshot matrix $\boldsymbol{U}$ is created. For the 3-dimensional data sets investigated in this work, which have a spatial resolution of $n = 633 \times 61 \times 40$ points and contain $m = 3875$ time instances, the resulting snapshot matrix $\boldsymbol{U}$ has a dimension of $m \times n = 3875 \times 4,633,560$, i.e. approx. 8.7×10^9 entries.

   In this process, the 3-dimensional vector fields of the individual velocity fluctuation components are reshaped as 1-dimensional line vectors, horizontally concatenated and finally stacked onto each other so that each snapshot represents one row in the resulting snapshot matrix:

$$\boldsymbol{U} = \begin{bmatrix} u'(\boldsymbol{x},t_1) & v'(\boldsymbol{x},t_1) & w'(\boldsymbol{x},t_1) \\ u'(\boldsymbol{x},t_2) & v'(\boldsymbol{x},t_2) & w'(\boldsymbol{x},t_2) \\ \vdots & \vdots & \vdots \\ u'(\boldsymbol{x},t_m) & v'(\boldsymbol{x},t_m) & w'(\boldsymbol{x},t_m) \end{bmatrix}. \tag{3.30}$$

2. In a next step the covariance matrix $\boldsymbol{C}$ is computed:

$$\boldsymbol{C} = \frac{1}{m-1}\boldsymbol{U}\boldsymbol{U}^{\boldsymbol{T}}, \tag{3.31}$$

which is now an $m \times m$ matrix (approx. 3.5×10^6 entries compared to the $n \times n$ of the classical POD, which would result in approx. 21.5×10^{12} entries).

3. The POD modes are now determined as the Eigenvectors $\boldsymbol{\phi_k}(\boldsymbol{x})$ of the covariance matrix $\boldsymbol{C}$ from:

$$\boldsymbol{C}\boldsymbol{\Phi_k}(\boldsymbol{x}) = \lambda_k \boldsymbol{\Phi_k}(\boldsymbol{x}), \tag{3.32}$$

where the Eigenvalues λ_k represent the kinetic energy captured by the respective POD modes. If the eigenvalues are arranged from the largest to the smallest in decreasing order, the POD modes are arranged in the order of importance in terms of capturing the kinetic energy of the flow field.

4. In a last step the temporal coefficients $a_k(t)$ are calculated using the dot product :

$$a_k(t) = \langle \boldsymbol{U^T}, \boldsymbol{\Phi_k}(\boldsymbol{x}) \rangle \tag{3.33}$$

3.3.5.2 Computational cost

As described in the previous section, the data sets involved in the present case are huge and, in the context of POD, lead to matrices with several billion entries. It is therefore important that the implementation of the calculation steps described above is carried out in an efficient manner in order to keep the calculation times and the memory load as low as possible.

In the present work this was realized by means of a python implementation, which is fundamentally based on the libraries SCIPY and NUMPY, whereby an efficient parallel computation of e.g. matrix multiplication or eigenvalue determination is facilitated. All POD calculations were performed on a workstation with 24 physical CPU cores and 256 GB of RAM.

Figure 3.15 illustrates the percentage of the total program duration accounted for by the calculation steps described above. Here, the total runtime of the program is approx. 120 s, not including the loading of the raw data and the saving of the solution.

It is noticeable that solving the eigenvalue problem, which is mathematically the most time-consuming procedure, takes only about 3% of the total runtime. This is achieved by the application of the method of snapshots, which reduces the dimension of the correlation matrix to $m \times m$ and thus reduces the effort of solving the eigenvalue problem by orders of magnitude.

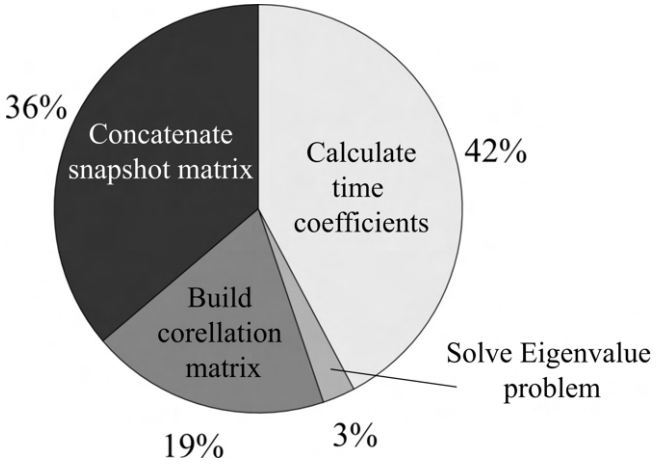

Figure 3.15: Pie chart of the total runtime percentage accounted for by the individual program sections.

Much more time-consuming are the matrix multiplications which have to be performed for the calculation of the correlation matrix and the time coefficients. In both cases, about 32.6×10^{12} computational operations (multiplications and additions) have to be performed for this calculation, which is why the two steps require more than 60% of the total computation time.

One third of the calculation time is required for the creation of the snapshot matrix, whereby not only the lining up of the vectors was accounted for, but also the calculation of the time average and the subsequent calculation of the fluctuation values of the individual velocity components.

In summary, due to the application of the method of snapshots and an efficient parallel calculation of the computationally intensive operations, the total computation time of 2 min is very low and thus cannot be considered as a limiting factor in this case even on a workstation with less CPU power. It is rather the memory, which is to be regarded as critical due to the large matrices which caused a peak loading of over 100GB.

4 Results

This chapter contains the discussion of the results obtained using the evaluation methods explained in section 3.3 and the numerical model described in chapter 3.2. The chapter is divided into four sections, namely time-averaged analysis, time-exact analysis, frequency domain analysis and modal analysis. Verification of the numerical predictions against experimental data is not carried out in a separate section, but is included at the appropriate points.

4.1 Operating points under investigation

A total of four operating points were investigated within this work. The Reynolds number is kept the same for all operating points at Re=200,000, so that the various simulations only differ in the character of the inflow into the stator grid.

An unperturbed ("*clean*") inflow was considered as a reference, i.e. without periodically incoming wakes and without free stream turbulence (laminar inlet). This operating point will be referred to as OP-CL in the following.

In order to quantify the influence of the free stream turbulence, a calculation was also carried out with synthetically generated turbulence at the inlet, whereby also in this case no periodic wakes were taken into account. This operating point will be referred to as OP-CT in the following.

For the wake perturbed operating points, two different rotational speeds were considered (60 rpm & 180 rpm), which are representative of a low disturbance frequency case (OP-W60) e.g. low Strouhal number with a high flow coefficient and a high disturbance frequency case (OP-W180) e.g. high Strouhal number with a low flow coefficient. Both simulations were performed with synthetic turbulence.

It should be noted that in the following sections the focus will be essentially on the three operating points with free stream turbulence (FST) (OP-CT, OP-W60 and OP-W180). For the sake of clarity, the operating point with laminar inflow (OP-CL), which serves as a reference case, is only used at some selected points to quantify the influence of the FST.

The basic parameters are summarized in Table 4.1.

Table 4.1: Summary of the main parameters for the operating points under consideration.

Operating point	Free stream turbulence	Strouhal number	Flow coefficient
OP-CL	✗	-	-
OP-CT	✓	-	-
OP-W60	✓	0.54	2.4
OP-W180	✓	1.61	0.8

4.2 LES quality assessment

As described in section 3.2.1.2, at least 80% of the turbulent energy spectrum must be resolved by the numerical mesh in order to obtain a valid LES. To estimate this a priori, several assumptions had to be made, which were based on a simplified "model spectrum" for isotropic turbulence. At this point it is now to be checked which part of the total turbulent energy is actually directly resolved and which part is modeled by the SGS model.

For this it is reasonable to employ the following equation:

$$E_{\text{resolved}} = \frac{k_{\text{resolved}}}{k_{\text{resolved}} + k_{\text{sgs}}}, \tag{4.1}$$

where k_{resolved} can simply be calculated based on the rms values gathered from the unsteady statistics according to Eq. (2.17).

As described above, the kinetic energy of the subgrid modes k_{sgs} is not directly modeled in the present simulations and thus has to be estimated based on the relation:

$$k_{\text{sgs}} = \frac{\nu_{\text{sgs}}}{C_m \hat{\Delta}}, \tag{4.2}$$

with the model constant $C_m = C_w = 0.325$ [5].

Since k_{resolved} is a statistic based value, it is obvious to determine statistics for the other values as well. For this purpose, the three variables occurring in Eq. (4.1) are defined a priori as so-called custom field functions in order to be able to collect their statistics during the simulation.

The distribution of the resolved energy spectrum E_{resolved} is shown in Fig. 4.1 for an arbitrary snapshot (top left) and for the time mean representation (bottom right) along a blade to blade (B2B) section at 50% spanwise position. The illustration shows the OP-W-180 operating point, as it is considered most

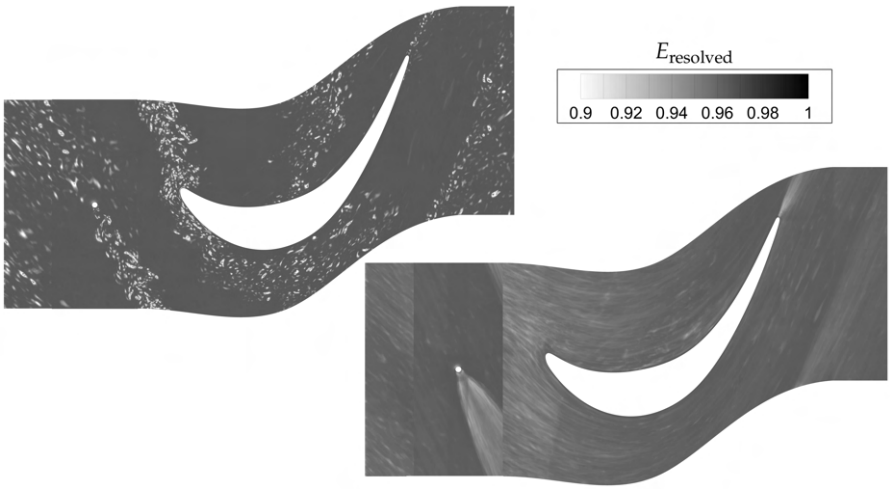

Figure 4.1: Distribution of the resolved part of the turbulent energy spectrum E_{resolved} in a B2B section at 50% spanwise position. Snapshot representation (top left). Time mean representation (bottom right).

critical with regard to the vortical structures inside the wake of the rotating bar.

It is clearly visible that in a large part of the numerical domain more than 90% of the turbulent energy spectrum is resolved. Therefore, the scale resolving simulations presented in this thesis can be considered as highly resolved LES.

4.3 Time mean evaluation

This section deals with the evaluation of transient statistics and serves to give a basic impression of the flow conditions in the vicinity of the blade surface and the boundary layer condition. A further aspect is the verification of the numerical data against the experimental measurements.

4.3.1 2-dimensional flow field

The flow structure in the vicinity of the blade's trailing edge will be analyzed within this section. For this purpose, the time mean velocity field inside the

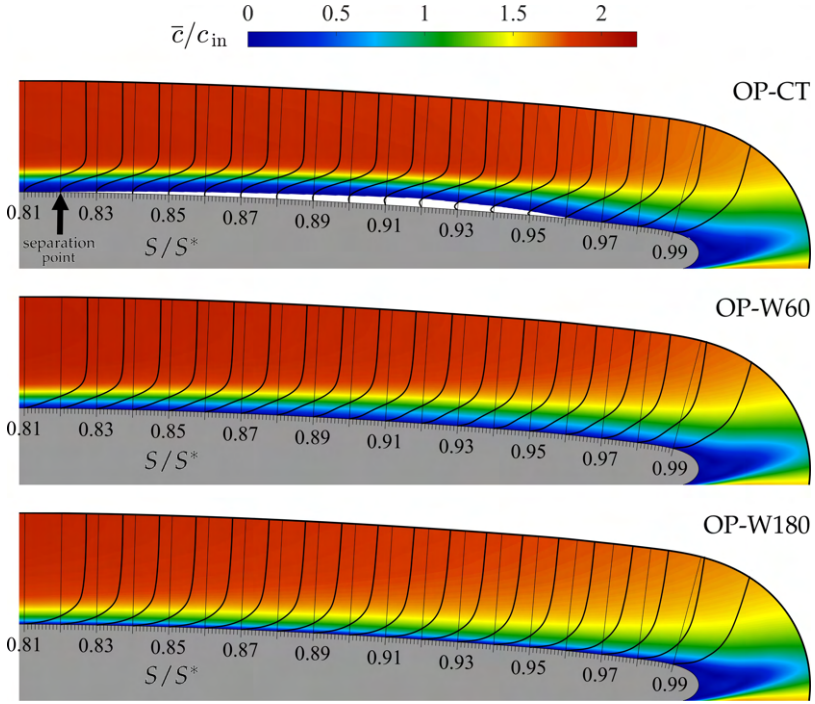

Figure 4.2: Distribution of the time mean non-dimensional velocity $\overline{c}/c_{\text{in}}$ at mid-span position of the blade for three different operating points (top: OP-CT, mid: OP-W60, bottom:OP-W180). Profiles representing the tangential velocity component are superimposed as black curves.

evaluation plane O-GRID is shown in Fig. 4.2 for three operating conditions under investigation. Profiles of the tangential component of the velocity vector are overlaid as black lines on the contour plot.

For the case without wake disturbance (OP-CT) the back-flow region inside the laminar separation bubble is indicated by blanked values. Apparently it is a closed separation bubble, which extends between the separation point $S_s/S^* \approx 0.82$ (black arrow) and the reattachment point $S_r/S^* \approx 0.97$ based on the time averaged velocity field.

It can be seen, that the boundary layer profiles upstream of the separation bubble exhibit a shape typical of laminar boundary layers, which turns inflectional as the boundary layer separates from the blade surface. Whether

a complete transition to the turbulent state takes place within the detached shear layer and whether the boundary layer is completely turbulent after reattachment cannot be clearly determined at this point.

For the two perturbed cases no separation bubble can be identified on the basis of the time-averaged field. However, it should be noted that this does not necessarily imply that the flow does not detach intermittently from the blade surface between two wake impacts, as will be further investigated in the following sections.

In comparison to the unperturbed case, the boundary layer profiles are much more "bulbous" for the perturbed operating points and are therefore more similar in shape to a typical turbulent boundary layer profile. This effect is much more pronounced at higher Strouhal numbers (OP-W180) than at lower ones (OP-W60). Here again, this does not necessarily mean that the boundary layer is fully turbulent at all times, so that more detailed considerations become necessary, which will be described in detail in the following sections of this thesis.

4.3.2 Boundary layer analysis

This section deals with the analysis of the boundary layer development along the suction-side trailing edge of the blade on the basis of the time-averaged velocity fields. In order to provide a reference, the unperturbed case (OP-CT) is considered first, with the characterization of the separation bubble being one of the main aspects.

4.3.2.1 Reference operating point (OP-CT)

Figure 4.3 (top) shows the distribution of the velocity rms value in the area of the blade's trailing edge (suction side) for the reference operating point OP-CT. To get an impression of the dimensions within the near-wall flow, the edge of shear layer, the inflection line and the line of zero tangential velocity are indicated.

Along the inflection line there is a clear band of increased rms values. These fluctuations increase significantly along the separation bubble, indicating the presence of the inflectional Kelvin-Helmholtz instability, which is inviscid by nature and is mainly responsible for the laminar to turbulent transition of the separated shear layer. The fact that the maximum rms values in the area of the inflection line still increase after the flow has been reattached to the

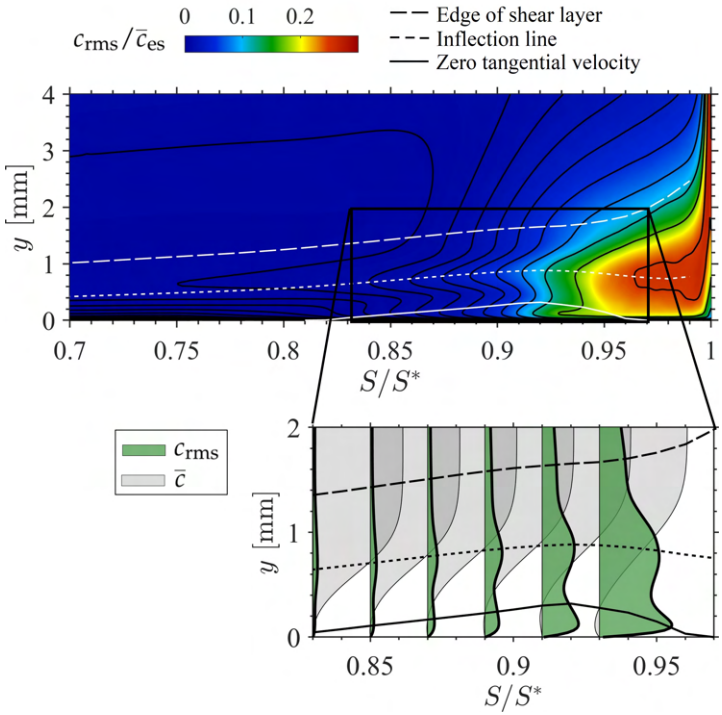

Figure 4.3: Distribution of rms velocity near the blade's suction side trailing edge for the unperturbed case OP-CT (wall-normal coordinate stretched for clarity) (top), and zoom of the qualitative velocity profiles near the reattachment point (bottom).

blade surface indicates that the transition of the shear layer is not completely finished at this point, i.e. it is not a fully turbulent reattachment process.

However, also within the separation bubble, areas of increased fluctuations can be identified in the near wall region, which is further illustrated in the bottom part of Fig. 4.3 using qualitative wall normal profiles of the rms velocity (green profiles).

According to *Rist and Maucher* [102] and *McAuliffe and Yaras* [77], this can be attributed to a viscous Reynolds number dependent inner instability, which is strongly influenced by the degree of back-flow inside the laminar separation bubble, which is also evident in the velocity profiles (grey profiles) presented in the close up. The boundary layer transition in this case can thus

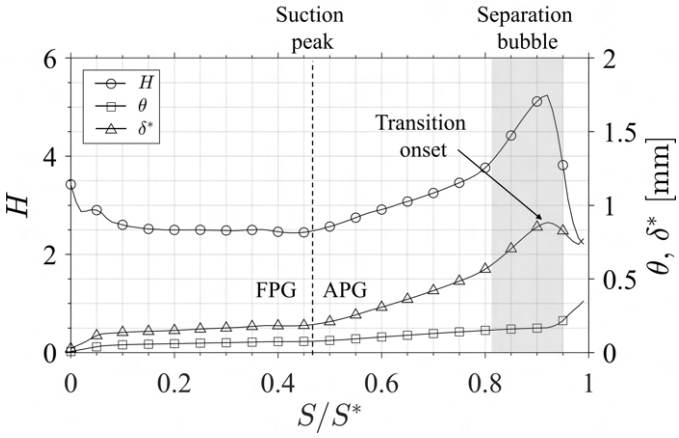

Figure 4.4: Development of boundary layer parameters along the suction surface of the investigated stator profile at operating point OP-CT.

be considered as taking place via a so-called multi mode transition (cf. [77]), which is to be examined in more detail in the following sections.

In order to better evaluate the boundary layer condition, the shape factor H_{12} (Eq. (2.6)) along the suction side is shown in Fig. 4.4, which describes the flow development and structural reordering of the boundary layer during laminar-turbulent transition. Since this factor is derived from the momentum thickness θ and the displacement thickness δ^*, their progressions are also shown.

In the front part of the blade, which is mainly characterized by an acceleration of the flow and a subsequently favorable pressure gradient (FPG), the shape factor remains almost constant, which is attributable to the parallel course of the displacement thickness and the momentum thickness. Here the value $H \approx 2.5$ approximates the Blasius solution for laminar boundary layers (cf. section 2.2.1), meaning that there is a stable laminar boundary layer in this region of the profile.

Behind the suction peak of the profile, a weakening of the boundary layer takes place caused by the adverse pressure gradient (APG), which results in a linear increase of the shape factor. This is mainly caused by the increase of the displacement thickness due to the successive deceleration and the associated thickening of the boundary layer profile.

In the area of the separation point $S_s/S^* = 0.82$, the shape factor is approx. $H \approx 3.9$, and rises even steeper within the separation area, which is caused by unrealistically high values of the displacement thickness in case of separated flows, as *Hourmouziadis* [45] describes.

As *Hatman and Wang* [38] state, the transition onset within the detached shear layer is indicated at the point of maximum displacement ($S_{xmd}/S^* \approx 0.92$). It is followed by a drastic drop of the shape factor, which is caused by the reduction of the displacement thickness as a consequence of the reduction of the height of the separation bubble. This effect is intensified by the growing momentum thickness θ, which is caused by the increased momentum exchange inside the shear layer as it enters the turbulent state. It seems likely that this effect is significantly influenced by the inner instability in the aft portion of the laminar separation bubble described above, which will be discussed in more detail in the following chapters.

In the area around the reattachment point $S_r/S^* = 0.97$ the form factor further decreases to around $H \approx 3$, which is also an indication of a non fully turbulent reattachment of the separated shear layer as a further decrease is observable towards the trailing edge of the stator blade, indicating an ongoing transition process.

According to *Hatman and Wang* [38] a comprehensive classification of the laminar separation bubble can be carried out, which is mainly based on empirical correlations of boundary layer parameters. They distinguish three separated flow transition modes, which they defined as a *transitional separation mode*, where transition occurs before the point of separation, a *laminar separation short mode*, and a *laminar separation long mode*, where transition happens in both cases inside the separated shear layer. They further found that the dominance of one type of instability over the other (Tollmien-Schlichting or Kelvin-Helmholtz) determines the type of separation bubble. [42]

First of all the separation Reynolds number based on the momentum thickness θ has to be evaluated, which is a common measure for the classification of separation bubbles. For the present case it yields:

$$\mathrm{Re}_{\theta s} = \frac{\overline{U}_{es}\theta_s}{\nu} \approx 312, \tag{4.3}$$

with the time mean boundary layer edge velocity magnitude at separation $\overline{U}_{es}$.

According to *Hatman and Wang* [38], the laminar separation bubble can thus be classified as falling under the short bubble regime in the present case. This is to be expected as LPT blades most likely experience short separation

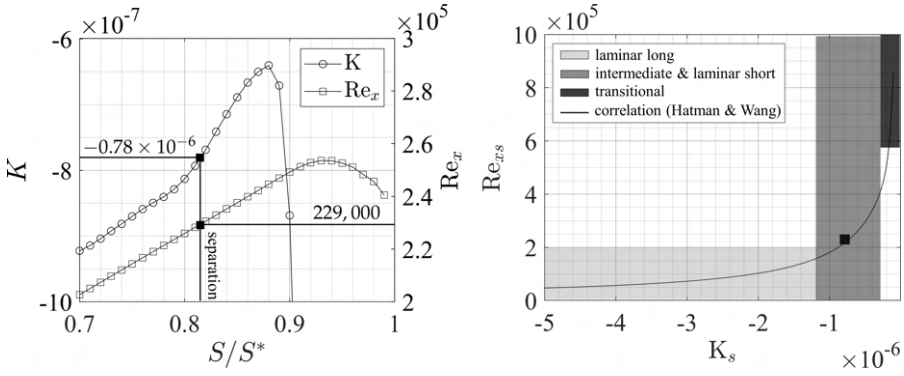

Figure 4.5: Course of the acceleration parameter K and the local Reynolds number Re_x along the suction surface for operating point OP-CT (left), and comparison with the correlation after *Hatman and Wang* [38] (right).

bubbles under most operating conditions ($10^5 < \mathrm{Re} < 4 \times 10^5$), as it is stated by *Hodson and Howell* [42].

The plausibility of the structure of the separation bubble predicted by the LES can be further verified by evaluating the acceleration parameter

$$K = (\nu/\overline{U}_e^2)(\mathrm{d}\overline{U}_e/\mathrm{d}S) \tag{4.4}$$

and the local Reynolds number

$$\mathrm{Re}_x = \overline{U}_e S/\nu \tag{4.5}$$

(their progression is presented in Fig. 4.5 (left)) within the separation point and comparing them with a correlation presented by *Hatman and Wang* [38]. The results show a very good agreement (Fig. 4.5 (right)) and confirm that the laminar separation bubble is part of the short bubble/intermediate regime.

A comparison of the Reynolds numbers at maximum displacement $\mathrm{Re}_{x\mathrm{md}}$ and reattachment Re_{xr} with the empirical correlations also given by *Hatman and Wang* [38] is shown in Fig. 4.6 and also demonstrates very good agreement.

It can therefore be concluded that the structure of the laminar separation bubble predicted by the LES in the present case corresponds to the structures known from the literature regarding flat plate experiments, which can be clearly described by means of empirical correlations. Thus on the one hand

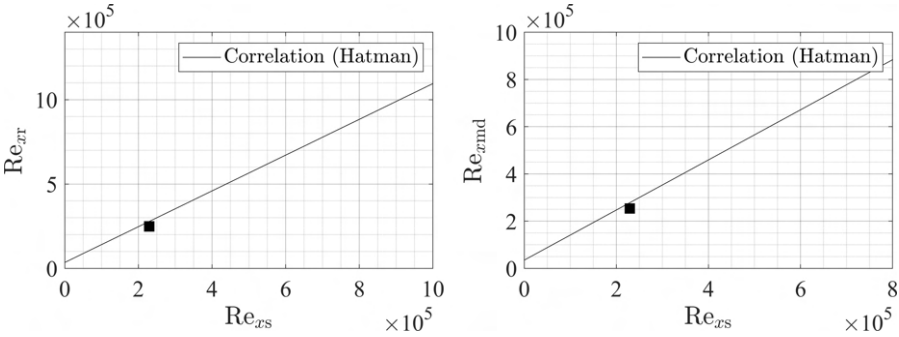

Figure 4.6: Correlation between reattachment Reynolds number Re_{xr} and separation Reynolds number Re_{xs} (left) and between Reynolds number at maximum displacement $\mathrm{Re}_{\mathrm{xmd}}$ and separation Reynolds number Re_{xs} (right).

a verification of the simulation results and on the other hand a verification of the evaluation methods (boundary layer integration) is achieved. Basic parameters describing the laminar separation bubble for the OP-CT case are summarized in Table 4.2.

For the unperturbed reference case OP-CT transition thus takes place within the detached shear layer via a closed short laminar separation bubble. Although all the analyses shown up to this point confirm the reattachment of the flow to the blade surface and also the onset of the transition within the detached shear layer, the course of the shape factor H does not indicate a fully developed turbulent boundary layer in the region downstream of the reattachment point S_r, as this would be associated with a constant shape factor and a flattening of the streamwise gradient of θ (cf. [21, 67, 86]). This

Table 4.2: Summary of the main parameters for the laminar separation bubble for the OP-CT operating point.

Separation point	S_s/S^*	0.82
Transition onset	S_t/S^*	0.92
Reattachment point	S_r/S^*	0.97
Separation conditions:		
Reynolds number	Re_{xs}	229,000
Momentum thickness Reynolds number	$\mathrm{Re}_{\theta\mathrm{s}}$	312
Shape factor	H_{12}	3.9
Acceleration parameter	$K_\mathrm{s} \times 10^{-6}$	-0.78

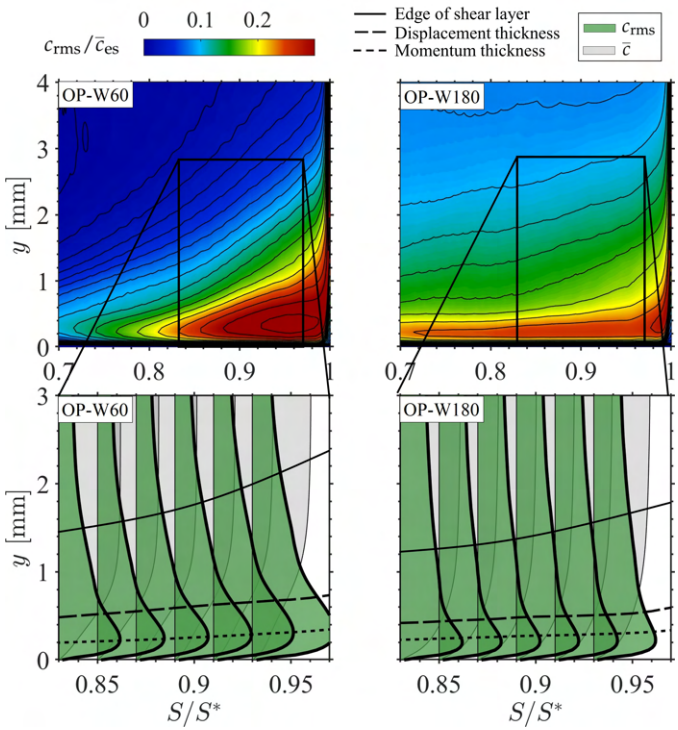

Figure 4.7: Distribution of rms velocity near the blade's suction side trailing edge for both perturbed cases (OP-W60 top left/OP-W180 top right) (wall-normal coordinate stretched for clarity), and boundary layer properties along the suction surface (OP-W60 bottom left/OP-W180 bottom right).

is inline with the findings of *McAuliffe and Yaras* [77] who reported that in their studies regarding flat plate boundary layer transition with comparable bubble structure and FSTI, a complete turbulent boundary layer was completed only about 50% of the bubble length downstream of the reattachment point.

4.3.2.2 Perturbed operating points (OP-W60 & OP-W180)

For the two perturbed cases the distributions of rms velocity are shown in Fig. 4.7 (top row). It should be noted that the y-axis scaling has been adjusted compared to Fig. 4.3 to provide a better impression.

It can be clearly seen that the fluctuation values for the case of a high Strouhal number (OP-W180, right) in the area away from the wall are significantly higher than in the case of a low Strouhal number. As expected, this is due to the higher turbulent energy within the wakes generated by the wake generator.

In the area close to the wall, however, the picture is different. Here the fluctuations for the case of low Strouhal number (OP-W60, left) are much higher especially near the trailing edge of the blade. Although it is not yet possible to make a clear statement on the basis of the results shown so far, it is reasonable to assume that this phenomenon may be attributed to the fact that the energy transferred to the boundary layer by the wake in the OP-W60 is not sufficient to achieve a continuous attached flow at the prevailing interaction frequency. This in turn leads to a periodic separation and re-attachment of the boundary layer which causes a thickening of the time mean boundary layer and momentum thickness (left bottom), which will be analyzed more closely in the following chapters.

For the OP-W180 the above described behavior is not apparent, as due to the higher TKE level the wakes are able to energize the boundary layer far more upstream (higher fluctuation levels upstream $S = 0.8$ compared to OP-W60, cf. Fig. 4.7). In this case it seems reasonable that a periodic flow separation is completely suppressed even between the direct wake impacts (effect of calmed regions).

To further get a quantitative impression of the boundary layer state a comparison of the shape factor for all three operating points is shown in Fig. 4.8. The almost identical course of all three curves in the front area of the blade confirms that the laminar boundary layer which is stabilized by the FPG is not affected by the periodically incoming wakes before reaching the suction peak, as it was firstly stated by *Halstead et al.* [34]. However, it is important to note that this does not mean that no instabilities within the boundary layer are introduced by the external disturbances, which are difficult to detect in this time-averaged global view.

Downstream of the suction peak, both perturbed cases initially show a slight increase in the shape factor H due to the APG and the resulting destabilization of the boundary layer (increasing displacement thickness), although it is not as steep as in the case of unperturbed inflow.

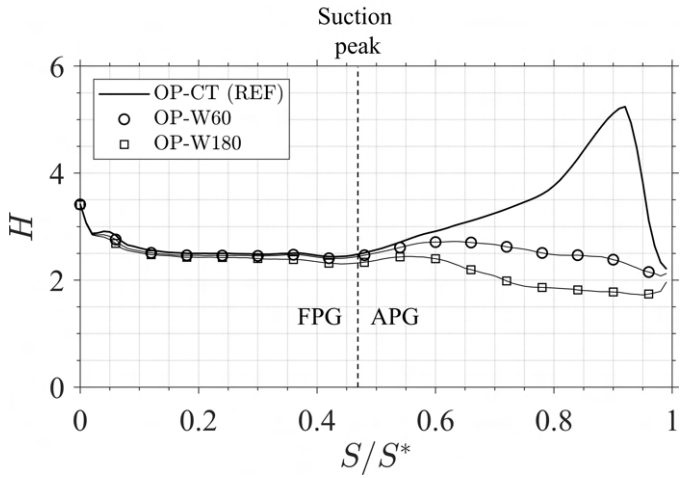

Figure 4.8: Development of the shape factor H along the suction surface of the investigated stator profile at different operating points.

In the case of high Strouhal number (OP-W180), the increased energy transfer to the boundary layer provides for an increased impulse exchange, which is indicated by an increase in momentum thickness. The resulting drop of the shape factor therefore occurs much earlier compared to the OP-W60, although it does not fall below H<1.4. This would indicate a completely turbulent boundary layer, which is caused by the periodic change between laminar, transitional and turbulent boundary layer states and will be discussed in more detail below.

4.3.3 Wall shear stress distribution

This section involves the analysis of the distribution of wall shear stress in the mid-span section of the investigated stator blade. In addition to the previously presented analyses, the wall shear stress provides a further possibility to draw conclusions regarding the boundary layer state. Furthermore it provides a means to verify the numerical predictions based on the experimental data.

For this purpose, the time mean quasi wall shear stresses (QWSS), measured using surface flush hot film arrays, are compared with the numerical data for all three operating points considered.

It should be noted that hot film arrays ideally reflect the tangential component of the QWSS, but this may not be fully accurate as cross components within the flow may influence the results. Furthermore, this measurement method is not able to detect negative values of the QWSS, so that the instantaneous values of the measurement only reflect the absolute value. This must be taken into account when averaging the numerical data over time so that the mean value in this case is given by

$$\overline{\tau}_{\mathrm{w}} = \frac{1}{N} \sum_{i=1}^{N} \left| \tau_{\mathrm{w}}(t_i) \right| . \tag{4.6}$$

The fact that this averaging does not correspond to the true average value must be taken into account when evaluating the results.

The distribution for the OP-CT case is shown in Fig. 4.9 (top) together with the laminar inflow OP-CL case. The left side of the figure corresponds to the pressure side, while the right side corresponds to the suction side of the blade surface. The leading edge of the blade is at position 0 and the trailing edge at position -1/1.

A comparison of the data shows an excellent agreement between CFD and experiment. The area of largest deviation is found in the suction side area upstream of the suction peak. The two measured values are clearly below the curves of the LES, which is most likely due to measurement errors (e.g. incorrect calibration of the zero voltages), since these outliers are not typical for the T106 wall shear stress distribution and cannot be found anywhere in the literature (cf. *Michelassi et al.* [81], *Sandberg et al.* [107]).

Nevertheless, the more important reduction of the wall shear stress due to the APG downstream of the suction peak is matched very well by both simulations and also the position of the separation point is in good agreement with the experimental data in both cases.

The influence of turbulence is only clearly visible in the area of the laminar separation bubble. It is evident that the simulation with laminar inflow predicts a too late onset of the transition within the detached shear layer, which results in a too large expansion of the laminar separation bubble and thus a delayed increase of the wall shear stress, which is in line with the findings of other researchers [7, 48, 56, 59, 60, 85, 121].

For the cases with wake disturbance shown in Fig. 4.9 (bottom). Again, the agreement between the numerical predictions and the experimentally measured data is excellent with minor deviations in the rear suction side region.

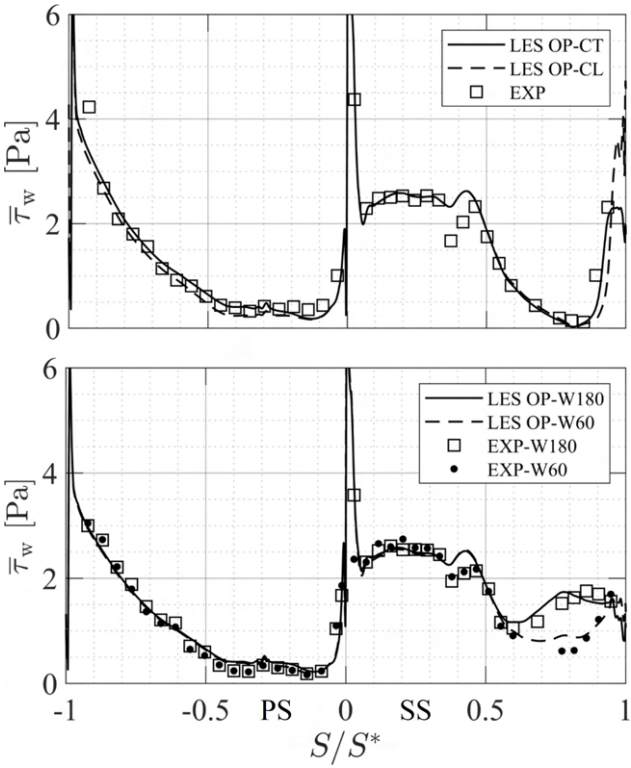

Figure 4.9: Distribution of time mean wall shear stress $\overline{\tau}_w$ at midspan of the investigated stator blade for OP-CT/L (top), and for the perturbed operating points OP-W60/180 (bottom).

The wall shear stress on the pressure side as well as in the front area of the suction side is almost identical to the unperturbed cases, which was to be expected in view of the previously shown course of the form factor. The wake influence only becomes apparent downstream of the suction peak at approx. $S/S^* > 0.6$. In both cases, the drop of the average wall shear stress to zero is prevented and thus a permanent flow separation is suppressed, which, again, does not imply, that intermittent flow separations may not occur.

In the case of a high Strouhal number, the wall shear stress doubles downstream of $S/S^* > 0.6$ compared to the case of a low Strouhal number, which is due to the higher turbulent fluctuations within the wake and the associated energy transfer. Furthermore, the flow at low Strouhal numbers has more time to change between two wake impacts into a laminar boundary

layer state with low wall shear stress due to the lower disturbance frequency, which is reflected in a reduction of the time mean value.

Interesting to note is the increase in mean wall shear stress near the trailing edge of the profile in the case of low Stouhal number (OP-W60). This behavior is in line with the phenomenon of increased rms-velocity near the trailing edge shown in Fig. 4.7 (left) and can be attributed to the intermittent increase in wall friction due to transitional effects in between two consecutive wake impacts, as will be shown in the following sections.

4.3.4 Analysis of turbulence states

This section covers the analysis of turbulence states according to the theory of *Lumley and Newman* [66] described in section 3.3.3. As in the previous sections, this analysis is based on time-averaged data sets, so that a strong mixing of different turbulence states can be expected in case of the wake disturbed operating points, which makes an exact evaluation difficult. Nevertheless, interesting tendencies can be derived from these observations, which in combination with the previously presented analyses allow a more comprehensive illustration of the flow conditions in the area of the blade trailing edge.

4.3.4.1 Reference operating point (OP-CT)

Figure 4.10 (left) shows the distribution of the *componentality contours* according to *Emory and Iaccarino* [24] for the OP-CT case in the area of the suction side trailing edge of the profile. Horizontal profiles are representing the qualitative course of the rms-value of the absolute velocity c_{rms}. To get an impression of the dimensions within the near-wall flow, the edge of shear layer, the line of zero tangential velocity as well as the momentum thickness θ and the displacement thickness δ^* are indicated. It has to be noted, that in the underlying case the course of the momentum thickness is almost identical to that of the inflection line.

At first glance, the illustration provides a clear separation of the near-wall area into regions of different turbulence states, which basically correspond to the plotted courses of the boundary layer parameters.

The onset of the transition (cf. section 4.3.2) within the detached shear layer is indicated in the area of maximum displacement thickness ($0.9 < S/S^* < 0.93$) by a change of the turbulence state from the 1-component (red area, region (A)) to the axisymmetric rod-like shape (purple area, region (B)). This

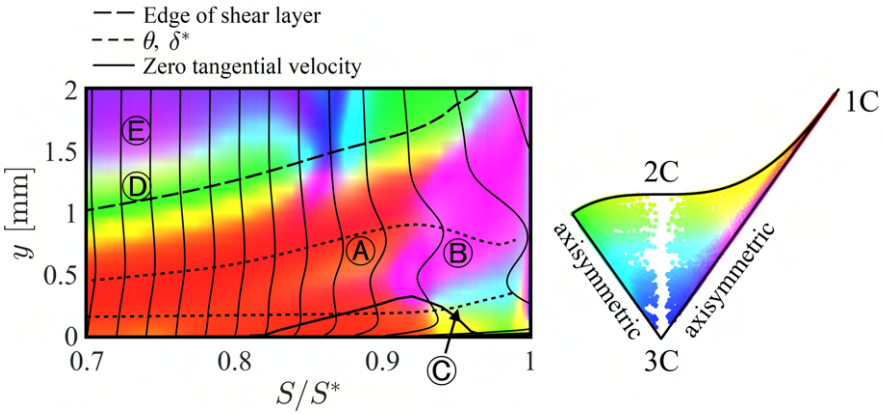

Figure 4.10: Illustration of the turbulence states for OP-CT (according to the theory of *Lumley and Newman* [66]) using the method of componentality contours after *Emory and Iaccarino* [24] (wall-normal coordinate stretched for clarity) (left) and anisotropy invariant map for every data point (right).

confirms the prior assumptions of KH-instability driven shear layer transition along the inflection line. It is interesting to note that the transition onset shifts downstream with increasing wall distance, so that the furthest upstream position of the onset is in the zero tangential velocity line region, suggesting that the origin of the transition is also located in this region.

Downstream of the separation bubble a region of 2C shaped axisymmetric turbulence follows, which can be identified by the light blue and green/yellow areas (region (C)). Whether these regions might be attributed to the viscous near wall instability described by *McAuliffe and Yaras* [77] has to be further analyzed in the following, as well as the interaction of these areas in the process of ongoing transition of the separated shear layer.

Along the edge of shear layer there is another area (region (D)) which is characterized by 2C turbulence (green/yellow), which acts as a transition layer between the almost isotropic (blue) turbulence of the free stream (region (E)) and the 1C turbulence inside the boundary layer.

4.3.4.2 Perturbed operating points (OP-W60/OP-W180)

The contours of the two perturbed cases are shown in Fig. 4.11 (y-axes are scaled for a better impression). The distributions are clearly different com-

pared to the unperturbed case. In the case of a high Strouhal number (OP-W180), an almost horizontally layered distribution between the areas of different turbulent states is evident. The isotropic area of the free flow (region (A)) is divided by a very broad area of axisymmetric turbulence (light blue, region (B)) outside the edge of the shear layer from the inner area of the boundary layer. Within the boundary layer, a layer of 2C turbulence (green/yellow, region (C)) is found above the displacement thickness, while the turbulence below the displacement thickness is characterized by 1C turbulence (red, region (D)). The purple region, which previously marked the transitional region in Fig. 4.11, is confined to a small region near the trailing edge (region (E)) in this case of high Strouhal number, indicating that the present case is not characterized by instability-driven transition mechanisms.

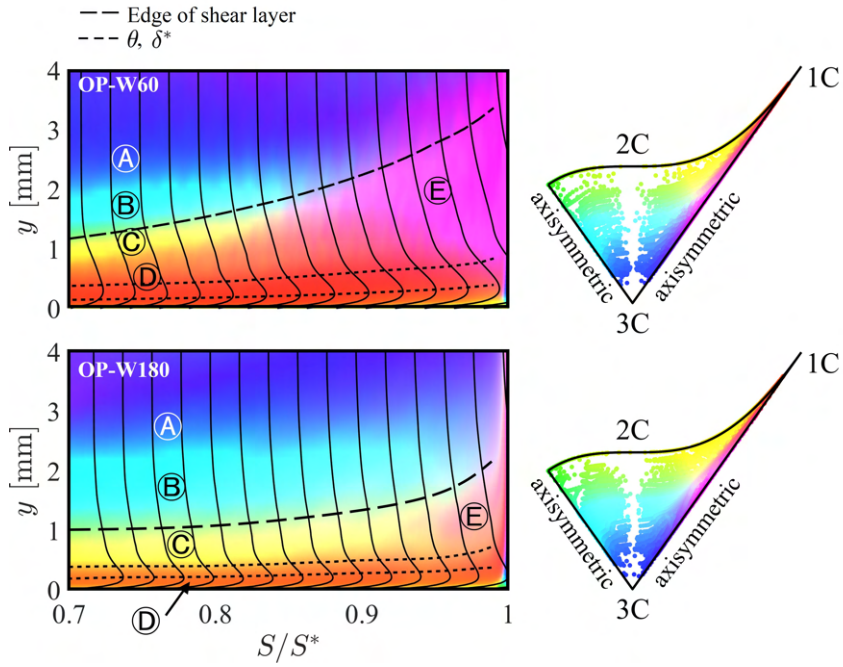

Figure 4.11: Illustration of the turbulence states for OP-W60 (top) and OP-W180 (bottom) (according to the theory of *Lumley and Newman* [66]) using the method of componentality contours after *Emory and Iaccarino* [24] (wall-normal coordinate stretched for clarity) (left) and anisotropy invariant map for every data point (right).

For the low Strouhal number case (OP-W60) the picture is different. Here, an additional large region of axisymmetric turbulence (purple) spreads below the edge of shear layer along the rear portion of the blade. As in Fig. 4.10 this is an indication for an ongoing transition process of the boundary layer, which is not directly induced by the incoming wakes, but intermittently triggered by instability mechanisms. A closer look into these phenomena is presented in the unsteady consideration illustrated in the following sections.

In the two perturbed cases the majority of turbulence kinetic energy is produced very near the wall (along the line representing the momentum thickness), indicated by the regions of maximum rms-velocity (cf. Fig. 4.7), which are qualitatively represented by the vertical profiles. As this behavior is similar to equilibrium turbulent boundary layers it indicates an at least intermittently turbulent boundary layer state.

In the unperturbed case the majority of turbulence kinetic energy is produced in the range of the displacement thickness (cf. Fig. 4.3) and is a consequence of shear layer instabilities (KH-instabilities) and the generation of large scale vortical structures (KH-rolls) shed from the separation bubble (cf. *McAuliffe and Yaras* [77]), which will be analyzed more closely in the following sections.

4.3.5 Summary

In summary it can be concluded that with the help of the above presented analyses based on the time mean flow field a detailed description of the global flow structures and flow states could be established based on the verified numerical predictions. By comparing the boundary layer parameters for the unperturbed cases with correlations known from the literature concerning flat plate flows, excellent agreement was found, proving the transferability of these correlations to more complex configurations as in the underlying case and also the validity of the underlying CFD predictions.

The 2-dimensional analysis of the turbulence states, which to the author's knowledge has not been performed elsewhere in the literature in this context, provided a spatial impression of the flow fields for the three operating points studied and allowed visualization of the different regions involved in the detached shear layer transition, showing similar extensions to the theoretical descriptions known from the literature. Especially the visual evidence of the near wall instability region is an interesting finding, which supports current theories of different research groups [7, 77] regarding the course of separated shear layer transition.

However, it must be mentioned at this point that for the two perturbed operating points the analysis of the flow field on the basis of time averaged values is quite complicated as intermittent flow features like wake affected boundary layer transition or intermittent flow separation become blurred by the global time averaging. The time averaged velocity field, for example, initially indicated a complete suppression of laminar flow separation, while a closer analysis of the fluctuation values as well as the boundary layer parameters indicate that a periodic flow separation might exist in the case of a low Strouhal number (OP-W60). In these cases it is therefore inevitable to carry out additional detailed time-exact investigations, whereby the intermittent character of the flow can be completely described and a detailed analysis of the spatial development of boundary layer instabilities in the time and frequency domain can be carried out.

4.4 Time domain evaluation

This section deals with the time domain analysis of the transient data, which aims to obtain a temporal description of the transition phenomena that will allow a separation of the different mechanisms involved. Besides a detailed knowledge of the temporal relationships in the reference case, i.e. without perturbed inflow, the focus is especially on the identification of the wake influence on the transition mechanisms and the resulting intermittent boundary layer evolution.

To ensure this, an analysis of the wake kinematics for the two wake disturbed operating points is presented in a first step. In a second step the transient boundary layer behavior is analyzed by means of time-space representations of wall shear stress and shape factor and visualized by means of 3-dimensional representations of the Q-criterion.

4.4.1 Wake kinematics

The wake kinematics describe the change of the structure of the incoming wakes while they are convected with the flow throughout the blade passage. Due to the different flow conditions, very different kinematic phenomena occur at the two operating points under investigation, which will be discussed in the following.

The wake kinematics are illustrated in Fig. 4.12 and 4.13 for both operating points, based on the distribution of the phase-averaged fluctuating velocity

$$\left\langle c' \right\rangle (x, \theta, t) = \langle c \rangle (x, \theta, t) - \overline{c}(x, \theta) \tag{4.7}$$

at four equally distributed time steps per bar passing.

On first glance, the much flatter wake angle in the case of low Strouhal number (OP-W60) is evident, which results from the lower circumferential speed of the rotating bars. As a result, the base point (A) of the wake enters the blade passage much faster (B) and is accelerated, causing the wake to bend towards the suction side (C) of the neighboring blade. The blocking of the passage by the wake causes a cell of increased velocity (D) near the suction side, which is pushed in front of the wake along the suction side in the direction of the trailing edge and forms a spanwise running vortex (E) upstream the wake's leading edge. Together with the counter-rotating vortex (F) downstream of the wake, both vortices are pushed towards the trailing edge as the wake flaps down onto the blade surface (G). This flapping causes a quick evacuation of the accelerated near wall cell towards the trailing edge, which will be of particular relevance in the following considerations.

In summary, it can be said that the flow in the area of the blade's suction-side trailing edge experiences a brief acceleration due to the quick evacuation of the wake's leading edge vortical structure ($t/\tau_{60} \approx 3/4$), which is followed by a prolonged deceleration of the flow ($0 \lessapprox t/\tau_{60} \lessapprox 1/4$) as a direct consequence of the wake beeing flushed down the suction side surface.

In the case of a high Strouhal number (OP-W180), the wake kinematics show a completely different picture, which is basically attributable to the steeper wake angle and the higher circumferential speed of the rotating bars. After the wake base point (A) enters the blade passage, due to the high speed of the wake generator it does not have as much time to be convected into the passage, so that after the wake reaches the neighboring blade at $t/\tau_{180} = 3/4$ (B) a clearly recognizable wake front is formed in pitch direction (C - orange curve).

Similar to the previously described case of low Strouhal number, two distinct spanwisely running counter rotating vortices (D+E) form upstream and downstream of the wake front, which are convected with the wake along the blade passage towards the trailing edge. Between these vortices, fluid from the PS of the adjacent blade is transported toward the SS, often referred to as the "negative jet effect".

As the vortex pair is convected downstream, it is increasingly deformed (F+G) and intensified, so that in the area of the trailing edge two fast suc-

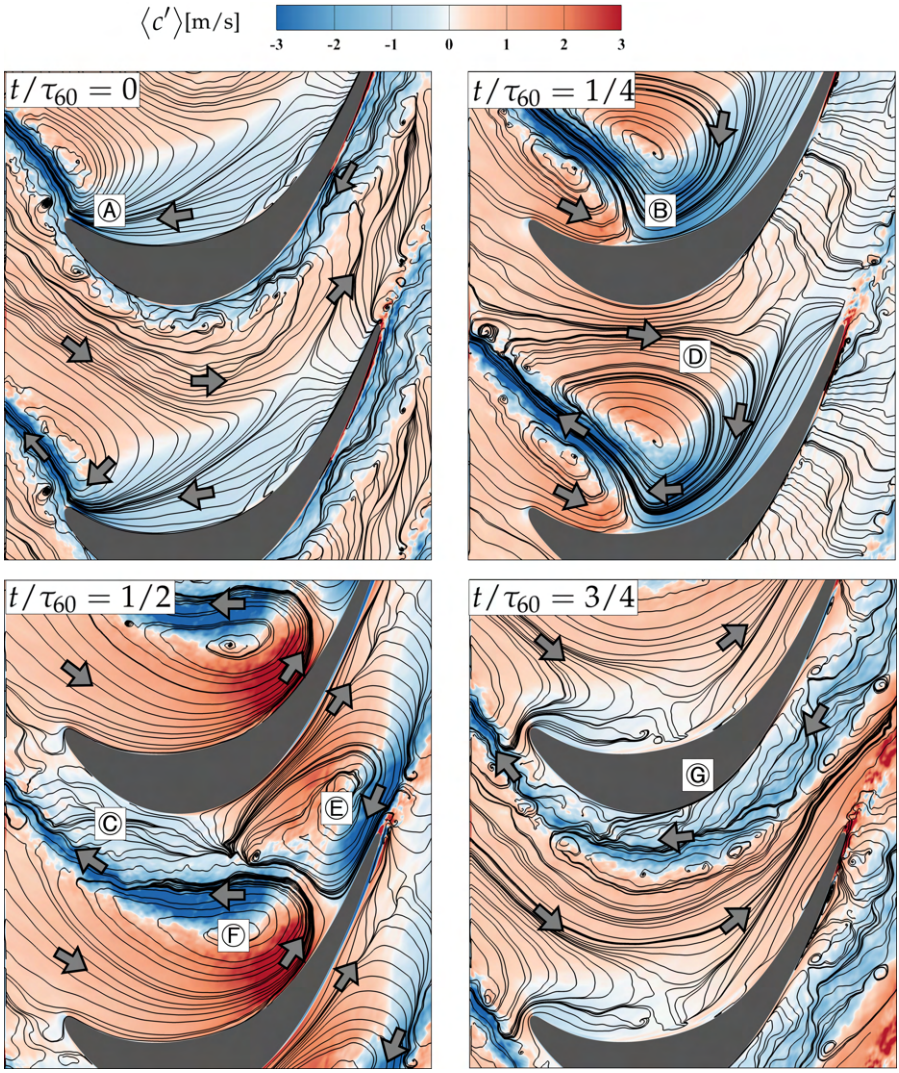

Figure 4.12: Temporal evolution of wake kinematics at 50% constant span visualized via contours of phase-averaged velocity fluctuation $\tilde{c}$ for OP-W60.

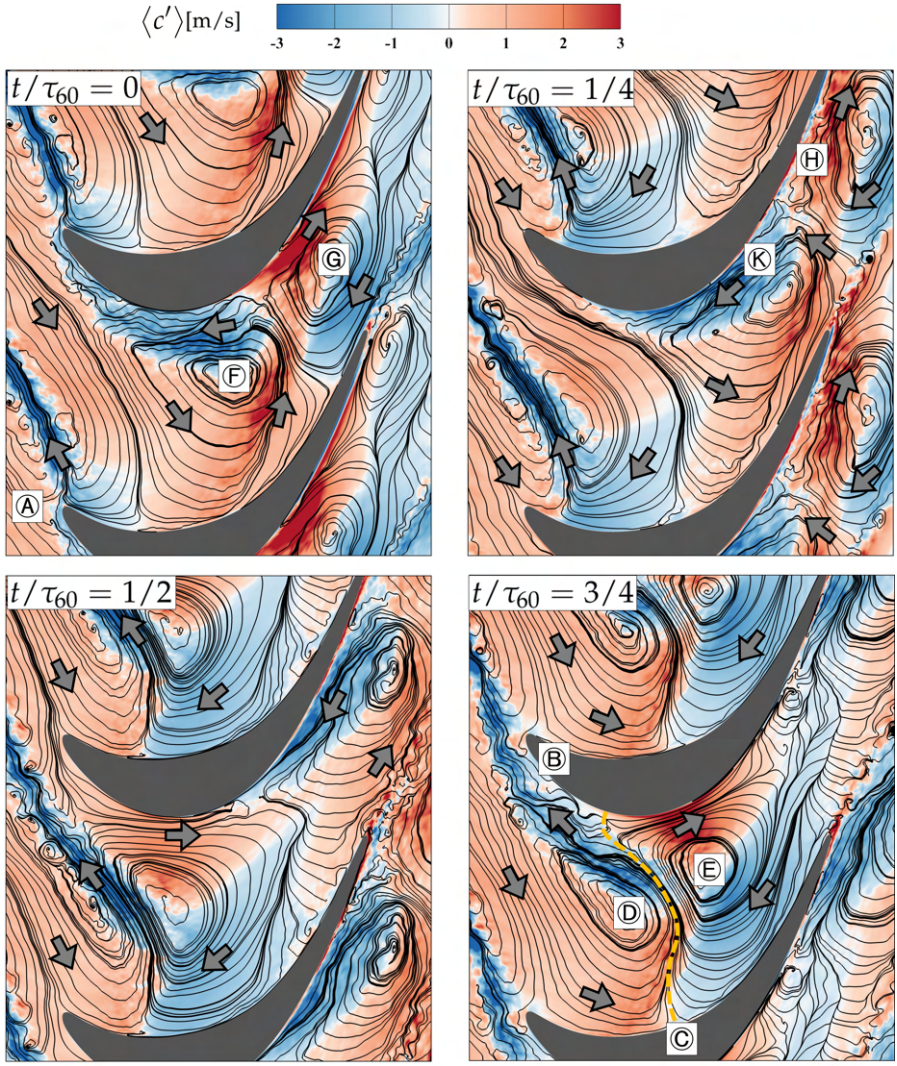

Figure 4.13: Temporal evolution of wake kinematics at 50% constant span visualized via contours of phase-averaged velocity fluctuation $\tilde{c}$ for OP-W180.

cessive areas (H+K) enter in which the boundary layer material is first accelerated and then decelerated. In contrast to the previous case, these two areas are of similar spatial extension and therefore their temporal influence on the flow is comparable. In addition, the wake in case of a low Strouhal number has a much lower turbulent intensity due to the lower relative flow velocity, so that a reduced influence on the boundary layer can be expected, which will be analyzed in the following.

4.4.2 Time space analysis

The time space analysis performed in the following comprises the time-exact evaluation of the temporal progression of different boundary layer parameters, such as the wall shear stress and the shape factor along the blade surface. For this purpose, these parameters are visualized as contour plots in a path-time diagram, which allows the spatial development of the different boundary layer states to be represented in a temporal context.

A comparison of the numerical predictions with the experimental data is shown in Fig. 4.14 for both perturbed operating points and reveals excellent agreement. Therefore a verification of the kinematic interactions between the incoming wakes and the boundary layer predicted by the LES is ensured, which justifies a further evaluation of the transient data based on the LES data.

4.4.2.1 Wall shear stress

OP-CT operating point

Figure 4.15 illustrates the time-space distribution of the absolute wall shear stress $|\boldsymbol{\tau}_{\mathrm{w}}|$ along the suction side blade surface. To allow for a distinction of separated flow regions, an iso-line is indicated in white for $\boldsymbol{\tau}_{\mathrm{w,tan}} = 0$. The time axis of both representations is normalized with the bar passing time τ_{180} to ensure better comparability with the following illustrations regarding the perturbed operating points.

For the unperturbed inflow (OP-CL) case (Fig. 4.15 (left)) the separation line is clearly distinguishable at around $S/S^* \approx 0.82$. Downstream there is a uniform oscillation of the reattachment line caused by the periodic shedding of spanwise KH vortices, which becomes evident from the convective character of the visualized contours (*"footprints of the vortex structures, from bottom left to top right"*). As a consequence, the entire detached shear layer oscillates due

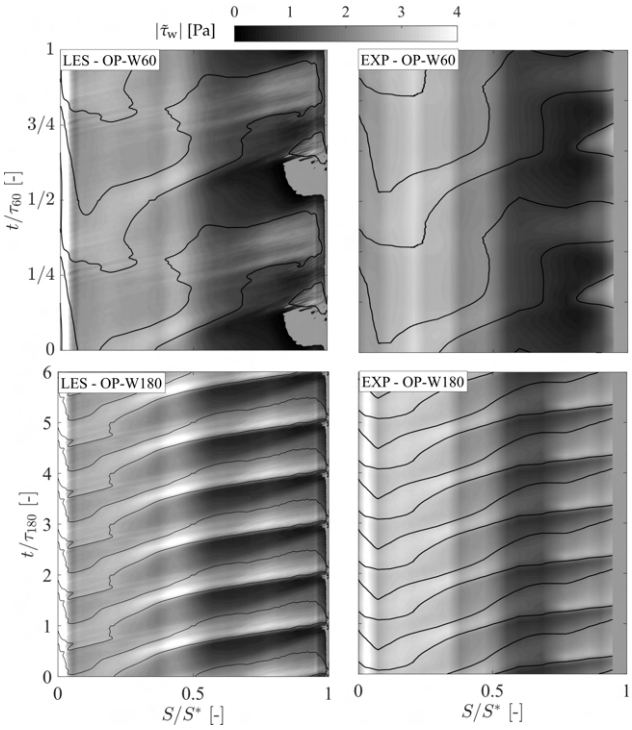

Figure 4.14: Verification of the phase-averaged absolute wall shear stress distribution $|\overline{\boldsymbol{\tau}}_w|$ along the suction side blade surface for the OP-W60 (top) and the OP-W180 (bottom) operating points, with wake paths highlighted via black lines.

to the periodic bubble "breathing", as *Hatman and Wang* [38] describes, which also causes a periodic oscillation of the separation line, although it is much less pronounced than that of the reattachment line.

Within these footprints downstream of $S \approx 0.9$ a rapid increase of the wall shear stress is observable (cf. Fig. 4.9), which is caused by the near-wall breakdown of the KH rolls in the area of the transition onset. This might be a direct consequence of a vortex wall interaction described by *Hatman and Wang* [38], which has to be analyzed further in the following.

A closer look reveals that there are about 17 shedding cycles within two periods τ_{180}, which corresponds to a shedding frequency of approximately $f_{KH} \approx 1500\,\text{Hz}$, or a Strouhal number of $\text{Sr}_{\theta,\text{md}} \approx 0.0083$ related to the max-

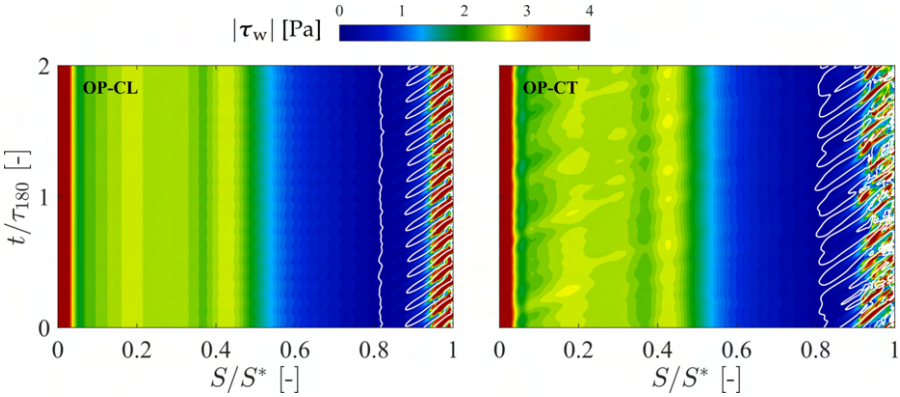

Figure 4.15: Time-space visualization of the absolute wall shear stress $|\boldsymbol{\tau}_w|$ along the suction side blade surface for the OP-CL (left) and the OP-CT (right) operating points. Separation line is highlighted via a white iso-line.

imum displacement thickness θ_{md} of the boundary layer and the velocity at the edge of the boundary layer $\overline{c}_{emd}$ at S_{md}.

In Fig. 4.15 (right), a clearly different picture is shown for the case of turbulent inflow (OP-CT). The influence of the inflow turbulence can be seen already in the area of the leading edge through regions of increased/reduced wall shear stress, even if this does not seem to have a major influence on the local course of the boundary layer. In the area of the laminar separation bubble, the influence of the turbulence manifests in a significantly non-uniform course of the separation line and of the footprints of the spanwise KH rolls in the area of their breakdown.

To what extent this significant difference is caused by instabilities already introduced upstream in the laminar boundary layer or by a direct influence of the inflowing turbulence on the vortex decay process cannot be said on the basis of the analyses presented so far. For this purpose, time-domain and frequency-domain analyses will be shown in later sections.

Perturbed operating points

The time-space plots for the two perturbed cases are shown in Fig. 4.16. For better comparability, the unperturbed case OP-CT is shown above the plots. The presented distributions are based on phase-averaged data $|\langle\boldsymbol{\tau}_w\rangle|$, which were additionally spatially averaged in spanwise direction for a better clarity

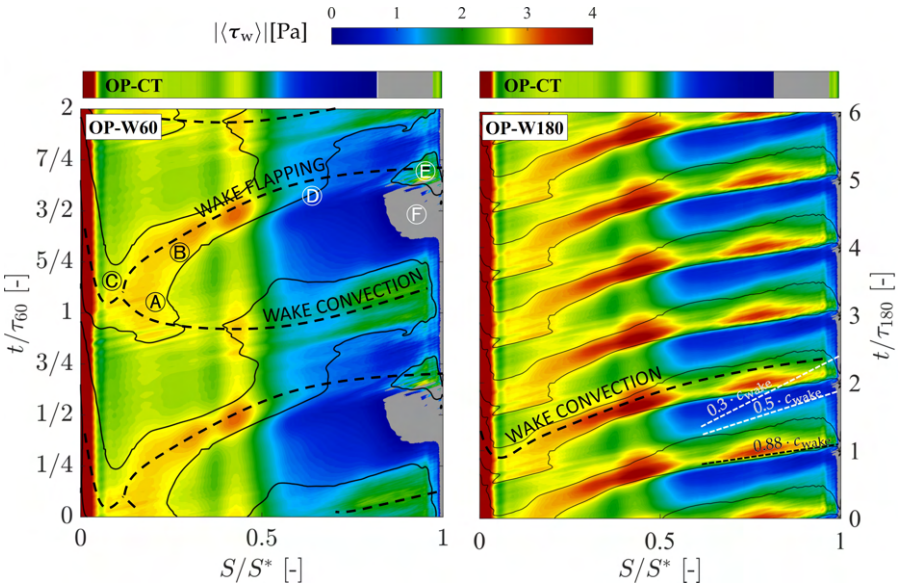

Figure 4.16: Time-space visualization of the phase-averaged absolute wall shear stress $|\langle\tau_w\rangle|$ along the suction side blade surface for the OP-W60 (left) and the OP-W180 (right) operating points, with wake paths highlighted via black lines. Separated flow regions are blanked (grey areas).

(cf. section 3.3.1). A comparison of the differently averaged distributions with the raw data is shown in Fig. 4.17.

To better identify the wake paths, they are highlighted with black isolines, based on a normalized variant of the phase-averaged wall shear stress:

$$|\langle\tau_w(S,t)\rangle|_{norm} = \frac{|\langle\tau_w(S,t)\rangle| - \min(|\langle\tau_w(S)\rangle|)}{\max(|\langle\tau_w(S)\rangle|) - \min(|\langle\tau_w(S)\rangle|)}. \tag{4.8}$$

OP-W180 operating point

Since this operating point has a much simpler structure of the wall shear stress distribution, it will be considered first in the following. For the high Strouhal number (Sr = 1.33) OP-W180 case (Fig. 4.16 (right)) the wake paths are clearly distinguishable as contours of increased wall shear stress running from bottom left to top right. These areas are mainly affected by the vortical structure, which builds in front of the wake, and is pushed towards the

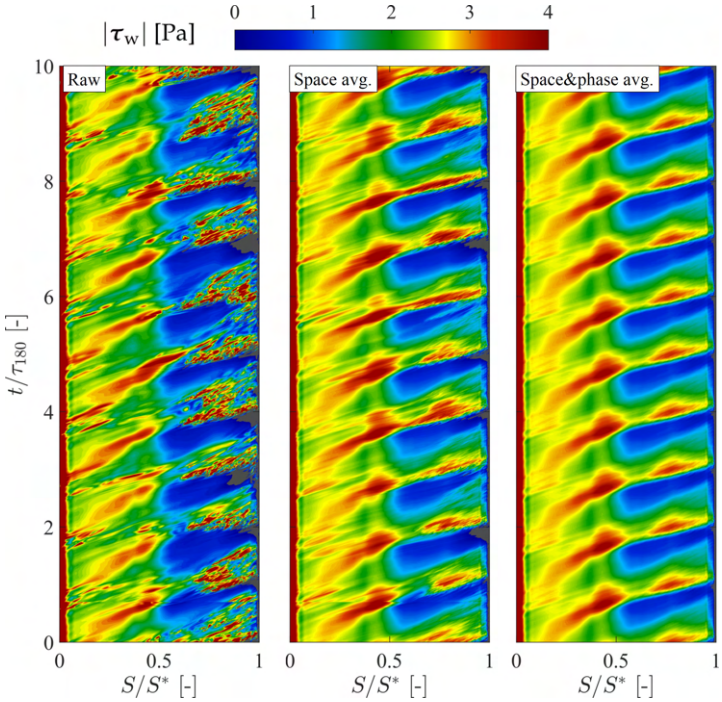

Figure 4.17: Influence of the averaging procedure on the distribution of the absolute wall shear stress $|\overline{\tau}_w|$ along the suction side blade surface for the OP-W180. Separated flow regions are blanked (gray areas).

trailing edge (cf. Fig. 4.13), resulting in an increase of wall shear stress due to the accelerated fluid. While the relative increase (compared to the unaffected areas) upstream of the suction peak ($S < 0.5$) is less pronounced, it is progressively enhanced downstream of the suction peak as a consequence of the destabilization effect of the APG on the boundary layer.

Due to the increased Strouhal number, the wakes of the rotating bars exhibit high turbulent kinetic energy at a high disturbance frequency (bar passing frequency). As a consequence, the impulse exchange between the incoming wakes and the blade boundary layer is high enough that a separation of the flow is completely suppressed (cf. reference case shown above), which is caused by the interaction of different phenomena:

Within the wake affected region (black iso line) the energy transfer leads to a local change of the boundary layer into the turbulent state via the mechanism of bypass transition and the direct formation of turbulent spots, indicated by the red areas of strongly increased wall shear stress (these areas are even more clearly visible in the raw data shown in Fig 4.17).

According to *Halstead et al.* [34] (cf. section 2.2.2.4) the front of these spots moves slower (about $0.88 \cdot c_{\text{wake}}$) than the wakes convected with the free stream velocity while the rear boundary moves with about $0.5 \cdot c_{\text{wake}}$, which results in the fan shaped structure of the footprints of those spots.

However, even outside the areas directly influenced by the wakes the wall shear stress is slightly increased inside the calmed regions compared to the reference case. Here, according to *Mahallati et al.* [69], a dampening of instabilities leads to a delay of transition while the boundary layer remains attached to the blade surface due to the still increased energy during its recovery process. As the trailing edge of the calmed region spreads with about $0.3 \cdot c_{\text{wake}}$ it forms a kind of fan, which is clearly visible behind the region directly influenced by the wake.

OP-W60 operating point

The wall shear stress distribution for the OP-W60 case at low Strouhal number ($\text{Sr} = 0.43$) is shown in Fig. 4.16 (left). First of all, the reduced disturbance frequency is noticeable, which consequently increases the time interval between the wake cycles.

Another significant difference is the course of the wake paths, which is highlighted by the dotted lines and already indicates that in this case an analysis of the underlying phenomena has to be performed with the help of an exact knowledge based on the wake kinematics described above.

It becomes clear, that unlike the case of high Strouhal number, there is no unique wake path to recognize at first sight. In addition, the iso-line distribution shown by the normalized wall shear stress in this case shows a misleading course, which impedes interpretation.

As explained in the previous section, in the case of a lower Strouhal number, the wake lies flat against the blade surface (cf. Fig. 4.12 (G)), which can be seen in a very flat curve of what is here called the wake convection line (A).

This flat impingement of the wake occurs almost simultaneously along the entire blade surface and leads to a temporal increase of the wall shear stress as the wake fluid is flushed down the suction side surface, whereby a flow separation in the area of the rear edge of the blade can be momentarily prevented.

Along the here called wake flapping line (B) the influence of the cell of accelerated flow upstream the wake's leading edge (cf. Fig. 4.12 (D)) manifests in an increase of wall shear stress. Shortly downstream of the suction peak, however, this effect loses intensity so that an increase in wall shear stress is only marginally noticeable (D).

As a consequence, the contour of the normalized wall shear stress in this region "jumps" into the range of the wake convection line, whereby a false impression of the actual wake convection could be given. This effect is also evident in the experimental data shown in Fig. 4.14.

Further downstream, however, the wake flapping causes a fast evacuation of accelerated fluid and a subsequent turbulent reattachment (E) of the completely detached shear layer (F). This results in a change of the transition mode from the transition via a laminar separation bubble to that of an attached bypass transition, which will be illustrated in section 4.4.3.

Since only a qualitative analysis of the boundary layer course can be made on the basis of the wall shear stresses, but no absolute statements about the actual boundary layer condition, an analysis of the temporal development of the shape factor H_{12} will be carried out in a similar way in the following.

4.4.2.2 Shape factor

To get an impression of the unsteady development of the boundary layer state, the shape factor H_{12} is now analyzed in its temporal development using time space representations.

Since a precise integration of the boundary layer thicknesses (cf. section 2.2.1) is required for an exact determination of the shape factor, in this case it is not sufficient to use only the phase-averaged data, since especially in the wake influenced area a data base of 10 bar passings is by far not sufficient to generate smooth velocity profiles. Therefore, also in this case a spatial averaging in spanwise direction was additionally performed, which led to very satisfactory results, as depicted in Fig. 3.13.

As in this case this spatial averaging is only possible on the basis of the 3D output data, the volume output described in section 3.2.5 was used for this analysis, which is why the evaluation is limited to $S/S^* > 0.6$.

The distributions of H_{12} are shown in Fig. 4.18 for the two perturbed operating points, whereby this time only 2 bar passings are shown in both cases to enhance clarity. As a reference the OP-CT is shown above both figures.

OP-W60 operating point

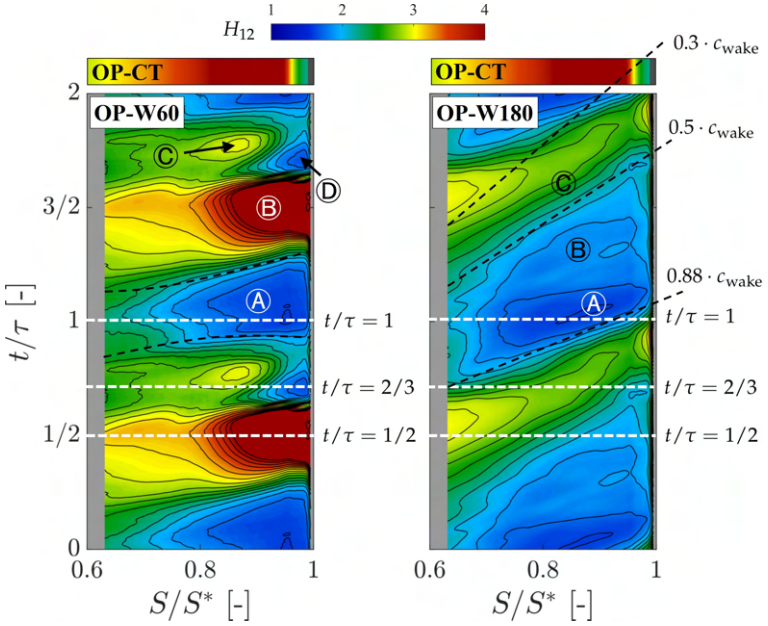

Figure 4.18: Time-space visualization of the phase-averaged shape factor H_{12} along the rear portion of the suction side blade surface for the OP-W60 (left) and the OP-W180 (right) operating points

In the case of a low Strouhal number (OP-W60), the wake convection is clearly recognizable as an area of low shape factor (blue area) (A). With values of $H_{12} < 1.6$, the areas shown in blue clearly represent a turbulent boundary layer state, which also corresponds to the areas of higher wall shear stress in Fig. 4.16.

In the red regions (B), a strong increase in the shape factor $H_{12} > 4$ indicates the intermittent separation of the flow, which is initiated upstream with increasing destabilization (yellow/orange areas) of the laminar (green area) boundary layer.

These regions are followed in time by a localized area of unstable laminar boundary layer (C), which seems to accumulate in front of the turbulent region (D) (cf. 4.16 (E)), indicating an attached boundary layer transition mode. This phenomenon is forced by the wake flapping effect, causing an evacuation of the accelerated fluid cell which is pushed over the separated shear layer thus resulting in an energization and a subsequent reattachment. Although the yellow destabilized region (C) continues to propagate toward the

trailing edge, the following wake convection prevents the attached boundary layer from separating from the blade surface again.

OP-W180 operating point

In the case of high Strouhal number (OP-W180), the boundary layer states are well structured, as expected. Within the regions directly affected by the wakes, a turbulent boundary layer is clearly indicated by blue regions of low shape factors. Here, the cell of accelerated fluid causes a deep blue region (A), which is followed by a light blue fan caused by the upstream cell of decelerated fluid (region (B)).

The region directly affected by the incoming wakes is followed in time by a calmed region (C), whose leading and trailing edge spread with $0.88 \cdot c_{\mathrm{wake}}$ and $0.5 \cdot c_{\mathrm{wake}}$ respectively, according to the theory of turbulent spot convection illustrated in Fig. 2.11.

This region is characterized by increased stability and is therefore less susceptible to flow separation is not only reflected in the fact that flow separation. This is also prevented in the area not directly influenced by the wake, but also in the development of the shape factor, which indicates a stabilization of the laminar boundary layer by the change from yellow to green in the direction of the trailing edge.

4.4.3 Flow visualization

By analyzing the temporal course of the wall shear stress and the shape factor along the blade surface, a comprehensive picture of the boundary layer condition could be obtained for the unperturbed cases as well as for both wake disturbed cases. The aim of the following section is to assign the flow topologies to the different flow states with the help of vortex core visualization in order to obtain a visual impression of the flow in the absence and presence of incoming wakes.

4.4.3.1 Unperturbed inflow cases (OP-CL & OP-CT)

The theory of laminar separation bubbles described in 2.2.2.3 and analyzed in section 4.3.2 for the present case, forecasts the presence of inviscid instabilities (KH-instabilities) within the detached shear layer, which, according to the literature, lead to a rolling up of shear layer material and thus the formation of spanwise oriented KH-rolls. An analysis of the temporal progression of the wall shear stress in the rear area of the blade suction side could support

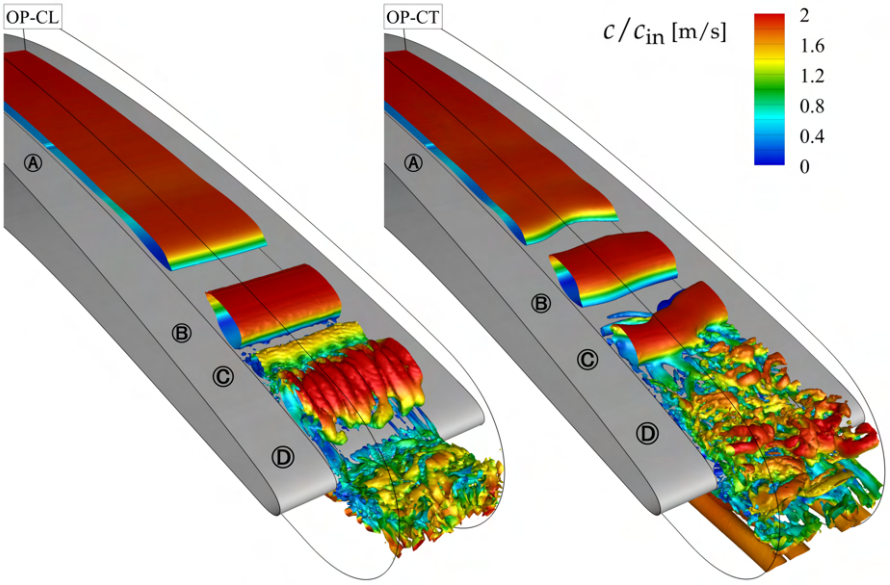

Figure 4.19: Q-criterion at $Q = 1 \times 10^6\,\text{s}^{-2}$ colored by the normalized absolute velocity c/c_{in} at arbitrary snapshots for OP-CL (left) and OP-CT (right).

this theory, especially in the case of a laminar inflow. It will now be shown for the two unperturbed inflow cases that the dominant flow structures are actually attributable to this mechanism and how the turbulence influences these structures.

The basis for this is the 3-dimensional visualization of vortex core regions using the Q-criterion shown in Fig. 4.19, which enables the extraction of coherent flow structures based on the velocity gradient tensor (cf. section 3.3.2).

Figure 4.19 shows the distribution of an iso-surface for $Q = 1 \times 10^6\,\text{s}^{-2}$ colored by the normalized absolute velocity c/c_{in}. For the OP-CL shown on the left, a laminar, detached shear layer appears in region (A), which begins to form 2-dimensional, spanwise running KH rolls in region (B). With increasing flow distance, 3-dimensional structures develop near the wall (C), indicating the presence of a viscous instability, as described by *McAuliffe and*

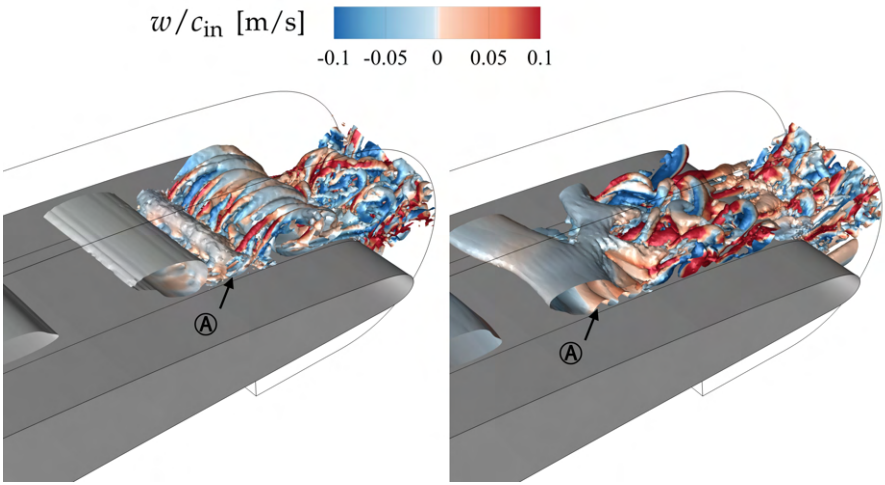

Figure 4.20: Closeup of Q-criterion at $Q = 1 \times 10^6\,\text{s}^{-2}$ colored by the normalized spanwise velocity w/c_{in} at arbitrary snapshots for OP-CL (left) and OP-CT (right).

Yaras [77]. This is caused by an interaction between the vortical structures and the blade surface (*Hatman and Wang* [38]).

The first emergence of the 3-dimensional flow structures is particularly evident inside the near-wall region from the detailed representation in Fig. 4.20 (region (A)). Here, the coloring by means of the spanwise velocity component in both investigated operating points shows initial 3d effects in the aft near-wall region of the laminar separation bubble, which is transported towards the shear layer by the vortical motion of the KH-rolls. A comparison with the analysis of the turbulence states from section 3.3.3 shows that this region coincides with region (C) from Fig. 4.10, which marks the transition of the near-wall 1-component turbulence into a 2-dimensional rodlike turbulence state.

Allthough, for both cases this near wall instability seems to play in important role in the process of laminar to turbulent transition of the separated shear layer, for the OP-CL the KH-rolls in this area show a nearly 2-dimensional structure, which gradually becomes 3-dimensional towards the trailing edge (Fig. 4.19 region (D)), but does not fully break down before reaching the trailing edge of the blade.

For the case with inlet turbulence shown on the right, the situation is clearly different. Starting from a laminar shear layer in region (A), an asymmetric distortion of the 2-dimensional KH structures (B) can already be seen during the formation of the 2-dimensional KH structures (B), which is further intensified downstream (C) and finally leads to an accelerated breakdown (D) of these structures into smaller turbulent scales. This deformation of the coherent structures makes them become destabilized, so that the interaction with the near-wall instability can lead to an accelerated turbulent breakdown.

Along the suction side, the occurrence of streamwise running Görtler vortices (cf. [33, 93]) is also visible, whose formation is obviously triggered by the free stream turbulence. At this point, however, these phenomena will not be discussed further, as the focus of this work is limited to the mechanisms on the suction side.

In summary, the influence of the turbulence apparently causes an acceleration of the transition within the detached shear layer, which could already be observed when comparing the time-averaged wall shear stress curves (cf. section 4.3.3). Here the asymmetry of the coherent flow structures seems to play an important role, which will be analyzed more closely in the following sections. In both cases, the analysis of the 3-dimensional flow structures yields the result that the turbulent breakdown of the coherent 2-dimensional KH-rolls is initiated near the wall, indicating an interaction with a near-wall viscous instability, which is in agreement with the findings from the analysis of the turbulence states from section 3.3.3.

4.4.3.2 Perturbed cases

Figure 4.21 shows the distribution of the phase-averaged Q-criterion using iso-surfaces at $Q = 2 \times 10^6\,\mathrm{s}^{-2}$ for the OP-W60 case for three selected time steps along one wake passing period. The relative position of the time steps in the wake process can be found in Fig. 4.18. In this case, the isosurface is colored with the phase-averaged tangential fluctuation velocity to give an impression of whether the respective flow area is currently influenced by accelerated or decelerated flow cells (cf. Fig. 4.12).

- $\boldsymbol{t/\tau = 1/2}$:
  At this point, a clearly laminar boundary layer is visible in the front part of the evaluation volume, which detaches further downstream and forms KH structures, typical for a separated shear layer transition. It can thus be concluded that the flow structures depicted by the Q-criterion correspond to the course of the shape parameter at $t/\tau = 1/2$ in Fig. 4.18.

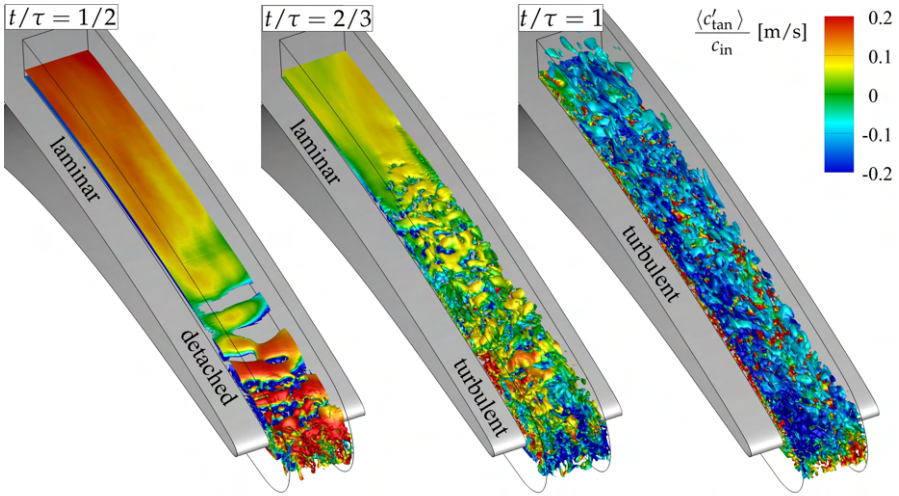

Figure 4.21: Phase-averaged Q-criterion at $Q = 2 \times 10^6\,\text{s}^{-2}$ colored by the phase-averaged tangential fluctuation velocity $\langle c'_{\tan} \rangle$ for three different snapshots (cf. Fig. 4.18) at OP-W60.

The illustration also clearly shows the incoming cell of accelerated fluid as it is pushed downstream in front of the wake as a result of the previously described wake flapping (see Fig. 4.12 (E)), which is recognizable at the laminar region by the increased tangential fluctuation speed (red area). However, this region has an apparently low degree of turbulence, so that at this level of Q-criterion no vortex structures are visible in this area.

- $t/\tau = 2/3$:
  At this point, the cell of accelerated fluid reached the trailing edge, where the energy transfer already caused a turbulent reattachment of the shear layer. The turbulent character of the attached boundary layer is clearly evident from the vortex structures near the blade's trailing edge. At this point in time, an attached transition can be assumed, which is in accordance with the previous observations. The relatively low energy content of the cell pushed in front of the wake allows only in the rear part of the blade to put the boundary layer into a turbulent state, because here the boundary layer is much more susceptible to external disturbances due to its instability. Further upstream, however, a laminar boundary layer is still present.

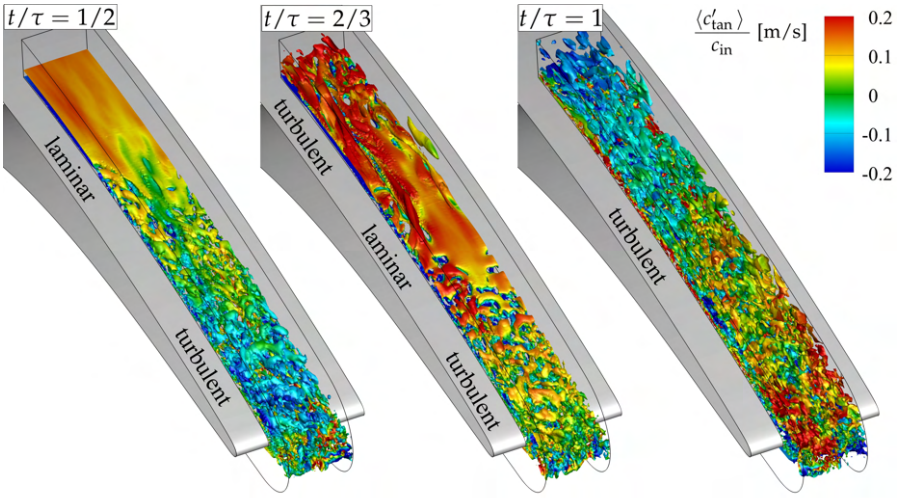

Figure 4.22: Phase-averaged Q-criterion at $Q = 2 \times 10^6\,\text{s}^{-2}$ colored by the phase-averaged tangential fluctuation velocity $\langle c'_{\tan} \rangle$ for three different snapshots (cf. Fig. 4.18) at OP-W180.

- ***t*/τ = 1**:
  At this point, the fluid in the entire evaluation volume is affected by the wake as it is flushed along the blade suction side. This can be clearly seen in the vortex structures of negative tangential fluctuation velocity (blue), which occur within the wake due to the negative jet effect (cf. Fig. 4.12) as the wake bends over the blade surface. This results in a turbulent boundary layer in the entire rear area of the blade suction side, which is in accordance with the course of the shape parameter presented in Fig. 4.18.

For the high Strouhal number case OP-W180 the same illustration is presented in Fig. 4.22. Also in this case the presented time steps are highlighted in Fig. 4.18 within the course of the unsteady shape factor. A description of the presented distributions of the Q-criterion is presented in the following.

- ***t*/τ = 1/2**:
  Similar to the previously described case, also here, the approach of the cell of accelerated fluid upstream of the incoming wake is indicated by the increased tangential fluctuation velocity (red area) in the laminar region. However, unlike in the case of low Strouhal number, the flow in the rear part of the blade is not detached from the blade surface but in a turbulent state, as it is directly affected by the previous wake impact. This is clearly

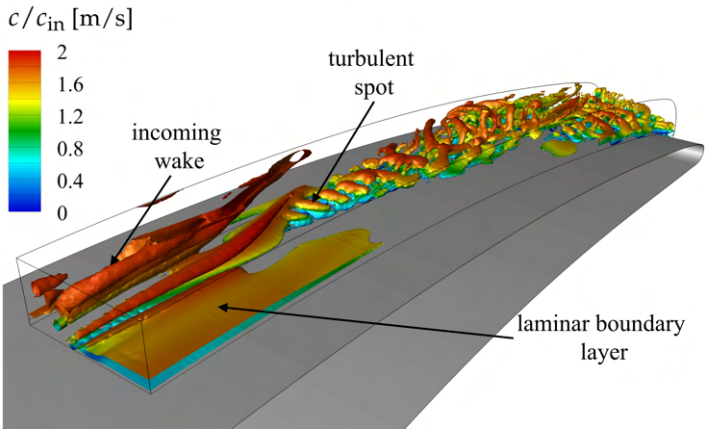

Figure 4.23: Closeup of a turbulent spot developing along the suction side via an isosurface at $Q = 2 \times 10^6\,\text{s}^{-2}$ colored by normalized absolute velocity c/c_{in} at OP-W180.

recognizable by the blue colored vortex structures and is in accordance with the observations made before.

- $t/\tau = 2/3$:
  At this point, the vortex structures within the accelerated cell (red area) are already visible in the upstream part of the evaluation volume. Here they cause the direct formation of turbulent spots inside the laminar boundary layer, which grow in spanwise direction as they get convected downstream towards the trailing edge as illustrated in the closeup presented in Fig. 4.23 on the example of a non phase-averaged snapshot. For the presented time step, the increased momentum exchange thus causes a turbulent boundary layer via the mechanism of bypass transition while only a small strip of the blade boundary layer is still visible as being laminar.

- $t/\tau = 1$:
  The core region of the wake has reached the evaluation volume in this time step and is causing a fully turbulent flow in the entire region, which is also reflected by the shape factor in Fig. 4.18. The cell of accelerated flow in front of the wake is clearly visible by the red colored areas, while the upstream cell of decelerated fluid is indicated by the blue colored regions.

4.4.4 Summary

With the help of the time-exact analysis of the transient data, the KH-mechanism could be confirmed to play a dominant role in the transition process of both unperturbed operating points under investigation. While in the absence of FST the KH structures are mostly 2-dimensional, the presence of inflow turbulence leads to a strong distortion of these structures, resulting in an accelerated turbulent breakdown.

Regarding the two perturbed operating points, the fundamentally different character of the transient boundary layer state was found. It was shown that in the case of a low Strouhal number, intermittent flow separation takes place despite the wake influence, while flow separation is completely suppressed in the case of a high Strouhal number.

With the help of the detailed analysis of the wake kinematics, the cause of the transition effects occurring in both the numerical and the experimental data could be determined and linked to quantifiable boundary layer parameters like shape parameter and wall shear stress. For the case of low Strouhal number it was found that besides the direct wake effect (referred to as *wake convection*), an additional wake effect could be identified (referred to as *wake flapping*), which is characterized by a sudden evacuation of passage fluid over the trailing edge of the blade and has a significant influence on the resulting transition scenario.

The results of the time domain analysis therefore not only underline the findings of *Halstead et al.* [34, 36] but also add important details related to the LPT specific wake convection phenomena.

4.5 Frequency domain evaluation

The following chapter comprises frequency domain based analyses of the time resolved flow fields for the different operating points under consideration. The primary goal is to identify characteristic frequencies within the boundary layer and thus to follow the development of instability mechanisms along the flow.

4.5.1 General approach

As described in section 2.2.2.3, the process of transition in detached shear layers can be characterized by various instability mechanisms and their in-

teraction. These mechanisms involve the viscous TS instability, which generally originates upstream of the separation bubble, and the inviscid KH instability, which is an inflectional instability by nature that develops within the detached shear layer.

Since a frequency analysis on the basis of the entire flow area quickly generates confusingly large data sets, it makes sense to first define a region to which the frequency analysis is limited. Therefore, based on the statistics sampled on the OGRID evaluation plane (cf. section 3.2.5), the line along the blade suction side is extracted where the standard deviation (STD) of the velocity signal reaches its maximum in the wall-normal direction $\sigma(c)_{\max}$.

This is shown in Fig. 4.24 (top row) on the example of the unperturbed inflow cases OP-CL (left) and OP-CT (right). It should be noted that for a more space-saving representation, the data has been transformed to a Cartesian grid, resulting in a distortion of the flow field, especially near the trailing edge. However, this is only an optical disadvantage, which does not affect the results of the following analyses.

4.5.2 Unperturbed inflow cases

The top row of Fig. 4.24 shows the distribution of STD for both unperturbed inflow operating points with the line of maximum STD highlighted in white. In the case of laminar inflow, an increased STD is visible only in the immediate vicinity of the onset of the LSB, which is a direct consequence of the inviscid KH-instability and the subsequent formation of the KH-rolls.

For the turbulent inflow case, elevated STD levels are also visible even further upstream, which can be attributed to fluctuations, which are introduced to the attached laminar boundary layer by the free stream turbulence.

For a more distinct analysis, the bottom line of the diagram shows the course of the STD for the individual transformed velocity components along the line of maximum STD.

For the turbulent inflow case, there is a nearly constant course in all velocity components upstream of the separation bubble, which indicates a saturation of the fluctuations introduced into the boundary layer by the the free stream turbulence.

This effect is not observed in the case of laminar inflow, where only for the normal component of the velocity the STD seems to saturate shortly before the onset of the LSB at almost the same level as for the OP-CT case. The fact that in OP-CL the fluctuations of all velocity components increase upstream

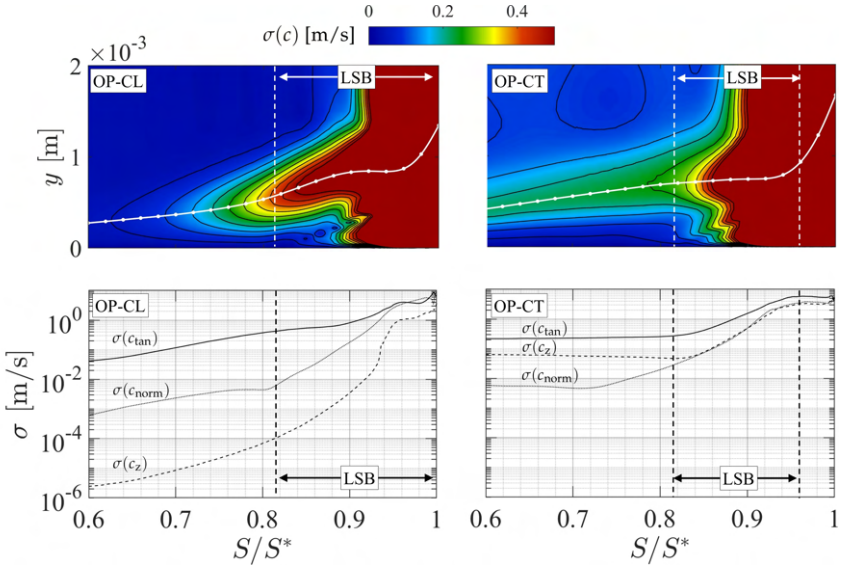

Figure 4.24: Top: Distribution of the STD of the absolute velocity $\sigma(c)$ near the trailing edge of the profile for OP-CL (left) and OP-CT (right) with line of maximum STD highlighted in white. Bottom: Progression of the STD for each velocity component along the line of maximum STD.

of the LSB indicates the growth of viscous instabilities that arise near the suction peak with the onset of the APG.

It is also noticeable that while the STD of the tangential and normal components rise towards a similar level as for the OP-CT, the spanwise component is significantly lower, indicating an initially 2-dimensional character of the boundary layer instabilities. This is in line with the findings of the previous sections, where initial 3-dimensionality of the coherent flow structures was initiated in the aft portion of the separation bubble (cf. Fig. 4.20).

After the onset of LSB, an exponential increase of the STD is observed in the case of the OP-CT, which indicates the emergence of additional instability mechanisms, whereby the normal component already begins to rise slightly upstream, which allows the cross-flow fluctuations to be in equilibrium after the onset of the LSB. In the case of laminar inflow, this intensified increase is only clearly visible in the STD of the normal component, as it was already previously saturated. Due to the low level of spanwise fluctuations there is no cross-flow equilibrium as it is apparent in the OP-CT.

While reaching the maximum values of the STD (non-linear saturation, cf. *Rist* [101]) in the OP-CT at the end of the LSB indicates a complete transition within the detached layer, this state is not reached in the OP-CL.

Nevertheless, it can be concluded that within the LSB, the fluctuation values of all three velocity components tend towards a state of equilibrium (turbulent break down), which causes a more or less drastic increase of the fluctuations depending on the initial fluctuation level when entering the LSB.

To what extent the exponential increase of STD within the LSB is caused by the presence of additional inviscid KH instability and if so, whether it is influenced by TS instability will be determined in the following with the help of a detailed frequency domain analysis.

For the two perturbed cases it has to be evaluated if these transition mechanisms still exist and if so, how they are influenced by the interaction with the incoming wakes.

For this purpose, the transient data are interpolated to the line of maximum STD ($0.6 < S/S^* < 1$) for each respective case, resulting in 41 ($\Delta(S/S^*) = 0.01$) data sets equidistantly distributed in streamwise direction, which form the basis for the performed analyses presented in the following.

4.5.2.1 OP-CL

The spectra corresponding to the absolute velocity signal $c(\boldsymbol{x}, t)$ for the laminar inflow are presented in Fig. 4.25 (left) for every other point along the line of maximum STD ($S/S^* > 0.6$). The color scale indicates the respective streamwise location of each spectrum, while the spectrum closest to the separation point is highlighted with a dashed black line to facilitate spatial orientation.

Especially noticeable are the increased amplitudes inside a frequency band at around $f = 1500\,\mathrm{Hz}$, which can be attributed to the KH-vortex shedding mechanism. As was already suspected during the visual inspection of Fig. 4.15, transition inside the separated shear layer occurs through the amplification of disturbances via an inviscid KH instability mode, which causes the periodic shedding of spanwise vortex structures. According to *Tennekes and Lumley* [137] the convective passing of these distinct vortical structures causes wide peaks of frequencies from $0.6f$ to $1.6f$ (half a log decade), where f is the frequency associated with the eddy passing and via Taylors hypothesis of frozen eddies, the inverse of their size [31]. This phenomenon is clearly visible in the representation of the respective spectra.

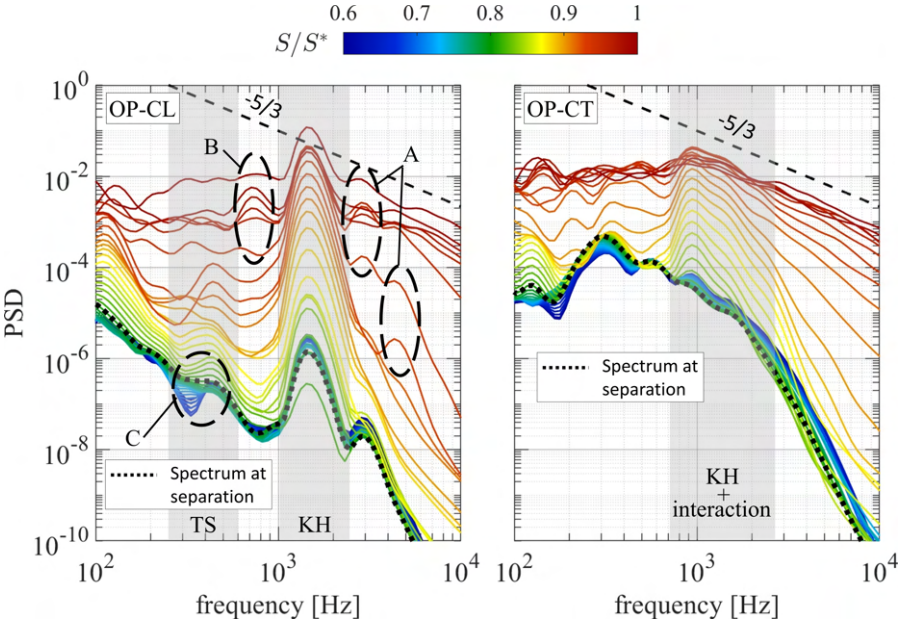

Figure 4.25: Frequency spectra of the absolute velocity signal for every other point along the line of STD for OP-CL (left), and OP-CT (right).

The occurrence of the KH-instability mode happens at a dominant frequency that for both unperturbed inflow cases is in good agreement with the typical ranges occurring in published studies of separated and free shear layers, which confirms the KH instability mode correlations summarized by *McAuliffe and Yaras* [77] and *Dähnert et al.* [21] and further verifies the numerical predictions presented in this work.

In Table 4.3 the results of the underlying work and a variety of studies concerning separated free- and boundary-layer shear flow are summarized, which encompass the range $0.005 < \mathrm{Sr}_{\theta s} < 0.016$ of instability Strouhal number

$$\mathrm{Sr}_{\theta s} = \frac{f\theta_s}{c_{\mathrm{es}}}, \tag{4.9}$$

with the the momentum thickness θ_s and the shear layer edge velocity c_{es} evaluated within the separation point.

While an exponential growth of the KH mode can be observed directly downstream of the separation point, the higher harmonic (region (A)) and subharmonic (region (B)) content only develops further downstream from about

Table 4.3: Summary of typical ranges for the instability Strouhal number from the literature

Investigators	$\mathrm{Sr}_{\theta s} = f\theta / c_{\mathrm{es}}$
present study (OP-CL & OP-CT)	0.007
Dähnert et. al [21]	0.009-0.014
Talan and Hourmouziadis [136]	0.010-0.014
McAuliffe and Yaras [73, 77]	0.008-0.016
Pauley et. al [64, 99]	0.005-0.008
Voke and Yang [140]	0.005-0.011
Ho and Huerre [41]	0.016

$S/S^* \approx 0.9$, which is a clear indication of an increasing three-dimensionality within the flow.

An additional range of increased amplitudes is found in the low-frequency range at about 300-500 Hz. These low frequency disturbances indicate the presence of the viscid TS instability, which originates upstream of the separation point within the laminar boundary layer, as also observed by *Graveline and Sjolander* [31] during their experimental investigations regarding a moderately loaded LPT. A clear indication for this is that a modulation of the peak frequency as well as an influence on the maximum amplitude is already visible upstream of the separation point (region (C)).

Although this low frequency mode is still amplified inside the separated shear layer, its growth rate is much lower than that of the KH mode. This is in accordance with the findings of various researchers [31, 70, 153], which does not necessarily imply that the TS-mode does not play a role in the transition process, as *Yang* [153] reports. In his review about bypass transition in separation bubbles he states: "It is worth noting that although the KH instability usually plays a dominant role in the separated boundary layer transition process the TS instability may still be present, interacting with the KH instability and in some cases the TS instability mechanism may play a significant role in the break down to turbulence" [55, 70, 77, 104].

4.5.2.2 OP-CT

Due to the turbulent kinetic energy from the free flow, the energy level of the spectra upstream of the separation bubble is significantly increased compared to the case of laminar inflow. Especially in the low frequency range, the spectral density is "filled up" by the turbulent content, so that an almost

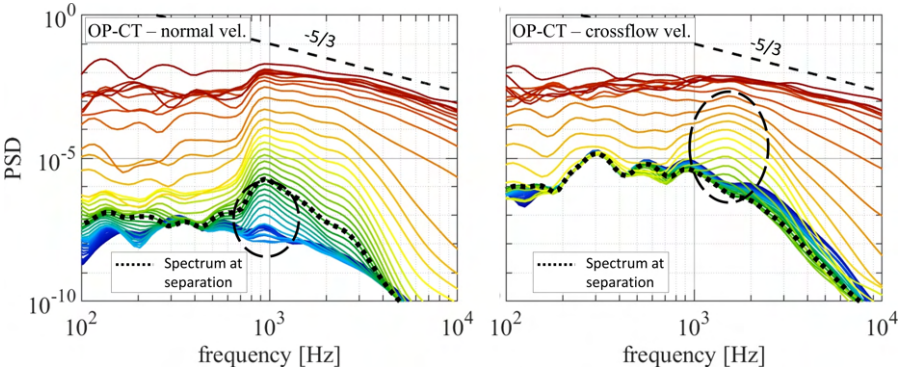

Figure 4.26: Frequency spectra of the wall normal (left) & crossflow (right) velocity signal for every other point along the line of STD for OP-CT.

uniform picture of the spectra upstream of the LSB can be observed, which initially does not provide any indication of a modal growth of certain instabilities. However, downstream of the LSB, there is a significant amplification in the area of the KH instability in a frequency band that is wider than in the case of laminar inflow and whose peak frequency is lower at approx. 1000 Hz.

It may be suspected here that the influence of free stream turbulence causes a shift in the frequency of the KH instability, since the spectra of the absolute velocity no longer show a peak at 1500 Hz. However, an analysis of the spectra of the crossflow velocity component w, which is depicted in Fig. 4.26 (right), shows that this is not the case. The frequency band associated with the KH instability is clearly visible (although it is broadened by the FST), indicating that the KH instability still plays an important role in the final breakdown of the detached shear layer towards full 3-dimensional turbulence, which was also stated by several researchers (cf. [38, 45, 77, 135]).

This becomes also evident when comparing the growth rate of the most amplified frequency, which is associated with the KH-instability $f_{\mathrm{MA}} \approx 1500$ Hz, shown in Fig. 4.27 for both unperturbed inflow operating points. Although the curve of the OP-CT is much more uniform, which is due to the stochastically modulated structure of the KH structures introduced by the free stream turbulence, the same typical exponential increase of the PSD, which is typical for the rapid growth of this inflectional instability, can be observed in a global view.

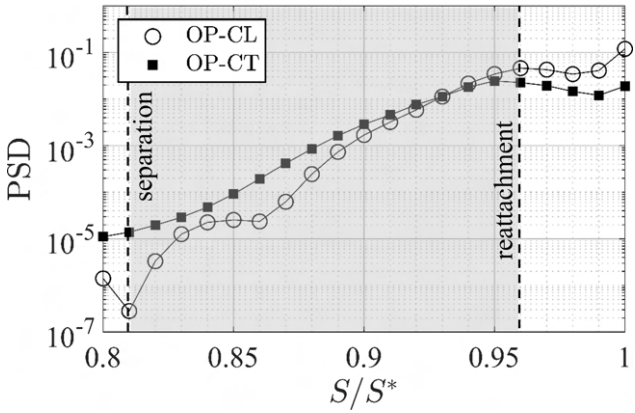

Figure 4.27: Growthrate of the most amplified frequency $f_{\mathrm{MA}} \approx 1500\,\mathrm{Hz}$ for both unperturbed inflow operating points.

The emergence of the 1000 Hz peak in contrast, is clearly visible in the spectra of the normal component way upstream of the LSB. This is an indication of a non-modal growth of an an additional mechanism interacting with the KH mode, and as a consequence results in a widening of the peak frequencies.

Even without a more detailed knowledge of the modal structures, which will be discussed in the next chapter, it is reasonable to conclude that the low frequency disturbances, which penetrate the boundary layer in the front part of the blade, introduce spanwise inhomogeneities into the streamwise velocity distribution. These cause a distortion of the spanwise KH-vortices, so that the additional peak at 1000 Hz may be attributed to the stramwise elongated structures (Klebanov modes) known from literature ([7, 32, 63, 77]).

4.5.3 Perturbed inflow cases

The line of maximum STD is presented in Fig. 4.28 (top row) for both perturbed operating points under consideration. It should be noted at this point that the color scale of the top row figures as well as the the y-axis of the bottom row figures have been adjusted compared to Fig. 4.24 to ensure a better clarity.

While the region of highest STD in the case of high Strouhal number (right) extends along the entire near wall region of the displayed blade surface, in the case of low Strouhal number it is limited to the rear portion of the blade

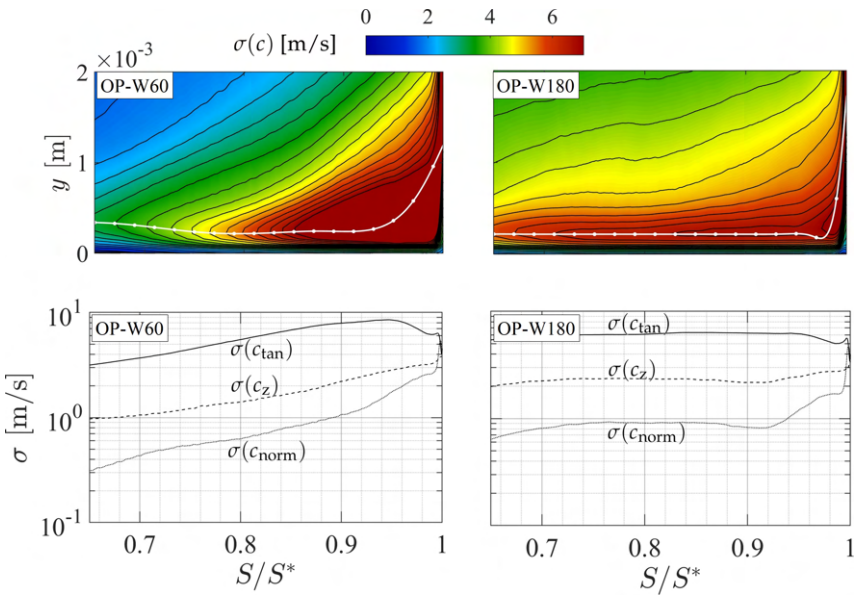

Figure 4.28: Top: Distribution of the STD of the absolute velocity $\sigma(c)$ near the trailing edge of the profile for OP-W60 (left) and OP-W180 (right) with line of maximum STD highlighted in white. Bottom: Progression of the STD for each velocity component along the line of maximum STD.

downstream of $S/S^* \approx 0.8$. This is caused by the lower turbulent intensity within the wake at a low Strouhal number, which only exerts a noticeable influence on the boundary layer when it is sufficiently weak (see section 4.4.2 Fig. 4.16 & 4.18). In addition, the intermittent boundary layer separation, which is followed by a turbulent reattachment of the flow, causes additional transient features in the vicinity of the trailing edge. This leads to a significantly higher STD inside this region compared to the high Strouhal number case.

Looking at the STD of the individual velocity components, which are shown in the bottom row of the Fig. 4.28, it is noticeable that in both cases the unsteadiness of the tangential velocity component is significantly higher than that of the other two components, which indicates that the wake has a major influence on this component. This effect can be explained by the spanwise oriented vortex regions that form in front of and behind the wake. As already shown in the analysis of wake kinematics in section 4.4.1, these vortex

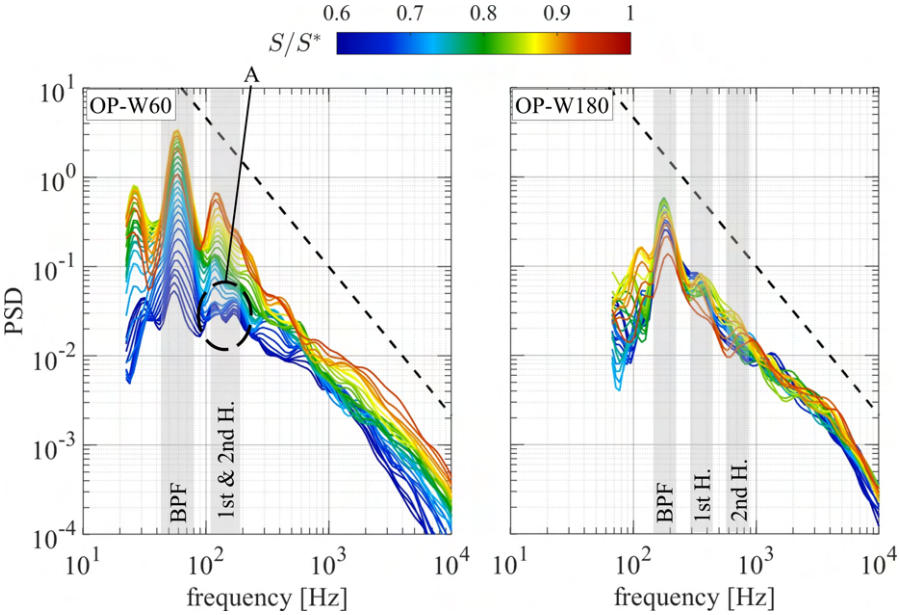

Figure 4.29: Frequency spectra of the absolute velocity signal for every other point along the line of STD for OP-W60 (left), and OP-W180 (right).

regions induce an acceleration or deceleration of the flow close to the wall, the effect of which also affects the fluctuation values.

As a consequence of the higher turbulent kinetic energy, a nearly constant course of the STDs in case of a high Strouhal number is observable, indicating a saturated boundary layer state. In case of a low Strouhal number the STDs increase exponentially in the direction of the trailing edge of the blade, also promoted by the intermittent flow separation in this region.

The spectra corresponding to both perturbed operating points are presented in Fig. 4.29 and reveal peak amplitudes in the range of the respective bar passing frequencies (BPF). In case of OP-W180 (right), this maximum is clearly distinct, while the peaks corresponding to the higher harmonics are less pronounced at lower amplitudes, which underlines the dominance of the flow effects directly caused by the wake passing within one bar passing period.

For the low Strouhal number OP-W60 case (left), the peak at the BPF is accompanied by strongly pronounced amplitudes at the higher harmonics as well as some subharmonic content, which clearly indicates an interaction of

different flow phenomena, already discussed in section 4.4.2. For example the two different transition modes, namely *wake flapping* and *wake convection* obviously result in an excitation at the 2nd harmonic of the BPF.

The fact that there are no clear peaks in the range of the previously determined KH-mode frequencies, although it was already found in section 4.4.3.2 that a KH-mode dominated intermittent flow separation occurs at this operating point, is based on the circumstance that these amplitudes are overshadowed by the wake effects in a global frequency consideration.

In the case of a periodically oscillating flow state, which introduces a strong time-dependent unsteadiness to the system, it makes sense to also perform a time-dependent frequency analysis. This is achieved by means of the continuous wavelet transformation (CWT) described in section 3.3, the results of which are explained below for the OP-W60 operating point.

Figure 4.30 shows the amplitude distribution of the CWT spectra at four equally spaced positions along the line of maximum STD (cf. Fig. 4.28 (left)) for OP-W60. The underlying velocity signals are phase-averaged to improve clarity of the results. To enable a better assignment of the phenomena to the temporal course of the boundary layer state during the wake passing, the temporal evolution of the shape factor is shown above the figure.

At a first sight, the global effect of the wake influence is visible as a uniform oscillation at the BPF, in all four spectra presented (region (A)). This effect extends over the entire passing period and only shows slight asymmetries on closer inspection, which underlines its macroscopic character.

In the case of the higher frequencies, increasing asymmetries can be detected within the passing period, which allow a separation of the phenomena occurring during a wake passing (cf. section 4.4.2).

The highlighted areas (B), which occur once per bar passing within the time window (TB) highlighted in the top figure, can be clearly assigned to the areas directly influenced by the wake (effect of *"wake convection"*). Here, the turbulent kinetic energy within the incoming wakes causes an excitation of frequencies within a broad spectrum, whose amplitude grow with increasing streamwise position, underlining the increasingly turbulent character of the boundary layer.

A further characteristic region (C) can be identified within the time window (TC), which coincides in time with the intermediate transitional boundary layer state. Here, the region of accelerated fluid, which is pushed upstream of the wake towards the trailing edge (cf. section 4.4.1), leads to an accelerated transition process within the detached shear layer, which in turn provides for a turbulent reattachment of the flow.

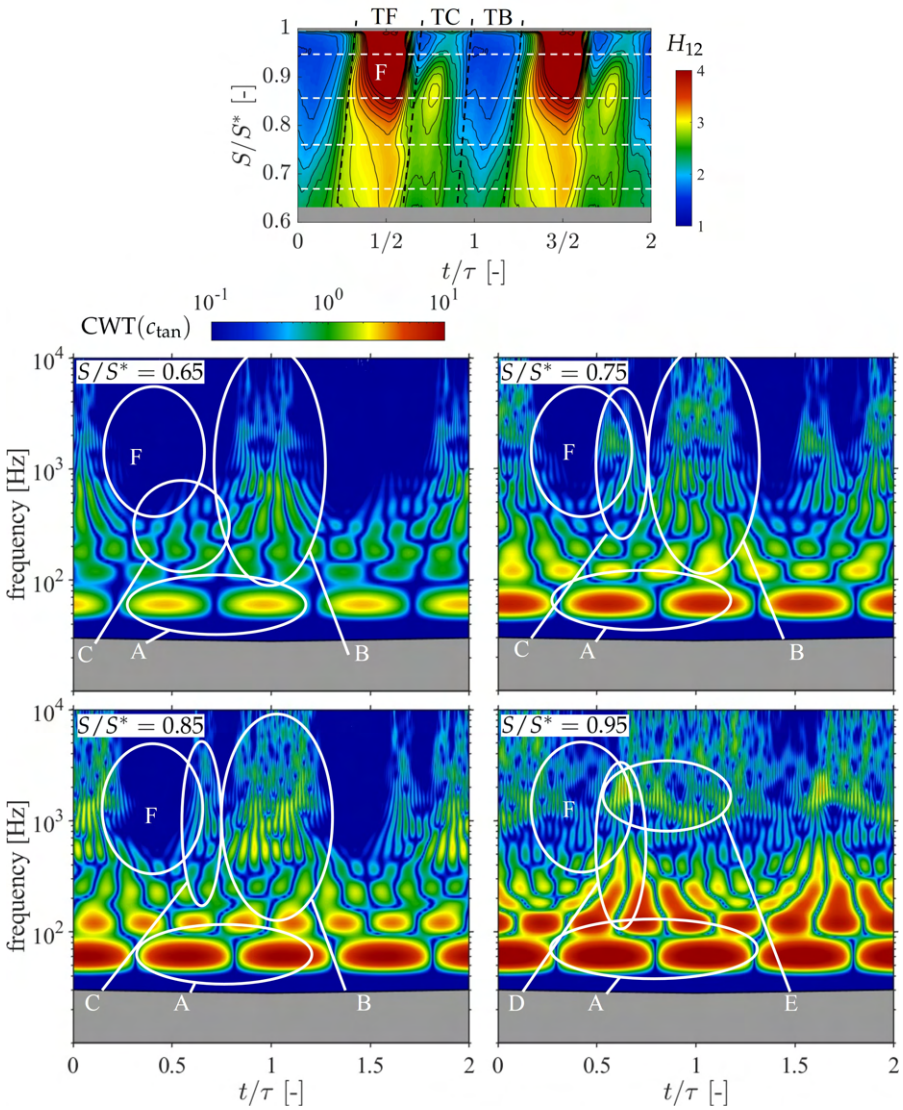

Figure 4.30: Spectra of the continous wavelet transformation of the tangential velocity component at four equally spaced streamwise positions along the line of maximum STD (bottom four figures), and time space visualization of the shape factor H along the blade surface near the trailing edge (top figure).

The temporal extension of the range (TC) is smaller than that of the direct wake impact, as already noted in section 4.4.2, and also the amplitudes of the spectrum excited by this phenomenon are somewhat smaller. Nevertheless, this effect seems to contribute significantly to the formation or amplification of the KH-mode within the detached boundary layer, whose existence could be proven in Fig. 4.21 by means of the Q-criterion.

This is illustrated by the spectral pattern visible in region (D), which extends up to 2000 Hz and is clearly related to the structures in region (E), which originate inside the time window (TC), affected by the accelerated fluid.

It can therefore be concluded that for this operating point the KH instability is enhanced by the sweeping of the accelerated region over the detached shear layer. This also explains the slightly increased frequencies compared to the unperturbed case. According to equation (4.9) this phenomenon can be attributed to the increased velocity at the edge of the shear layer, which is additionally confirmed by the frequency drop after the accelerated flow region has passed by.

4.5.4 Summary

With the help of the frequency domain analysis presented above, a separation of the different mechanisms involved in the transition process could be achieved, which enabled the identification of the individual components and their respective characteristics as well as tracing their development. It is shown that in both unperturbed inflow cases, the KH instability is significantly involved in the transition process and is exponentially amplified to a similar extent within the detached shear layer. While the data in the laminar inflow case indicate the presence of viscous TS instability, in the turbulent inflow case a more pronounced mechanism emerges, indicating the presence of Klebanoff modes, which seem to interact with the KH mechanism.

In the two perturbed cases, based on a conventional frequency analysis, the clearly more complex spectrum in the case of low Strouhal number could be observed. This underlines the substantially more complex transition processes in this case. However, it was shown that this method is not sufficient for capturing transient effects. With the help of CWT, this problem could be circumvented, whereby individual characteristic frequency ranges could be assigned to the individual boundary layer states during a wake transition. This also proved the occurrence of shear layer instabilities such as the KH mode.

4.6 Modal analysis

As the previous chapters have clearly demonstrated, the phenomenon of transition in separated shear layers is highly complex due to the interaction of different fluid mechanical phenomena, so that a separation of the different components poses a great challenge. Nevertheless, a profound understanding of the interplay of these mechanisms is essential when it comes to developing or improving empirical models or designing control mechanisms of those phenomena. In the chapters presented so far, a detailed analysis in both the time and frequency domain was used to identify different mechanisms and to assign them to different frequency ranges in order to track their energetic impact within the macroscopic phenomenology. This procedure is time-consuming and requires a lot of intuition from the user.

The aim of the following chapter is therefore to decompose the complex 3-dimensional flow field in the area of the suction-side trailing edge of the blade into its different mode shapes with the help of the proper orthogonal decomposition (POD) approach, in order to find the elusive coherent structures, which dominate the transition process within the separated shear layer.

For this purpose, the high-dimensional flow field, covering millions of degrees of freedom (DOF), is projected onto a reduced order set of spatial modes, each representing a certain amount of turbulent kinetic energy (TKE). For this the procedure described in section 3.3.5 is applied, enabling a precise analysis of the individual components, which will be presented in the following.

Since in the case of perturbed inflow an analysis by means of POD is overshadowed by the global wake effects and thus does not provide any further results, only the two operating points without wake disturbance will be discussed in the following.

4.6.1 Reference case analysis

In a first step, the reference case OP-CL is analyzed to identify the modes that dominate the transition process in the case of unperturbed inflow. For this purpose, following the modal decomposition of the flow field by means of POD, an analysis of the convergence of its POD eigenvalues is carried out, with the help of which the first n modes can be identified, which represent an arbitrary percentage of the total TKE.

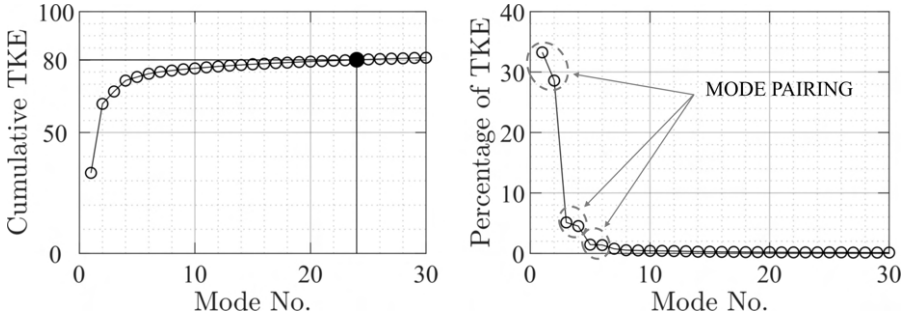

Figure 4.31: OP-CL: TKE of the first 30 POD modes, cumulative representation (left) and percentage representation of total TKE (right)

The convergence of the first 50 POD eigenvalues is depicted in Fig. 4.31 (left) by means of the cumulative sum of their respective TKE. In this case 80% of the overall TKE is covered by only 24 of the total 1875 modes, which represents a very satisfactory convergence. It can therefore be assumed that the first energetic modal structures are linked to coherent flow features which have a significant influence on the transition process.

Looking at the energy content of the individual modes (Fig. 4.31 (right)), it is also noticeable that the first 6 modes occur as pairs of similar energy levels. This phenomenon, called mode pairing, is typical for vortex shedding mechanisms and will be discussed in more detail later on.

However, before a detailed analysis of the different modal contributions is carried out, the quality of the reconstruction of the flow field on the basis of different sets of modes will be evaluated. For this purpose, the flow field at an arbitrary time step is reconstructed by setting up a reduced order model (ROM) based on Eq. (3.29), where different numbers of modes were picked as a basis and compared to the original flow solution. The number of modes was chosen in such a way that they represent TKE levels of 80%, 85%, 90%, 95% and 100%.

Figure 4.32 shows a contour distribution of the normalized velocity magnitude c/c_{in} on the boundary cell faces of the rearmost portion of the considered 3-dimensional evaluation volume (cf. section 3.2.5).

An inspection of the original snapshot reveals distinct structures in region (A), indicating the spanwise oriented coherent KH-rolls. In area (B), small-scale structures are visible, which form as a consequence of the advancing turbulent breakdown of the flow within the detached shear layer.

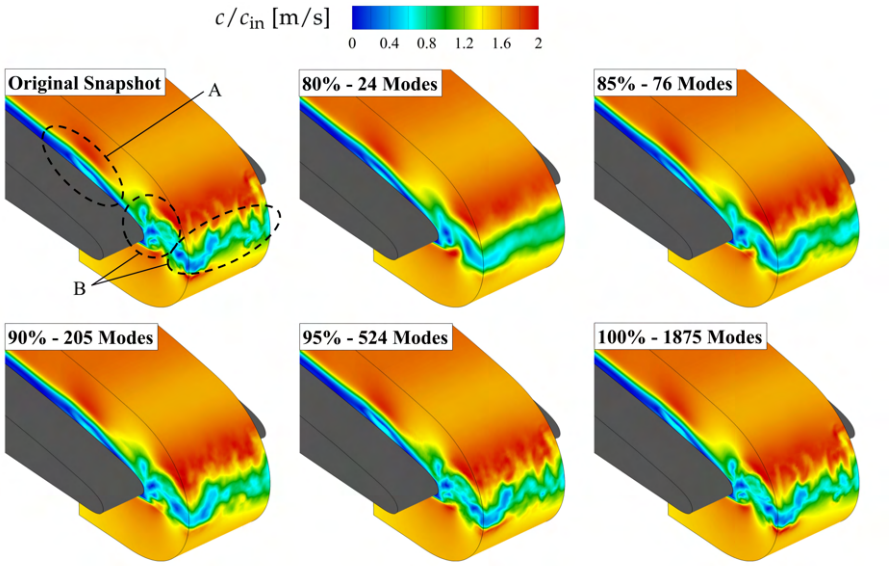

Figure 4.32: OP-CL: Flow field reconstruction based on different numbers of modes compared to the original flow field (top left) for an arbitrary snapshot.

While all ROMs seem to reproduce the coherent structures similarly well, the less deterministic patterns in the areas (B), however, differ more clearly, which is to be expected due to the decreasing coherence of the flow structures associated with the higher modes. The low order ROM based reconstructions can thus be seen as an ensemble averaged variant of the snapshot data based on the shedding cycle of the coherent flow motion.

If a reduced order model (ROM), for example based on a Galerkin projection, is to be generated on the basis of this reduced spatial projection, it is important to decide at this point which flow structures must finally be represented by this model. Since this is not the focus of this work, it only remains to be noted that the model based on the first 24 modes, which covers 80% of the TKE, obviously already contains all the dominant energy carrying flow structures, as visualized in Fig. 4.33, based on the Q-criterion.

All coherent flow features like the shear layer separation (A), the spanwise KH-rolls (B) as well as some features which form as the flow progresses towards the turbulent breakdown (C) are captured by the ROM. Consequently it can be assumed that an analysis of the first 24 modes would be sufficient for

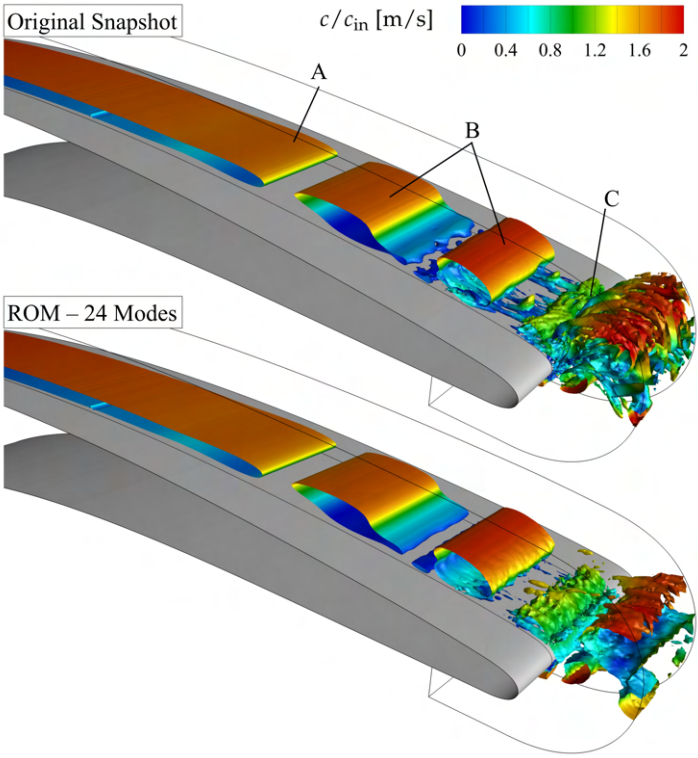

Figure 4.33: OP-CL: Flow field reconstruction (bottom) based on 24 modes (representing 80% of total TKE) compared to the original flow field (top) for an arbitrary snapshot (iso-surface of Q-criterion at $Q = 1 \times 10^6\,\mathrm{s}^{-2}$).

an identification and visualization of the essential mechanisms of the transition process, which is the main focus of the following.

In Fig. 4.34 (left) the distribution of the first three POD modes is visualized via contour representations of the normalized velocity magnitude along a slice at mid-span position of the blade. The right column shows the spectra of the respective time coefficients.

Both the spatial structure of the modes and the frequency peaks of their temporal coefficients clearly prove that these modes are the ones originating from the KH instability mechanism (cf. Fig. 4.25). The first mode represents the fundamental mode, while the 3$^{\mathrm{rd}}$ and 5$^{\mathrm{th}}$ mode represent the higher har-

monic content of lower energy. They correspond to the deviation of fluid motion from purely periodic convection of coherent structures extracted by the first mode.

It should be noted at this point that visual inspection of the mode shapes has shown that besides the similar energy level (cf. Fig. 4.31 (right)) modes 2, 4, and 6 have similar spatial structures at almost the same frequencies as their odd neighbors, but are characterized by a spatial shift of about 1/4 of the spatial KH wavelength λ (identified between two maxima of the course of the respective temporal coefficients as shown in Fig. 4.34 (bottom row)). This indicates that the first 3 POD mode pairs exhibit spatial correlation, which is typical of a vortex shedding phenomenon (e.g. [9, 60, 143]) and underlines the convective character of the underlying mechanism.

According to Fig. 4.31 the first mode covers over 30% of the overall TKE inside the 3-dimensional evaluation region, while the sum of all six first modes is almost 75%. This fact additionally underlines the dominance of the KH-instability mechanism within the transition process at the investigated operating conditions.

An analysis of the remaining modes and associated spectra of the temporal coefficients revealed that, with the exception of mode 15, no other modes could be identified that were associated with coherent structures. Rather, most of the structures are interactions of fluid motions of different frequency ranges, which can be assigned to the turbulent breakdown, as can be seen from the increasing accuracy of the reproduction of this range in Fig. 4.32 with the increase of higher modes.

In contrast, mode 15, whose structure and spectrum is shown in Fig. 4.35, can be assigned a clearly demarcated low-frequency band between 600 Hz and 900 Hz. The structure of the mode also indicates a coherent fluid motion originating upstream of the LSB inside the attached laminar boundary layer, which interacts with the KH mode within the rear portion of the LSB, and thus contributing to the final turbulent break down. The fact that this mode extends far upstream of the LSB along the attached boundary layer suggests that it is a consequence of a viscous instability, namely the TS instability.

The question now arises whether this mode was also previously recognizable in the frequency analyses of the reference case, which were shown in Fig. 4.25. This is indeed the case in region B, which was previously identified as subharmonic content of the KH-mode.

The reason that the previously identified peaks in the low-frequency range between 300 and 400 Hz (cf. Fig. 4.25) are not detected by the POD is that these modes obviously do not interact directly with the high-energy KH

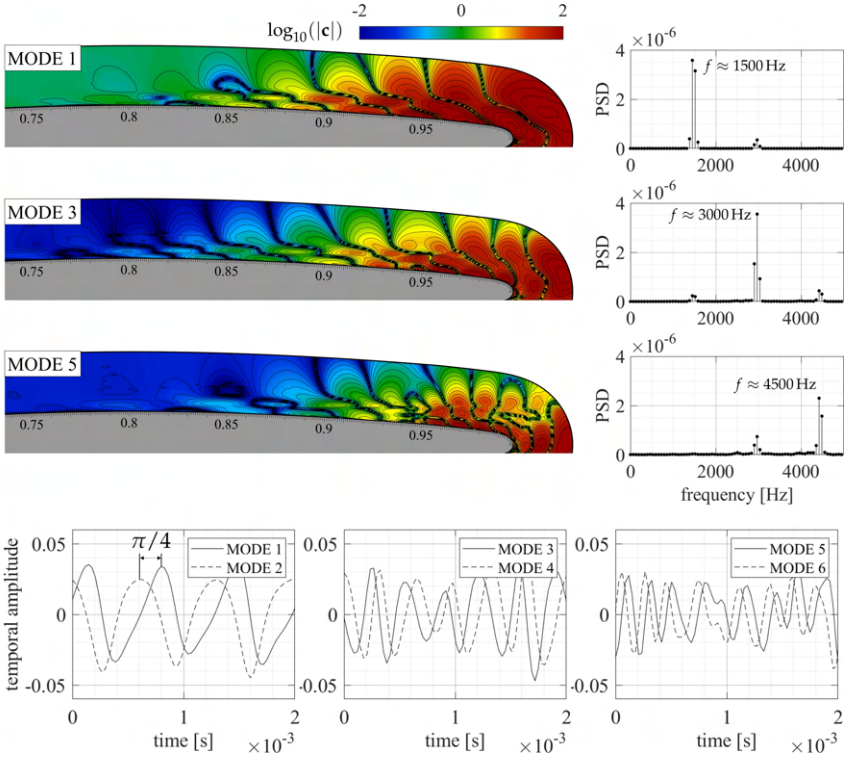

Figure 4.34: OP-CL: Distribution of POD modes 1, 3, 5 at midspan position together with the spectra of the respective time coefficients (top three rows), and temporal progression of the temporal coefficients belonging to the first three mode pairs (bottom row).

mode, but this communication takes place only via the harmonic content. Since the POD performs an energetic ranking of the modes, it can occur that low-energy modes cannot be identified by the POD, although they may contribute significantly to the flow dynamics, as *Sayadi et al.* [109] describe.

Nevertheless, the relevant flow structures that govern the transition process have been successfully identified for the reference case OP-CL and it remains to be verified how they are influenced by the incoming free stream turbulence.

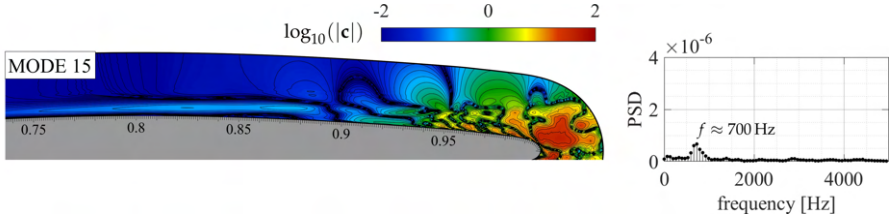

Figure 4.35: OP-CL: Distribution of POD mode 15 at midspan position together with the spectrum of the respective time coefficient

4.6.2 Influence of free-stream turbulence

As could already be observed in Fig. 4.25 (right), the overall energy level for the case with free-stream turbulence is significantly higher, as for the reference case OP-CL. Especially in the low-frequency range up to 1000 Hz, the spectra are much "fuller" due to the energy transfer of the turbulent structures from the free flow into the boundary layer. This is also reflected in the POD spectrum, which is shown in Fig. 4.36 (top row, left).

In contrast to the reference case, the convergence behavior is significantly flatter. In this case, 291 of the total 1875 modes are necessary to represent 80% of the total TKE. A reconstruction of the flow pattern on the basis of a ROM derived from these 291 modes is shown in Fig. 4.37. Despite the significantly more complex flow field, an adequate representation of the coherent flow structures, such as the laminar separation (A), as well as the spanwise KH-rolls, which in this case exhibit a pronounced 3-dimensional distortion, can be achieved, with some deviations in the non coherent turbulent region (C).

The respective percentage of total TKE is shown in Fig. 4.36 (top row, right) for the first 300 modes. Again, the first four modes appear as mode pairs, which indicates a convective character of a process dominated by shedding mechanisms, similar to the reference case considered before. This means that also in this case the KH instability plays a key role in the transition process. However, it remains to be clarified at this point whether the frequency shifts observed in section 4.5 can be attributed to an additional transition mechanism and whether this can be clearly identified by means of the POD.

To achieve this, the structure of modes 1 and 3 is shown in Fig. 4.36. The frequency spectra of the temporal coefficients are also shown here to enable the assignment of the respective modes to the frequency ranges identified in section 4.5. As in the reference case, the respective odd neighboring modes

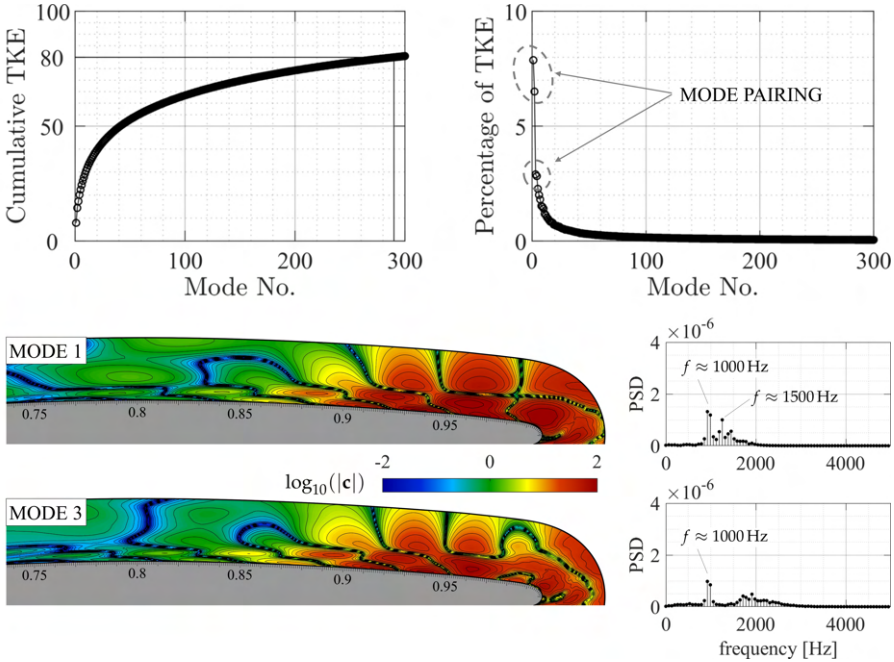

Figure 4.36: OP-CT: TKE of the first 300 POD modes, cumulative representation (top left) and percentage representation of total TKE (top right), and distribution of POD mode 1 and 3 at midspan position together with the spectra of their respective time coefficients (bottom rows).

have a similar structure, but are spatially shifted by $\pi/4$, and are therefore not shown for the sake of clarity.

While the first mode belonging to the dominant mode pair shows both frequency ranges previously identified in Fig. 4.25 at approx. 1000 Hz and 1500 Hz, mode 3 is clearly biased towards the 1000 Hz range. However, a comparison of the structures of the two modes reveals only minor differences, which only become apparent on closer inspection. Both modes are dominated by the typical convective KH pattern, which is also consistent with their appearance as mode pairs.

This leads to the conclusion that, due to the similar energy contribution of the involved mechanisms, no unambiguous separation is possible, but that the modes identified by the POD are mixed forms of the contributing modes,

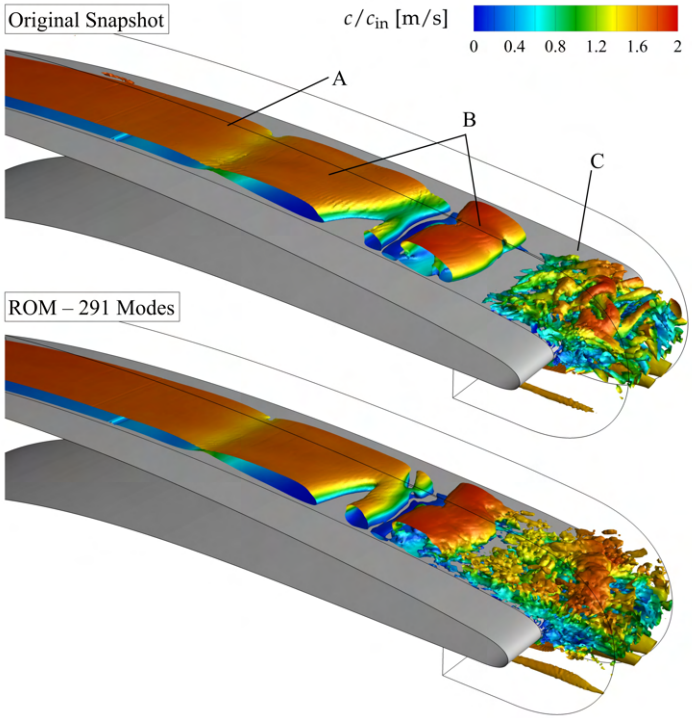

Figure 4.37: OP-CT: Flow field reconstruction (bottom) based on 291 modes (representing 80% of total TKE) compared to the original flow field (top) for an arbitrary snapshot (iso-surface of Q-criterion at $Q = 1 \times 10^6\,\mathrm{s}^{-2}$).

which leads to the distortion of the KH-rolls as observed in the previous chapters.

This 3-dimensional deformation is caused by elongated structures running in the direction of the flow (Klebanoff structures), which carry fluid of different streamwise velocity, causing a distortion of the cross-flow profile.

The streaks originate near the leading edge of the blade, as this is a receptivity site where the mean flow changes rapidly [77]. According to [49], the mechanism through which these streaks are produced in a laminar boundary layer is referred to as "shear sheltering", where the time-mean shear in a laminar boundary layer acts to filter perturbations from the free-stream turbulence. Thus only certain frequency components can penetrate and are then

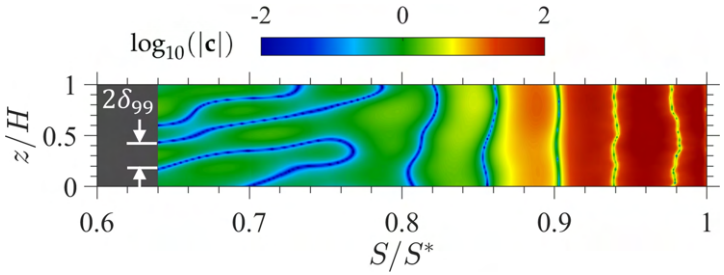

Figure 4.38: OP-CT: Mode 1 visualized at a slice along the line of maximum STD

amplified by the mean shear, causing the frequency spectra to shift towards lower frequencies, as could be observed in Fig. 4.25.

These structures are illustrated on a slice along the line of maximum STD (cf. Fig. 4.24), which is shown in Fig. 4.38 using the example of POD mode 1.

The streamwise elongated structures are clearly visible upstream of the LSB. Their spanwise extent is about $2\delta_{99}$, which is within the range of $2\delta_{99} - 4\delta_{99}$ given by *Balzer and Fasel* [7] and underlines the validity of the present investigations.

Nevertheless, the Klebanoff streaks do not appear to be strong enough to extend far into the transition region, as it is the case in the studies of *McAuliffe and Yaras* [77] and *Balzer and Fasel* [7] in the case of high FSTI levels. It can therefore be concluded that the present case is not a bypass transition triggered by the streamwise oriented streaks, but a KH-mode dominated transition accelerated due to the 3-dimensional distortion caused by the streamwise streaks.

4.6.3 Summary

With the help of the presented modal analysis based on the POD method, an energetic evaluation of the involved transition mechanisms could be performed. It was shown that in the case of laminar inflow the KH mechanism is responsible for almost 75% of the total TKE and thus represents the dominant transition mechanism. A reconstruction of the flow field on the basis of only 24 modes thus already covers 80% of the total TKE of the flow and represents the essential flow structures, which could be used e.g. with the aid of a ROM for the efficient training of artificial intelligences. In addition to the dominant KH mode, a low-frequency mode was also identified,

which arises upstream of the LSB and is significantly involved in the turbulent breakdown of the shear layer, especially in the rear region of the LSB. It could be shown that this is most likely a subharmonic interaction between the viscous TS instability and the KH instability.

In the case of turbulent inflow, the convergence of the POD was much flatter, which is why 291 modes are necessary to represent 80% of the TKE. Nevertheless, the dominance of the KH mechanism was shown, whose occurrence in the highest energy modes is accompanied by elongated Klebanoff modes aligned in the flow direction, which interact with the KH structures and thus cause for a distortion and an ultimately accelerated turbulent decay.

5 Summary & outlook

The present work deals with the numerical investigation of the wake boundary layer interaction in axial LPT stator blades using highly resolved LES, which was carried out within the framework of the DFG joint project PAK948: "*Near-wall flow in turbomachinery blading*", within subproject 4: "*Influence of periodic wakes on the near-wall unsteady flow in axial turbine annular cascades*".

The underlying test case is a low-speed, large-scale annular test rig located at the Chair of Turbomachines and Aero-Engines, which was specifically retrofitted for such types of investigations and provides excellent accessibility for measurement probes and sensors due to its large dimensions.

Within the present work, a numerical model was developed which, on the basis of detailed boundary conditions derived from the experimental data, is able to reproduce the transition process typical for LPT blades in the aft portion of the suction side blade surface. In order to guarantee this, the numerical predictions were carefully verified with the help of the experimental data, which consistently revealed excellent agreement. The high spatial resolution of the verified results could then be used to obtain deeper insights into the transition process in the presence and absence of periodic incoming wakes. On the one hand this underlined the experimental findings and on the other hand gave much deeper insight into the involved mechanisms. This was made possible, in part, by an efficient implementation of a reduced transient data output in the relevant regions, which enabled a targeted applicability of modern analysis methods in the time, frequency and modal domain.

Essential findings

- At the investigated Reynolds number of $\mathrm{Re} = 200,000$, in the absence of wake influences, the transition process is characterized by a transition within a detached shear layer of a closed separation bubble, which could be classified as belonging to the "short bubble" regime according to the characterization after *Hatman and Wang* [38].
- It was shown that the correlations according to *Hatman and Wang* [38], which are mainly based on experiments on flat plates, can be largely transferred to the present realistic application case of LPT flow.
- The transition process in this case is dominated by the Kelvin-Helmholtz (KH) instability mechanism, which arises in the region of the inflection point of the boundary layer profiles and is exponentially amplified within the detached shear layer.

- In the rear area of the separation bubble near the wall, additional viscous processes take place, which are significantly involved in the turbulent breakdown of the shear layer. This finding is in accordance to the recent investigations of *McAuliffe and Yaras* [74, 77].

- In the case of laminar inflow an interaction between TS-waves and KH instability modes could be identified, which largely influences the turbulent breakdown of the shear layer, which supports the findings of *Lang et al.* [55], *McAuliffe and Yaras* [74, 75], *Roberts and Yaras* [104].

- In the case of additional free stream turbulence, an accelerated transition was observed in comparison to the laminar inflow, resulting in a spanwise distortion of the KH structures leading to an early turbulent breakdown of the same. This was found to be caused by streamwise oriented elongated structures of accelerated and decelerated fluid, called Klebanoff streaks, which replace the viscous instability mechanism of Tollmien-Schlichting (TS) waves found in the attached boundary layer of the laminar inflow case.

- The instability Strouhal number evaluated in the separation point $\mathrm{Sr}_{\theta s} = 0.007$ was found to be well within the range known from the literature $0.005 < \mathrm{Sr}_{\theta s} < 0.016$.

- In the two perturbed operating points, a complete suppression of the flow separation was observed in the case of high Strouhal number, whereas in the case of reduced Strouhal number an intermittent boundary layer separation was observed, which exhibits similar transition mechanisms as in the non-wake influenced cases. This finding is in line with the fundamental theory of *Halstead et al.* [34, 35, 36, 37]

- In case of the much more complex transient boundary layer development at low Strouhal numbers two different wake kinematic phenomena could be identified, which were termed "wake flapping" and "wake convection". with the help of a detailed analysis of the underlying wake kinematics. Based on these findings, essential interaction phenomena between transitional boundary layer and incoming wakes could be explained, which were also found in the experimental data, whereby an extension of *Halstead's* fundamental theory could be achieved.

- Using a 3-dimensional POD decomposition, fundamental coherent structures were identified that determine the transition process. Thus, the basis for the construction of a reduced order model (ROM) has been laid, which can be used in the future, e.g. for the training of evolutionary algorithms and for the improvement of conventional methods ((U)RANS models).

Outlook

In further simulations, a fully 3-dimensional representation of the investigated configuration should be carried out in order to analyze the secondary flow effects and their transient interaction with the blade boundary layer. In this context, it would be interesting to see how the secondary flow system interacts with the transition phenomena in the mid-span region of the blade and how the application of the (steady-state) source term used in the underlying work (see section 3.2.3) affects the solution quality in this type of reduced (quasi 2D) configurations.

A further comparison of these results with the URANS results presented in *Winhart et al.* [148, 149], could provide additional insight into the capabilities of the conventional URANS approach in predicting these complex transient phenomena. With the currently available computing capacity, such large eddy simulations would be feasible within a time horizon of about one month, but due to the large number of grid nodes ($N > 100 \times 10^6$), the implementation of in situ post-processing routines should be considered for the evaluation of the data.

Another application of the numerical models created in this work is the training of artificial intelligences, which are becoming increasingly important in the field of turbulence research. To advance research in this area, a national collaboration has already been initiated with the stochastics group of the University of Wuppertal for the derivation of synthetic turbulence based on reduced-order models that are generated using the POD-based approach presented in this work.

6 Bibliography

[1] P. Addison. *"The Illustrated Wavelet Transform Handbook: Introductory Theory and Applications in Science, Engineering, Medicine and Finance"*. Taylor & Francis, 2002. ISBN 9781420033397. URL `https://books.google.de/books?id=RUSjIMQACQQC`. (page(s) 79)

[2] M. Alam and N. D. Sandham. "Simulation of Laminar Separation Bubble Instabilities". *Direct and Large-Eddy Simulation II*, pages 125–136, 1997. doi: 10.1007/978-94-011-5624-0_12. (page(s) 4, 5)

[3] M. Alam and N. D. Sandham. "Numerical study of separation bubbles with turbulent reattachment followed by a boundary layer relaxation". *Parallel Computational Fluid Dynamics. Recent Developments and Advances Using Parallel Computers*, pages 571–578, 1998. doi: 10.1016/B978-044482849-1/50068-3. (page(s) 4, 5)

[4] M. Alam and N. D. Sandham. "Direct numerical simulation of 'short' laminar separation bubbles with turbulent reattachment". *Journal of Fluid Mechanics*, 410:1–28, 2000. (page(s) 3, 4, 5)

[5] *"ANSYS Fluent Theory Guide"*. ANSYS, Inc., 275 Technology Drive Canonsburg, PA 15317, R2020 edition, 2020. (page(s) 45, 84)

[6] S. Armfield and R. Street. "The Fractional-Step Method for the Navier–Stokes Equations on Staggered Grids: The Accuracy of Three Variations". *Journal of Computational Physics*, 153(2):660 – 665, 1999. doi: 10.1006/jcph.1999.6275. (page(s) 48)

[7] W. Balzer and H. F. Fasel. "Numerical investigation of the role of free-stream turbulence in boundary-layer separation". *Journal of Fluid Mechanics*, 801:289–321, 2016. doi: 10.1017/jfm.2016.424. (page(s) 5, 26, 27, 96, 101, 128, 143)

[8] J. Bell, P. Colella, and H. Glaz. "A second-order projection method for the incompressible navier-stokes equations". *Journal of Computational Physics*, 85(2):257 – 283, 1989. doi: 10.1016/0021-9991(89)90151-4. (page(s) 48)

[9] M. Ben Chiekh, M. Michard, M. Guellouz, and J. Béra. "POD analysis of momentumless trailing edge wake using synthetic jet actuation". *Experimental Thermal and Fluid Science*, 46:89 – 102, 2013. ISSN 0894-1777. doi: 10.1016/j.expthermflusci.2012.11.024. (page(s) 138)

[10] J. S. Bendat and A. G. Piersol. *"Random Data: Analysis and Measurement Procedures"*. John Wiley & Sons, Inc., USA, 3rd edition, 2000. ISBN 0471317330. (page(s) 77)

[11] G. Berkooz, P. Holmes, and J. Lumley. "The Proper Orthogonal Decomposition in the Analysis of Turbulent Flows". *Annual Review of Fluid Mechanics*, 25:539–575, 11 2003. doi: 10.1146/annurev.fl.25.010193.002543. (page(s) 79)

[12] J. Blazek. *"Computational Fluid Dynamics: Principles and Applications"*. Elsevier Science, 2001. ISBN 9780080430096. (page(s) 39, 40, 46)

[13] J. Boussinesq. *"Essai sur la théorie des eaux courantes"*. Mémoires présentés par divers savants à l'Académie des sciences de l'Institut national de France. Imprimerie Nationale, 1877. URL `https://books.google.de/books?id=4NdQAAAAYAAJ`. (page(s) 46)

[14] W. Bräunling. *"Flugzeugtriebwerke: Grundlagen, Aero-Thermodynamik, ideale und reale Kreisprozesse, Thermische Turbomaschinen, Komponenten, Emissionen und Systeme"*. VDI-Buch. Springer Berlin Heidelberg, 2015. ISBN 9783642345388. URL `https://books.google.de/books?id=2uTPoAEACAAJ`. (page(s) 14)

[15] D. R. Chapman. "Computational Aerodynamics Development and Outlook". *AIAA Journal*, 17(12):1293–1313, 1979. doi: 10.2514/3.61311. (page(s) 60)

[16] H. Choi and P. Moin. Grid-point requirements for large eddy simulation: Chapman's estimates revisited. *Physics of Fluids*, 24(1):011702, 2012. doi: 10.1063/1.3676783. (page(s) 39)

[17] S. Choi, H. Yun Nam, and M. Cho. "A comparison of higher-order bounded convection schemes". *Computer Methods in Applied Mechanics and Engineering*, 121(1):281 – 301, 1995. doi: 10.1016/0045-7825(94)00713-W. (page(s) 45)

[18] L. Cordier. "Proper Orthogonal Decomposition: An Overview". *Lecture series 2002-04 and 2003-04 on Post-Processing of Experimental and Numerical Data*, 01 2008. (page(s) 79)

[19] J. Cui, V. Rao, and P. Tucker. "Numerical Investigation of Contrasting Flow Physics in Different Zones of a High-Lift Low Pressure Turbine Blade". *Journal of Turbomachinery*, 138, 09 2015. doi: 10.1115/1.4031561. (page(s) 5)

[20] E. M. Curtis, H. P. Hodson, M. R. Banieghbal, J. D. Denton, R. J. Howell, and N. W. Harvey. "Development of Blade Profiles for Low-Pressure

Turbine Applications". *Journal of Turbomachinery*, 119(3):531–538, 07 1997. doi: 10.1115/1.2841154. (page(s) 12, 15)

[21] J. Dähnert, C. Lyko, and D. Peitsch. "Transition mechanisms in laminar separated flow under simulated low pressure turbine aerofoil conditions". *Journal of turbomachinery*, 135(1), 2013. (page(s) 5, 24, 92, 125, 126)

[22] H. Dryden. "Air flow in the boundary layer near a plate". *NACA Technical Report*, 562, January 1937. (page(s) 3)

[23] J. Dukowicz and A. Dvinsky. "Approximate factorization as a high order splitting for the implicit incompressible flow equations". *Journal of Computational Physics*, 102(2):336 – 347, 1992. doi: 10.1016/0021-9991(92)90376-A. (page(s) 48)

[24] M. Emory and G. Iaccarino. "Visualizing turbulence anisotropy in the spatial domain with componentality contours". *Center for Turbulence Research Annual Research Briefs*, pages 123–138, 2014. (page(s) 76, 98, 99, 100)

[25] M. Farge. "Wavelet Transforms and their Applications to Turbulence". *Annual Review of Fluid Mechanics*, 24(1):395–458, 1992. (page(s) 78)

[26] J. Ferziger and M. Perić. *"Computational Methods for Fluid Dynamics"*. Springer, Berlin, 2008. doi: 10.1007/978-3-642-56026-2. (page(s) 38, 39, 40, 45, 47, 48, 49)

[27] E. Garnier, P. Sagaut, and N. Adams. *"Large Eddy Simulation for Compressible Flows (Google eBook)"*. 01 2009. ISBN 9048128188. (page(s) 40, 46)

[28] P. H. Gaskell and A. K. C. Lau. "Curvature-compensated convective transport: SMART, A new boundedness- preserving transport algorithm". *International Journal for Numerical Methods in Fluids*, 8(6):617–641, 1988. doi: 10.1002/fld.1650080602. (page(s) 45)

[29] M. Gaster. "The structure and behaviour of laminar separation bubbles aerodynamics". *Division N.P.L., Reports and Memoranda*, 3595, 1967. (page(s) 3)

[30] M. Giles. "A Numerical Method For The Calculation Of Unsteady Flow In Turbomachinery". GTL Report #205, Gas Turbine Laboratory, Massachusetts Institute of Technology, May 1991. (page(s) 68)

[31] J. R. S. Graveline and S. A. Sjolander. "A Spectral Study of a Moderately Loaded Low-Pressure Turbine Airfoil—Part I: Identifying Frequencies

Affecting Bypass Transition". *Journal of Turbomachinery*, 135(4), 06 2013. ISSN 0889-504X. doi: 10.1115/1.4007624. 041016. (page(s) 4, 124, 126)

[32] C. Haggmark. "Investigations of disturbances developing in a laminar separation bubble flow (Instability waves)". 2002. (page(s) 128)

[33] P. Hall. "Taylor—Gortler vortices in fully developed or boundary-layer flows: linear theory". *Journal of Fluid Mechanics*, 124:475–494, 1982. doi: 10.1017/S0022112082002596. (page(s) 117)

[34] D. E. Halstead, D. C. Wisler, T. H. Okiishi, G. J. Walker, H. P. Hodson, and H.-W. Shin. "Boundary Layer Development in Axial Compressors and Turbines: Part 1 of 4—Composite Picture". *Journal of Turbomachinery*, 119(1):114–127, 01 1997. ISSN 0889-504X. doi: 10.1115/1.2841000. (page(s) 4, 5, 26, 27, 28, 29, 30, 94, 111, 121, 146)

[35] D. E. Halstead, D. C. Wisler, T. H. Okiishi, G. J. Walker, H. P. Hodson, and H.-W. Shin. "Boundary Layer Development in Axial Compressors and Turbines: Part 2 of 4—Compressors". *Journal of Turbomachinery*, 119(3):426–444, 07 1997. ISSN 0889-504X. doi: 10.1115/1.2841000. (page(s) 4, 5, 27, 28, 146)

[36] D. E. Halstead, D. C. Wisler, T. H. Okiishi, G. J. Walker, H. P. Hodson, and H.-W. Shin. "Boundary Layer Development in Axial Compressors and Turbines: Part 3 of 4—LP Turbines". *Journal of Turbomachinery*, 119 (2):225–237, 04 1997. ISSN 0889-504X. doi: 10.1115/1.2841000. (page(s) 4, 5, 27, 28, 29, 121, 146)

[37] D. E. Halstead, D. C. Wisler, T. H. Okiishi, G. J. Walker, H. P. Hodson, and H.-W. Shin. "Boundary Layer Development in Axial Compressors and Turbines: Part 4 of 4—Computations and Analyses". *Journal of Turbomachinery*, 119(1):128–139, 01 1997. ISSN 0889-504X. doi: 10.1115/1.2841000. (page(s) 4, 5, 27, 28, 146)

[38] A. Hatman and T. Wang. "A Prediction Model for Separated-Flow Transition". *Journal of Turbomachinery*, 121(3):594–602, 07 1999. ISSN 0889-504X. doi: 10.1115/1.2841357. (page(s) 5, 90, 91, 107, 116, 127, 145)

[39] C. Hirsch. *"Numerical Computation of Internal and External Flows: The Fundamentals of Computational Fluid Dynamics"*. Butterworth-Heinemann , 01 2007. doi: 10.1016/B978-0-7506-6594-0.X5037-1. (page(s) 39, 41, 42, 47)

[40] C. Hirsch. *"Numerical Computation of Internal and External Flows, Volume 2: Computational Methods for Inviscid and Viscous Flows"*. Elsevier Science, 2019. ISBN 9780080940519. (page(s) 47)

[41] C. Ho and P. Huerre. "Perturbed Free Shear Layers". *Annual Review of Fluid Mechanics*, 16(1):365–422, 1984. doi: 10.1146/annurev.fl.16.010184.002053. (page(s) 126)

[42] H. P. Hodson and R. J. Howell. "Bladerow Interactions, Transition, and High-Lift Aerofoils in Low-Pressure Turbines". *Annual Review of Fluid Mechanics*, 37(1):71–98, 2005. doi: 10.1146/annurev.fluid.37.061903.175511. (page(s) 1, 5, 14, 27, 28, 90, 91)

[43] P. Holmes, J. L. Lumley, and G. Berkooz. *"Turbulence, Coherent Structures, Dynamical Systems and Symmetry"*. Cambridge Monographs on Mechanics. Cambridge University Press, 1996. doi: 10.1017/CBO9780511622700. (page(s) 79)

[44] H. Horton. "Laminar separation in two and three-dimensional incompressible flow". *PhD Thesis, QueenMary College, University of London, UK*, 1968. (page(s) 3)

[45] J. Hourmouziadis. "Aerodynamic design of low pressure turbines". *AGARD lecture series 167*, 1989. (page(s) 16, 90, 127)

[46] R. J. Howell, H. P. Hodson, V. Schulte, R. D. Stieger, H.-P. Schiffer, F. Haselbach, and N. W. Harvey. "Boundary Layer Development in the BR710 and BR715 LP Turbines—The Implementation of High-Lift and Ultra-High-Lift Concepts". *Journal of Turbomachinery*, 124(3):385–392, 07 2002. doi: 10.1115/1.1457455. (page(s) 5, 11, 13)

[47] A. K. M. F. Hussain and W. C. Reynolds. The mechanics of an organized wave in turbulent shear flow. *Journal of Fluid Mechanics*, 41(2): 241–258, 1970. doi: 10.1017/S0022112070000605. (page(s) 38)

[48] M. S. Istvan and S. Yarusevych. "Effects of free-stream turbulence intensity on transition in a laminar separation bubble formed over an airfoil". *Experiments in Fluids*, 59(3):52, 2018. (page(s) 26, 27, 96)

[49] R. G. Jacobs and P. A. Durbin. "Simulations of bypass transition". *Journal of Fluid Mechanics*, 428:185–212, 2001. doi: 10.1017/S0022112000002469. (page(s) 142)

[50] B. Jones. "Stalling". *J R Aero Soc*, 38:747–770, 1967. (page(s) 3)

[51] P. Klebanoff. "Effect of free-stream turbulence on a laminar boundary layer". *Bulletin of the American Physical Society*, 16(11):1323–1334, 1971. (page(s) 23)

[52] P. Klebanoff, K. Tidstrom, and U. S. N. B. of Standards. "Evolution of amplified waves leading to transition in a boundary layer with zero

pressure gradient". *NASA technical note*, 1959. National Aeronautics and Space Administration. (page(s) 23)

[53] A. N. Kolmogorov. "The Local Structure of Turbulence in Incompressible Viscous Fluid for Very Large Reynolds Numbers". *Proceedings: Mathematical and Physical Sciences*, 434(1890):9–13, 1991. ISSN 09628444. doi: 10.2307/51980. (page(s) 34, 39)

[54] V. Kolár. "Vortex identification: New requirements and limitations". *"International Journal of Heat and Fluid Flow"*, 28(4):638 – 652, 2007. ISSN 0142-727X. doi: 10.1016/j.ijheatfluidflow.2007.03.004. Including Special Issue of Conference on Modelling Fluid Flow (CMFF'06), Budapest. (page(s) 75)

[55] M. Lang, Rist, U., and S. Wagner. "Investigations on controlled transition development in a laminar separation bubble by means of LDA and PIV". *Experiments in Fluids*, 36, July 2004. (page(s) 24, 126, 146)

[56] S. Lardeau, M. Leschziner, and T. Zaki. "Large Eddy Simulation of Transitional Separated Flow over a Flat Plate and a Compressor Blade". *Flow Turbulence and Combustion*, 88, 03 2012. doi: 10.1007/s10494-011-9353-0. (page(s) 26, 96)

[57] D. Lee, D. Fahey, P. Forster, P. Newton, R. Wit, L. Lim, B. Owen, and R. Sausen. "Aviation and global climate change in the 21st century". *Atmospheric Environment*, 43(22-23):3520–3537, July 2009. (page(s) 1)

[58] A. H. Lefebvre. *" Gas turbine combustion "*. Hemisphere Pub. Corp Washington, 1983. ISBN 0891164960 0891168966. (page(s) 8)

[59] D. Lengani and D. Simoni. "Recognition of coherent structures in the boundary layer of a low-pressure-turbine blade for different free-stream turbulence intensity levels". *International Journal of Heat and Fluid Flow*, 54:1–13, 08 2015. doi: 10.1016/j.ijheatfluidflow.2015.04.003. (page(s) 5, 26, 96)

[60] D. Lengani, D. Simoni, M. Ubaldi, and P. Zunino. "POD analysis of the unsteady behavior of a laminar separation bubble". *Experimental Thermal and Fluid Science*, 58:70–79, October 2014. (page(s) 5, 26, 96, 138)

[61] D. Lengani, D. Simoni, M. Ubaldi, P. Zunino, and F. Bertini. "Experimental Investigation on the Time–Space Evolution of a Laminar Separation Bubble by Proper Orthogonal Decomposition and Dynamic Mode Decomposition". *Journal of Turbomachinery*, 139(3):031006, March 2016. (page(s) 5)

[62] B. Leonard. "The ULTIMATE conservative difference scheme applied to unsteady one-dimensional advection". *Computer Methods in Applied Mechanics and Engineering*, 88(1):17 – 74, 1991. doi: 0045-7825(91)90232-U. (page(s) 44)

[63] H. J. Li and Z. Yang. "Numerical study of separated boundary layer transition under pressure gradient". The 12th International Conference on Heat Transfer, Fluid Mechanics and Thermodynamics, 07 2016. (page(s) 128)

[64] J. Lin and L. Pauley. "Low-Reynolds-number separation on an airfoil". *AIAA Journal*, 34(8):1570–1577, 1996. doi: 10.2514/3.13273. (page(s) 126)

[65] J. L. Lumley. "The Structure of Inhomogeneous Turbulent Flows". In A. M. Yaglam and V. I. Tatarsky, editors, *Proceedings of the International Colloquium on the Fine ScaleStructure of the Atmosphere and Its Influence on Radio WavePropagation*, 1967. (page(s) 79)

[66] J. L. Lumley and G. R. Newman. "The return to isotropy of homogeneous turbulence". *Journal of Fluid Mechanics*, 82(1):161–178, 1977. doi: 10.1017/S0022112077000585. (page(s) 75, 98, 99, 100)

[67] C. Lyko, J. Dähnert, and D. Peitsch. "Forcing of Separation Bubbles by Main Flow Unsteadiness or Pulsed Vortex Generating Jets—A Comparison". *Journal of Turbomachinery*, 136(5), 10 2013. ISSN 0889-504X. doi: 10.1115/1.4025214. (page(s) 5, 92)

[68] R. W. Maccormack and A. J. Paullay. "Computational efficiency achieved by time splitting of finite difference operators.". 1972. (page(s) 42)

[69] A. Mahallati, B. R. McAuliffe, S. A. Sjolander, and T. J. Praisner. "Aerodynamics of a Low-Pressure Turbine Airfoil at Low Reynolds Numbers—Part I: Steady Flow Measurements". *Journal of Turbomachinery*, 135(1), 11 2012. ISSN 0889-504X. doi: 10.1115/1.4006319. (page(s) 111)

[70] O. Marxen, M. Lang, and U. Rist. "Discrete linear local eigenmodes in a separating laminar boundary layer". *Journal of Fluid Mechanics*, 711, 2012. doi: 10.1017/jfm.2012.263. (page(s) 5, 126)

[71] U. Maucher, U. Rist, and S. Wagner. *"Transitional Structures in a Laminar Separation Bubble"*, pages 307–314. Vieweg+Teubner Verlag, Wiesbaden, 1999. ISBN 978-3-663-10901-3. doi: 10.1007/978-3-663-10901-3_40. (page(s) 25)

[72] U. Maucher, U. Rist, and S. Wagner. "Secondary Disturbance Amplification and Transition in Laminar Separation Bubbles". In *Laminar-Turbulent Transition*, pages 657–662, Berlin, Heidelberg, 2000. Springer Berlin Heidelberg. ISBN 978-3-662-03997-7. (page(s) 25)

[73] B. Mcauliffe and M. Yaras. "Separation-Bubble-Transition Measurements on a Low-Re Airfoil Using Particle Image Velocimetry". *Proceedings of the ASME Turbo Expo*, 3, 01 2005. doi: 10.1115/GT2005-68663. (page(s) 126)

[74] B. R. McAuliffe and M. I. Yaras. "Numerical Study of Instability Mechanisms Leading to Transition in Separation Bubbles". *Journal of Turbomachinery*, 130(2), 02 2008. doi: 10.1115/1.2750680. 021006. (page(s) 5, 24, 25, 146)

[75] B. R. McAuliffe and M. I. Yaras. "Numerical Study of Turbulent-Spot Development in a Separated Shear Layer". *Journal of Turbomachinery*, 130(4), 08 2008. doi: 10.1115/1.2812948. (page(s) 5, 24, 146)

[76] B. R. McAuliffe and M. I. Yaras. "Passive manipulation of separation-bubble transition using surface modifications". *Journal of Fluids Engineering*, 131(2):021201, 2009. doi: 10.1115/1.2978997. (page(s) 5, 24)

[77] B. R. McAuliffe and M. I. Yaras. "Transition mechanisms in separation bubbles under low-and elevated-freestream turbulence". *Journal of Turbomachinery*, 132(1):011004, 2010. doi: 10.1115/1.2812949. (page(s) 5, 24, 26, 27, 88, 89, 93, 99, 101, 116, 125, 126, 127, 128, 142, 143, 146)

[78] P. W. McDonald. "The Computation of Transonic Flow Through Two-Dimensional Gas Turbine Cascades". volume ASME 1971 International Gas Turbine Conference and Products Show of *Turbo Expo: Power for Land, Sea, and Air*, 03 1971. doi: 10.1115/71-GT-89. (page(s) 42)

[79] F. R. Menter. "Two-equation eddy-viscosity turbulence models for engineering applications". *AIAA Journal*, 32(8):1598–1605, 1994. doi: 10.2514/3.12149. (page(s) 39)

[80] V. Michelassi, J. G. Wissink, J. Frohlich, and W. Rodi. "Large-Eddy Simulation of Flow Around Low-Pressure Turbine Blade with Incoming Wakes". *AIAA Journal*, 41(11):2143–2156, 2003. doi: 10.2514/2.6832. (page(s) 5, 57, 61)

[81] V. Michelassi, L.-W. Chen, R. Pichler, and R. D. Sandberg. "Compressible Direct Numerical Simulation of Low-Pressure Turbines—Part II:

Effect of Inflow Disturbances". *Journal of Turbomachinery*, 137(7), 07 2015. ISSN 0889-504X. doi: 10.1115/1.4029126. (page(s) 5, 55, 96)

[82] C. Müller-Schindewolffs, R.-D. Baier, J. Seume, and F. Herbst. "DNS-Based Analysis of RANS Predictions of a Low-Pressure Turbine Cascade". *Journal of Turbomachinery*, 06 2016. doi: 10.1115/GT2016-57582. (page(s) 5, 55)

[83] M. V. Morkovin. "On the Many Faces of Transition". In *"Viscous Drag Reduction"*, pages 1–31, Boston, MA, 1969. Springer US. (page(s) 22)

[84] F. Nicoud and F. Ducros. "Subgrid-Scale Stress Modelling Based on the Square of the Velocity Gradient Tensor". *Flow Turbulence and Combustion*, 62:183–200, 09 1999. doi: 10.1023/A:1009995426001. (page(s) 46)

[85] D. A. Olson, A. W. Katz, A. M. Naguib, M. M. Koochesfahani, D. P. Rizzetta, and M. R. Visbal. "On the challenges in experimental characterization of flow separation over airfoils at low Reynolds number". *Experiments in fluids*, 54(2):1470, 2013. (page(s) 26, 96)

[86] M. Opoka, R. Thomas, and H. Hodson. "Boundary Layer Transition on the High Lift T106A LP Turbine Blade With an Oscillating Downstream Pressure Field". *Journal of Turbomachinery*, 130, 01 2006. doi: 10.1115/GT2006-91038. (page(s) 92)

[87] W. Orr. "The stability or instability of the steady motions of a liquid. Part I: A Perfect Liquid". *Proceedings of the Royal Irish Academy. Section A: Mathematical and Physical Sciences*, 27:9–68, 1907. (page(s) 2)

[88] W. Orr. "The stability or instability of the steady motions of a liquid. Part II: A Viscous Liquid ". *Proceedings of the Royal Irish Academy. Section A: Mathematical and Physical Sciences*, 27:69–138, 1907. (page(s) 2)

[89] R. Pathak. "The wavelet transform". 01 2009. doi: 10.2991/978-94-91216-24-4_2. (page(s) 79)

[90] L. Pauley, P. Moin, and W. Reynolds. "The structure of two-dimensional separation". *Journal of Fluid Mechanics*, 220:397–411, November 1990. (page(s) 3, 4)

[91] L. L. Pauley. "Structure of local pressure-driven three-dimensional transient boundary-layer separation". *AIAA Journal*, 32(5):997–1005, 1994. doi: 10.2514/3.12086. (page(s) 4)

[92] J. Perot. "An Analysis of the Fractional Step Method". *Journal of Computational Physics*, 108(1):51 – 58, 1993. doi: 10.1006/jcph.1993.1162. (page(s) 48)

[93] P. Petitjeans and J. E. Wesfreid. *"Structure and Perturbation in Görtler Vortex Flow"*, pages 245–251. Ordered and Turbulent Patterns in Taylor-Couette Flow. Springer US, Boston, MA, 1992. ISBN 978-1-4615-3438-9. doi: 10.1007/978-1-4615-3438-9_25. (page(s) 117)

[94] U. Piomelli and J. R. Chasnov. *"Large-Eddy Simulations: Theory and Applications"*, pages 269–336. Turbulence and Transition Modelling: Lecture Notes from the ERCOFTAC/IUTAM Summerschool held in Stockholm, 12–20 June, 1995; Springer Netherlands, Dordrecht, 1996. ISBN 978-94-015-8666-5. doi: 10.1007/978-94-015-8666-5_7. (page(s) 60)

[95] S. Pope. *"Turbulent Flows"*. Cambridge University Press, 2000. doi: 10.1017/CBO9780511840531. (page(s) 31, 34, 35, 58, 59)

[96] L. Prandtl. "Der Luftwiderstand von Kugeln (The air resistance of spheres)". *Nachrichten von der Gesellschaft der Wissenschaften zu Göttingen, Mathematisch-Physikalische Klasse*, pages 177–190, 1914. (page(s) 2)

[97] C. M. Rhie and W. L. Chow. "Numerical study of the turbulent flow past an airfoil with trailing edge separation". *AIAA Journal*, 21(11): 1525–1532, 1983. doi: 10.2514/3.8284. (page(s) 49)

[98] L. Richardson. *"Weather prediction by numerical process"*. Cambridge University Press, 1922. (page(s) 33)

[99] M. Ripley and L. Pauley. "The unsteady structure of two-dimensional steady laminar separation". *Physics of Fluids A: Fluid Dynamics*, 5(12): 3099–3106, 1993. doi: 10.1063/1.858719. (page(s) 3, 4, 126)

[100] U. Rist. "Nonlinear Effects of 2-D and 3-D Disturbances on Laminar Separation Bubbles". In *Nonlinear Instability of Nonparallel Flows*, pages 330–339, Berlin, Heidelberg, 1994. Springer Berlin Heidelberg. doi: 10.1007/978-3-642-85084-4_28. (page(s) 4)

[101] U. Rist. "On Instabilities And Transition in Laminar Separation Bubbles". 09 2009. (page(s) 124)

[102] U. Rist and U. Maucher. "Investigations of time-growing instabilities in laminar separation bubbles". *European Journal of Mechanics - B/Fluids*, 21(5):495 – 509, 2002. ISSN 0997-7546. doi: 10.1016/S0997-7546(02)01205-0. (page(s) 25, 26, 88)

[103] P. Roach. "The generation of nearly isotropic turbulence by means of grids". *International Journal of Heat and Fluid Flow*, 8(2):82 – 92, 1987. ISSN 0142-727X. doi: https://doi.org/10.1016/0142-727X(87)90001-4. (page(s) 63)

[104] S. K. Roberts and M. I. Yaras. "Large-Eddy Simulation of Transition in a Separation Bubble". *Journal of Fluids Engineering*, 128(2):232–238, 08 2005. doi: 10.1115/1.2170123. (page(s) 24, 25, 126, 146)

[105] P. Sagaut and C. Meneveau. *"Large Eddy Simulation for Incompressible Flows: An Introduction"*. Scientific Computation. Springer, 2006. ISBN 9783540263449. (page(s) 32, 40, 46, 47)

[106] A. Samson and S. Sarkar. "An experimental investigation of a laminar separation bubble on the leading-edge of a modelled aerofoil for different Reynolds numbers". *Proceedings of the Institution of Mechanical Engineers, Part C: Journal of Mechanical Engineering Science*, 230(13):2208–2224, 2016. (page(s) 3)

[107] R. D. Sandberg, V. Michelassi, R. Pichler, L. Chen, and R. Johnstone. "Compressible Direct Numerical Simulation of Low-Pressure Turbines—Part I: Methodology". *Journal of Turbomachinery*, 137(5), 05 2015. ISSN 0889-504X. doi: 10.1115/1.4028731. (page(s) 5, 55, 96)

[108] F. Satta, D. Simoni, M. Ubaldi, P. Zunino, and F. Bertini. "Experimental investigation of separation and transition processes on a high-lift low-pressure turbine profile under steady and unsteady inflow at low Reynolds number". *Journal of Thermal Science*, 19(1):26–33, Feb 2010. doi: 10.1007/s11630-010-0026-4. (page(s) 24)

[109] T. Sayadi, P. Schmid, J. Nichols, and P. Moin. "Dynamic mode decomposition of controlled H- and K-type transitions". 2014. (page(s) 139)

[110] H. Schlichting. "Über die Entstehung der Turbulenz in einem rotierenden Zylinder". *Nachrichten von der Gesellschaft der Wissenschaften zu Göttingen, Mathematisch-Physikalische Klasse*, pages 160–198, 1932. (page(s) 2, 19)

[111] H. Schlichting. "Zur Enstehung der Turbulenz bei der Plattenströmung". *Nachrichten von der Gesellschaft der Wissenschaften zu Göttingen, Mathematisch-Physikalische Klasse*, pages 181–208, 1933. (page(s) 2)

[112] H. Schlichting. "Amplitudenverteilung und Energiebilanz der kleinen Störungen bei der Plattenströmung". *Nachrichten von der Gesellschaft der Wissenschaften zu Göttingen, Mathematisch-Physikalische Klasse*, I(47), 1935. (page(s) 2)

[113] H. Schlichting. "Turbulenz bei Wärmeschichtung". *Zeitschrift für angewandte Mathematik und Mechanik*, 15(6):313–338, 1935. (page(s) 2)

[114] H. Schlichting, E. Krause, H. Oertel, and K. Gersten. *"Grenzschicht-Theorie"*. Springer, 2006. ISBN 9783540230045. (page(s) 17, 21)

[115] P. Schmid and D. Henningson. *"Stability and Transition in Shear Flows"*. Applied Mathematical Sciences. Springer New York, 2012. ISBN 9781461301851. (page(s) 21)

[116] M. Schobeiri. *"Gas Turbine Design, Components and System Design Integration"*. 01 2018. ISBN 978-3-319-58376-1. doi: 10.1007/978-3-319-58378-5. (page(s) 12)

[117] G. Schubauer and H. Skramstad. "Laminar Boundary-Layer Oscillations and Transition on a Flat Plate". *Journal of Research of the National Bureau of Standards*, 38:251–292, February 1947. (page(s) 2, 28, 29)

[118] A. D. Scillitoe, P. G. Tucker, and P. Adami. "Large Eddy Simulation of Boundary Layer Transition Mechanisms in a Gas-Turbine Compressor Cascade". *Journal of Turbomachinery*, 141(6), 01 2019. ISSN 0889-504X. doi: 10.1115/1.4042023. (page(s) 57)

[119] J. Serna and B. Lázaro. "On the laminar region and the initial stages of transition in transitional separation bubbles". *European Journal of Mechanics - B/Fluids*, 49:171 – 183, 2015. ISSN 0997-7546. doi: 10.1016/j.euromechflu.2014.08.006. (page(s) 24)

[120] M. Shur, P. Spalart, M. Strelets, and A. Travin. "Synthetic Turbulence Generators for RANS-LES Interfaces in Zonal Simulations of Aerodynamic and Aeroacoustic Problems". *Flow Turbulence and Combustion*, 93:63–92, 06 2014. doi: 10.1007/s10494-014-9534-8. (page(s) 64)

[121] D. Simoni, D. Lengani, M. Ubaldi, P. Zunino, and M. Dellacasagrande. "Inspection of the dynamic properties of laminar separation bubbles: free-stream turbulence intensity effects for different Reynolds numbers". *Experiments in Fluids*, 58(6), June 2017. (page(s) 5, 26, 96)

[122] A. J. Simonsen and P. Å. Krogstad. "Turbulent stress invariant analysis: Clarification of existing terminology". *Physics of Fluids*, 17(8):088103, 2005. doi: 10.1063/1.2009008. (page(s) 76)

[123] M. Sinkwitz, D. Engelmann, and R. Mailach. "Experimental Investigation of Periodically Unsteady Wake Impact on the Secondary Flow in a 1.5 Stage Full Annular LPT Cascade With Modified T106 Blading". *Turbo Expo: Power for Land, Sea, and Air*, 06 2017. doi: 10.1115/GT2017-64390. (page(s) 50, 51)

[124] M. Sinkwitz, B. Winhart, D. Engelmann, F. di Mare, and R. Mailach. "On the Periodically Unsteady Interaction of Wakes, Secondary Flow Development and Boundary Layer Flow in an Annular LPT Cascade:

Part 1 — Experimental Investigation". *Journal of Turbomachinery*, 06 2018. doi: 10.1115/GT2018-76802. (page(s) 50)

[125] M. Sinkwitz, B. Winhart, D. Engelmann, F. di Mare, and R. Mailach. "Experimental and Numerical Investigation of Secondary Flow Structures in an Annular Low Pressure Turbine Cascade Under Periodic Wake Impact—Part 1: Experimental Results". *Journal of Turbomachinery*, 141(2), 01 2019. doi: 10.1115/1.4042284. (page(s) 50)

[126] M. Sinkwitz, B. Winhart, D. Engelmann, F. di Mare, and R. Mailach. "On the Periodically Unsteady Interaction of Wakes, Secondary Flow Development, and Boundary Layer Flow in An Annular Low-Pressure Turbine Cascade: An Experimental Investigation". *Journal of Turbomachinery*, 141(9), 05 2019. doi: 10.1115/1.4043577. (page(s) 50)

[127] M. B. Sinkwitz. *"Experimentelle Untersuchung der Entstehung von Sekundärströmung in Turbinen-Ringgittern unter periodisch-instationärer Zuströmung"*. dissertation, Ruhr-Universität Bochum, 2021. URL `https://hss-opus.ub.ruhr-uni-bochum.de/opus4/frontdoor/deliver/ind` (page(s) 6, 63)

[128] L. Sirovich. "Turbulence and the dynamics of coherent structures. I - Coherent structures. II - Symmetries and transformations. III - Dynamics and scaling". *Quarterly of Applied Mathematics - QUART APPL MATH*, 45, 10 1987. doi: 10.1090/qam/910463. (page(s) 80)

[129] A. Sommerfeld. "Ein Beitrag zur hydrodynamische Erklärung der turbulenten Flüssigkeitsbewegungen". *Proceedings of the 4th International Congress of Mathematicians*, III: 116–124, 1908. (page(s) 2)

[130] P. Spalart and M. Strelets. "Mechanisms of transition and heat transfer in a separation bubble". *Journal of Fluid Mechanics*, 403:329–349, 2000. doi: 10.1017/S0022112099007077. (page(s) 24)

[131] P. R. Spalart and M. K. Strelets. "Direct and Reynolds-averaged numerical simulations of a transitional separation bubble". In *11th Symposium on Turbulent Shear Flows*, Grenoble, France, September 1997. (page(s) 4, 5)

[132] J. Spurk and N. Aksel. *"Strömungslehre: Einführung in die Theorie der Strömungen"*. Springer Berlin Heidelberg, 2019. ISBN 9783662587645. URL `https://books.google.de/books?id=bN-GDwAAQBAJ`. (page(s) 32)

[133] R. Stieger. "The Effects of Wakes on Separating Boundary Layers in Low Pressure Turbines". *PhD Thesis, Cambridge University Engineering Department*, 2002. (page(s) 53)

[134] K. Taira, S. L. Brunton, S. T. M. Dawson, C. W. Rowley, T. Colonius, B. J. McKeon, O. T. Schmidt, S. Gordeyev, V. Theofilis, and L. S. Ukeiley. "Modal Analysis of Fluid Flows: An Overview". *AIAA Journal*, 55(12): 4013–4041, 2017. doi: 10.2514/1.J056060. (page(s) 79)

[135] M. Talan and J. Hourmouziadis. "Characteristic Regimes of Transitional Separation Bubbles in Unsteady Flow". *Flow Turbulence and Combustion*, 69:207–227, 12 2002. doi: 10.1023/A:1027355105017. (page(s) 5, 16, 127)

[136] M. Talan and J. Hourmouziadis. "Characteristic Regimes of Transitional Separation Bubbles in Unsteady Flow". *Flow Turbulence and Combustion*, 69:207–227, 12 2002. doi: 10.1023/A:1027355105017. (page(s) 126)

[137] H. Tennekes and J. Lumley. *"A First Course in Turbulence"*. Butterworth, 1989. URL `https://books.google.de/books?id=_pSyuQAACAAJ`. (page(s) 124)

[138] W. Tollmien. "The production of Turbulence". *NACA Technical Memorandum*, 609, 1931. (page(s) 2, 3)

[139] W. Tollmien. "General instability criterion of laminar velocity distributions". *NACA Technical Memorandum*, 792, 1936. (page(s) 2)

[140] P. Voke and Z. Yang. *"Large-eddy simulation of separation and transition for turbomachinery flows"*, volume 529, pages 46–63. 05 2007. doi: 10.1007/BFb0106092. (page(s) 126)

[141] G. J. Walker. "Transitional flow on axial turbomachine blading". *AIAA Journal*, 27(5):595–602, 1989. doi: 10.2514/3.10150. (page(s) 5)

[142] G. J. Walker. "The Role of Laminar-Turbulent Transition in Gas Turbine Engines: A Discussion". *Journal of Turbomachinery*, 115(2):207–216, 04 1993. doi: 10.1115/1.2929223. (page(s) 5, 23)

[143] D. Wee, T. Yi, A. Annaswamy, and A. Ghoniem. "Self-sustained oscillations and vortex shedding in backward-facing step flows: Simulation and linear instability analysis". *Physics of Fluids*, 16(9):3361–3373, 2004. doi: 10.1063/1.1773091. (page(s) 138)

[144] J. Weiss. "A Tutorial on the Proper Orthogonal Decomposition". 06 2019. doi: 10.2514/6.2019-3333. (page(s) 79)

[145] P. Welch. "The use of fast Fourier transform for the estimation of power spectra: a method based on time averaging over short, modified periodograms". *IEEE Transactions on audio and electroacoustics*, 15(2):70–73, 1967. doi: 10.1109/TAU.1967.1161901. (page(s) 77)

[146] D. C. Wilcox. *Turbulence modelling for CFD*. DCW Industries, La Cañada, 1993. (page(s) 33)

[147] P. Wilson and L. Pauley. "Two- and three-dimensional large-eddy simulations of a transitional separation bubble". *Physics of Fluids*, 10(11): 2932–2940, 1998. doi: 10.1063/1.869813. (page(s) 3, 4)

[148] B. Winhart, A. Sinkwitz, D. Engelmann, F. di Mare, and R. Mailach. "On the Periodically Unsteady Interaction of Wakes, Secondary Flow Development and Boundary Layer Flow in an Annular LPT Cascade: Part 2 — Numerical Investigation". In *Proceedings of the ASME Turbo Expo 2018: Turbomachinery Technical Conference and Exposition. Volume 2A: Turbomachinery*, Oslo, Norway, June 11-15 2018. ASME. (page(s) 66, 72, 147)

[149] B. Winhart, M. Sinkwitz, A. Schramm, D. Engelmann, F. di Mare, and R. Mailach. "Experimental and Numerical Investigation of Secondary Flow Structures in an Annular Low Pressure Turbine Cascade Under Periodic Wake Impact—Part 2: Numerical Results". *ASME J. Turbomach.*, 141(2):021009, February 2019. (page(s) 66, 72, 75, 147)

[150] D. Wisler. "The Technical and Economic Relevance of Understanding Boundary Layer Transition in Gas Turbine Engines". *NASA Minnowbrook II proceedings*, 1997. (page(s) 13)

[151] L. Yang. "Investigations of complicated flow mechanism and aerodynamic design method in low pressure turbine at low Reynolds number". *Beijing: Beihang University*. (page(s) 5)

[152] Z. Yang. "Numerical study of instabilities in separated-reattached flows". *International Journal of Computational Methods and Experimental Measurements*, 1(2):116–131, 2013. doi: 10.2495/CMEM-V1-N2-116-131. (page(s) 15, 24, 27)

[153] Z. Yang. "On bypass transition in separation bubbles: a review". *Propulsion and Power Research*, 8(1):23–34, March 2019. (page(s) 21, 27, 126)

[154] A. Young and H. Horton. "Some results of investigation of separation bubbles". *AGARD CP*, 4:779–811, 1966. (page(s) 3)

[155] Z. Zou, S. Wang, H. Liu, and W. Zhang. *"Axial Turbine Aerodynamics for Aero-engines: Flow Analysis and Aerodynamics Design"*. Springer Singapore, 2019. ISBN 9789811354809. URL https://books.google.de/books?id=ZcFWwAEACAAJ. (page(s) 14, 15)

Curriculum Vitae

Personal Information

Benjamin Winhart
born 28 October 1985 in Berlin, Germany

Professional Experience

since 10/2014 — Research assistant and doctoral student,
Chair of Thermal Turbomachines and Aeroengines,
Department of Mechanical Engineering,
Ruhr-Universität Bochum, Germany

03/2012 - 09/2014 — Student research assistant,
Institute of Fluid Mechanics and Technical Acoustics,
Chair of Numerical Fluid Dynamics,
TU Berlin

08/2010 - 09/2011 — Student research assistant,
Institute for Space and Aviation,
Chair of Aerodynamics,
TU Berlin

Academic Education

10/2010 - 06/2014 — Aerospace Engineering
TU Berlin
Master of Science

10/2006 - 09/2010 — Transportation Engineering
TU Berlin
Bachelor of Science

School Education

2003 - 2005 — Secondary school (Abitur),
Arndt-Gymnasium, Berlin Dahlem

1997 - 2003 — Secondary school,
Evangelisches Gymnasium zum Grauen Kloster,
Berlin Grunewald